

**DEVELOPMENT OF ANGLE-INTEGRATED
PHOTOEMISSION SPECTROSCOPY
SYSTEM USING SYNCHROTRON
LIGHT**

Mr. Samred Kantee

**A Thesis Submitted in Partial Fulfillment of the Requirements for
the Degree of Doctor of Philosophy in Physics**

Suranaree University of Technology

Academic Year 2004

ISBN 974-533-430-8

การพัฒนาระบบโฟโตอิมิตชันสเปกโทรสโกปีแบบรวบรวมเชิงมุม
โดยใช้แสงซินโครตรอน

นายสำเร็จ กันธิ

วิทยานิพนธ์นี้เป็นส่วนหนึ่งของการศึกษาตามหลักสูตรปริญญาวิทยาศาสตรดุษฎีบัณฑิต

สาขาวิชาฟิสิกส์

มหาวิทยาลัยเทคโนโลยีสุรนารี

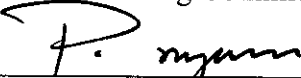
ปีการศึกษา 2547

ISBN 974-533-430-8


DEVELOPMENT OF ANGLE-INTEGRATED PHOTOEMISSION SPECTROSCOPY SYSTEM USING SYNCHROTRON LIGHT

Suranaree University of Technology has approved this thesis submitted in partial fulfillment of the requirements for the Degree of Doctor of Philosophy.

Thesis Examining Committee


(Asst. Prof. Dr. Prapun Manyum)


Chairperson


(Asst. Prof. Dr. Prayoon Songsiriritthigul)

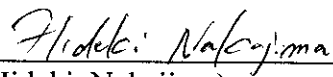
Member (Thesis Advisor)


(Prof. Dr. Takehiko Ishii)

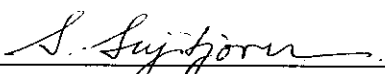
Member



(Assoc. Prof. Dr. Prasart Suebka)

Member


(Dr. Hideki Nakajima)

Member


(Assoc. Prof. Dr. Sarawut Sujitjorn)


(Assoc. Prof. Dr. Prasart Suebka)

สำเร็จ คณธี : การพัฒนาระบบโฟโตมิสชันสเปกโทรสโกปีแบบรวบรวมเชิงมุม
โดยการใช้แสงซินโครตรอน (DEVELOPMENT OF ANGLE-
INTEGRATED PHOTOEMISSION SPECTROSCOPY SYSTEM
USING SYNCHROTRON LIGHT) อาจารย์ที่ปรึกษา : ผู้ช่วยศาสตราจารย์ ดร.
ประยูร ส่งสิริฤทธิกุล, 159 หน้า. ISBN 974-533-430-8

ระบบโฟโตมิสชันสเปกโทรสโกปีแบบรวบรวมเชิงมุมได้ถูกพัฒนาขึ้น ณ ห้องปฏิบัติการ
แสงสยามสำหรับงานวิจัยทางด้านสเปกโทรสโกปีและงานวิเคราะห์เชิงเคมี ระบบดังกล่าวได้ใช้
ประโยชน์แสงซินโครตรอนจากระบบลำเลียงแสงซินโครตรอน BL-4 ซึ่งเป็นระบบลำเลียงแสง
ซินโครตรอนแรกของห้องปฏิบัติการแสงสยาม และแหล่งกำเนิดแสงอื่นๆสำหรับการกระตุ้นเช่น
ตะเกียงแสงอัลตราไวโอเลต ปืนอิเล็กตรอน หลอดรังสีเอกซ์ เทคนิคการวัดต่างๆ สามารถทำได้โดย
ใช้ระบบที่ถูกพัฒนาขึ้น เทคนิคดังกล่าวได้แก่ เทคนิคโฟโตมิสชันโดยใช้แสงซินโครตรอน
เทคนิคสเปกโทรสโกปีของโฟโตอิเล็กตรอนที่ถูกกระตุ้นโดยรังสีเอกซ์ เทคนิคสเปกโทรสโกปี
ของโฟโตอิเล็กตรอนที่ถูกกระตุ้นโดยแสงอัลตราไวโอเลต และเทคนิคสเปกโทรสโกปีของเออร์เจ
อิเล็กตรอน การใช้แสงซินโครตรอนทำให้ลักษณะการวัดโฟโตอิเล็กตรอนเป็นไปได้หลายรูปแบบ
ในวิทยานิพนธ์นี้ ได้มีการอธิบายข้อพิจารณาการออกแบบและรายละเอียดของระบบที่ได้พัฒนาขึ้น
และมีการรายงานผลที่ได้จากการดำเนินการเดินเครื่องและทดสอบระบบดังกล่าว

สาขาวิชาฟิสิกส์
ปีการศึกษา 2547

ลายมือชื่อนักศึกษา ณัฏฐ์ ส่งสิริ
ลายมือชื่ออาจารย์ที่ปรึกษา อ. ประยูร
ลายมือชื่ออาจารย์ที่ปรึกษาร่วม อ. ชัย
ลายมือชื่ออาจารย์ที่ปรึกษาร่วม อ. นุช

SAMRED KANTEE : DEVELOPMENT OF ANGLE-INTEGRATED

PHOTOEMISSION SPECTROSCOPY SYSTEM USING

SYNCHROTRON LIGHT. THESIS ADVISOR : ASST. PROF.

PRAYOON SONGSIRIRITTHIGUL, Ph.D. 159 PP. ISBN 974-533-430-8

PHOTOEMISSION SPECTROSCOPY /BEAMLINE/ SYNCHROTRON LIGHT

An angle-integrated photoemission spectroscopy (AIPES) system has been developed at the Siam Photon Laboratory for spectroscopic research, as well as for chemical analysis. The system employs synchrotron light from the BL-4 beamline, the first synchrotron light beamline at the Siam Photon Laboratory, and other laboratory excitation sources such as an ultraviolet lamp, an electron gun and an X-ray tube. Different measurement techniques are possible with the newly developed system. Those are photoemission techniques using synchrotron light, X-ray photoelectron spectroscopy, ultraviolet photoelectron spectroscopy and Auger electron spectroscopy. With synchrotron light, various modes of photoemission measurements such as EDC, CIS, CFS and total yield can be performed. The design considerations and the details of the system are described. The commissioning and test results are also reported and discussed.

School of Physics

Academic Year 2004

Student's Signature Sam Kantee

Advisor's Signature P. Songs

Co-advisor's Signature P. Subha

Co-advisor's Signature P. Subha

ACKNOWLEDGEMENTS

This thesis work could not have been completed without the generous support and advice of many persons. I would like to express my deep gratitude to the following persons for their contribution:

- Asst. Prof. Dr. Prayoon Songsiriritthigul, my thesis advisor, for his advice, constructive worthy comments, correction and support with his kindness during the course of my study and my thesis work.
- Dr. Hideki Nakajima, the researcher of the Siam Photon Laboratory, National Synchrotron Research Center (NSRC), Thailand, for his helpfulness, comments and training in the experiment of my thesis work.
- Prof. Dr. Takehiko Ishii, for his guidance, help and correction in regard to my thesis.
- Assoc. Prof. Dr. Prasart Suebka, the dean of Institute of Science, Suranaree University of Technology, for his support in various respects.
- Asst. Prof. Dr. Prapun Manyum, the head of School of Physics, Suranaree University of Technology, for his kind support.
- I would like to thank Mr. Supat Klinkhieo, Mr. Wiwat Wongkokua, Mr. Ritthikrai Chai-ngam, NSRC staff especially engineers in the beamline division, and my family for their help and encouragements.
- Sakon Nakhon Rajabhat University and National Synchrotron Research Center for partially financial support.

Samred Kantee

CONTENTS

	Page
ABSTRACT IN THAI.....	I
ABSTRACT IN ENGLISH.....	II
ACKNOWLEDGEMENTS.....	III
CONTENTS.....	IV
LIST OF TABLES.....	VII
LIST OF FIGURES.....	IX
CHAPTER	
I INTRODUCTION.....	1
1.1 Introductory Remark.....	1
1.2 Synchrotron Light.....	3
1.3 Sources of Synchrotron Light.....	5
1.3.1 Electron Beam	8
1.3.2 Bending Magnet	11
1.3.3 Insertion Devices	13
1.4 Synchrotron Light Beamlines.....	17
1.4.1 Definition of Synchrotron Light Beamline.....	17
1.4.2 Synchrotron Light Optics	19
1.4.2.1 The Optical Path	19
1.4.2.2 Mirrors	26

CONTENTS (Continued)

	Page
1.4.2.3 Gratings	31
1.4.2.4 Monochromators	36
II INSTRUMENTATION AND TECHNIQUES.....	38
2.1 Siam Photon Source.....	39
2.1.1 Injection System	40
2.1.2 Storage Ring	40
2.2 BL-4 Beamline	48
2.2.1 Front-end	48
2.2.2 Optical Beamline	51
2.2.2.1 Monochromator	53
2.2.2.2 Pre- and Post Focusing Mirrors	60
2.2.2.3 Photon Energy Scanning Mechanism.....	64
2.2.3 End Station	67
2.2.4 Vacuum System.....	70
2.2.5 Interlock System.....	73
2.3 Ray Tracing	74
2.4 Photoemission Technique.....	76
2.4.1 Energy Analyzer.....	78
2.4.2 The CLAM2 Spectrometer	82

CONTENTS (Continued)

	Page
III DEVELOPMENT OF CONTROL AND DATA ACQUISITION	
SYSTEM	85
3.1 Design Considerations	85
3.2 System Design	87
3.2.1 Hardware	87
3.2.2 Software	92
3.3 Energy Calibration of the CLAM2 Spectrometer	95
IV RESULTS AND DISCUSSIONS	101
4.1 Source	101
4.2 Imaging and Focusing Properties	105
4.3 Energy Calibration of the Monochromator	125
4.4 Resolution of the monochromator	128
4.5 Higher Order light	147
V CONCLUSION	152
REFERENCES	155
CURRICULUM VITAE	159

LIST OF TABLES

Table	Page
1.1 The coefficients of a_{ij} for toroid, paraboloid and ellipsoid surfaces.	25
2.1 The specifications of the booster synchrotron of the Siam Photon Source	42
2.2 The specifications of the DBA lattice of the storage ring of the Siam Photon Source.....	43
2.3 The specifications of the storage ring of the Siam Photon Source.	44
2.4 The optimum values of E_1 , E_2 , E_3 and E_4 used for determining the line-spacing variation coefficients, r_2 of varied line-spacing plane gratings (VLSPG's).	56
2.5 The specifications of the VLSPG of the BL-4 beamline.	57
2.6 The parameters of the pre-focusing, focusing and post-focusing mirrors.....	61
3.1 The status of TTL signals for different settings of the energy range of the spectrometer.	90
3.2 The status of TTL signals for different pass energies of the analyzer in the EDC mode of measurement. UPS represents the 81.9 eV and 163.84 eV energy ranges, while XPS represents the 1638.4 eV and 3276.8 eV energy ranges.	90

LIST OF TABLES (Continued)

Table	Page
3.3	The status of TTL signals for different settings of the CRR values.91
3.4	The binding energies are used as the reference in the energy calibration of the CLAM2 spectrometer.....96
3.5	The energy calibration curve for the CLAM2 spectrometer obtained and used in this work. V_{dc} and E_k are the control voltage for the spectrometer and the electron kinetic energy, respectively.96
4.1	The input parameters for the source of synchrotron light in the BM4 bending magnet.103
4.2	<i>FWHM</i> of the distribution around the Fermi level obtained from Au spectra shown in Figure 4.19.129
4.3	<i>FWHM</i> of the distribution of photoelectron yield of gold near the Fermi level (the spectra are shown in Figure 4.26)142
4.4	The widths of the entrance and exit slits for the resolving power limited by the slit of 500.143

LIST OF FIGURES

Figure	Page
1.1	Coordinate system for the electron motion in a storage ring.....6
1.2	Phase space illustration of the electron beam shape.....7
1.3	Emission of synchrotron light from bending magnets: (a) top view and (b) side view.12
1.4	The spectrum of synchrotron light produced from 1.0 GeV and 1.2 GeV electrons in a bending magnet with a radius of 2.78 m.....15
1.5	Typical spectra of synchrotron light produced by (a) a wiggler and (b) an undulator.16
1.6	The major components of a beamline.....17
1.7	Light rays from the source A incident on a surface $P(\xi, \omega, l)$ and form an image at B20
1.8	The definition of the parameters for different surfaces.24
1.9	Reflectivity of gold and nickel as a function of photon energy for the angles of incidence of 86.5° , 86° , 85° and 70° for (a) s-polarized light and (b) p-polarized light.27
1.10	The Kirkpatrick-Baez mirror system (Kirkpatrick and Baez, 1948).29
1.11	A diffraction grating showing the diffraction orders.....32
2.1	The schematic diagram of the Siam Photon Source.39
2.2	The DBA lattice of the storage ring of the Siam Photon Source.....41

LIST OF FIGURES (Continued)

Figure	Page
2.3 The vertical and horizontal betatron functions and the horizontal dispersion function of the DBA lattice of the storage ring of the Siam Photon Source.	45
2.4 The calculated spectra of synchrotron light from the bending magnet, undulator and wiggler for the Siam Photon Source.	47
2.5 Top view (a) and side view (b) drawings of the front-end of the BL-4 beamline. The acceptance angle of synchrotron radiation of the beamline is defined by Mask II. The scale in the direction along SR is different from the scale in the direction perpendicular to synchrotron light. MV and PV stand for a manual valve and a pneumatic valve, respectively.....	49
2.6 The photo of the front-end of the BL-4 beamline connected to the beam channel of the vacuum chamber of the BM4 bending magnet.	50
2.7 Optical layout and some parameters of the BL-4 beamline at the Siam Photon Laboratory.....	52
2.8 A convergent light beam incidents on VLSPG. It should be noted that the differences of angles of incidence and the angles of diffraction at point 1 and 2 are exacterated.	55
2.9 The calculated spherical, coma, defocus and slope error aberrations and the resolution limited by the width of the entrance and exit slit of the VLSPG monochromator.....	58

LIST OF FIGURES (Continued)

Figure	Page
2.10	The widths of the entrance and exit slits to obtained a resolution limited by the slit width of 2×10^{-4}59
2.11	Schematic diagram of the focusing optical element in the BL-4 beamline (a) in the vertical plane and (b) in the horizontal plane.63
2.12	Photo of the BL-4 beamline at the Siam Photon Laboratory.64
2.13	The photo of the grating chamber. The step motor for driving the sine bar and the linear encoder are installed outside the grating chamber. The sine bar located inside the UHV chamber is connected to the step motor via the bellow. The linear translator located on the left flange is used for exchanging the gratings.65
2.14	The sine bar for the rotation of the grating in monochromators with a constant included angle.66
2.15	The schematic diagram of the experimental station of the BL-4 beamline shows the major instruments.69
2.16	The schematic diagram of the vacuum systems of the front-end and optical beamline.72
2.17	The schematic diagram of the interlock system for the BL-4 beamline at the Siam Photon Laboratory.73
2.18	The coordinate system used in ray-tracing simulations (Schäfers, 1996).75
2.19	The schematic illustration of the energy diagrams of a photoelectron.77

LIST OF FIGURES (Continued)

Figure	Page
2.20	A feature cross section of a concentric hemispherical energy analyzer.....78
2.21	The schematically diagram of energy level contacting between metallic sample and spectrometer of PES measurement.80
2.22	The schematic diagram of the CLAM2 spectrometer system.82
3.1	The schematic diagram of a new data acquisition using the CLAM2 spectrometer installed at the experimental station of the BL-4 beamline.88
3.2	The wiring diagram between the interface card and the SCU362 unit.....89
3.3	Graphical feature of the control and data acquisition software of the BL-4 beamline.93
3.4	The calibration curve showing the analog 0-10 V DC input of the SCU362 spectrometer control unit as a function of the kinetic energy of electron.97
3.5	The photoemission spectra of gold showing the Fermi edge.98
3.6	Photoemission spectra of gold and copper taken by using the new control and data acquisition system developed in this thesis work.99
3.7	The Auger spectrum of copper taken by using the new control and data acquisition system developed in this thesis work.100

LIST OF FIGURES (Continued)

Figure	Page
4.1	The intensity distribution of the light source in the BM4 bending magnet (a) at the source position and (b) at the distance of 7300 mm from the source obtained from ray-tracing simulations.....
	102
4.2	The intensity distribution of light beam on the surface of the pre-focusing mirror obtained from ray-tracing simulation.
	104
4.3	The simulated intensity distribution of synchrotron light at the position of the entrance slit of the monochromator.
	105
4.4	The intensity distribution of synchrotron light in the vertical direction measured at the entrance slit of the monochromator for the electron beam currents in the storage ring of 8 mA, 24 mA and 55 mA.
	107
4.5	<i>FWHM</i> of the synchrotron light beam in the vertical direction as a function of the electron beam currents measured on different dates with the same machine parameters for the operations of the light source.
	109
4.6	The intensity distribution of synchrotron light beam at position of the X-Y aperture when the entrance slit is widely opened.
	110
4.7	The intensity distribution of synchrotron light beam at position of the X-Y aperture when the width of the entrance slit is 200 micron.
	111

LIST OF FIGURES (Continued)

Figure	Page
4.8 The intensity distribution of synchrotron light beam on the surface of the focusing mirror when the entrance slit and the X-Y aperture are fully opened.	112
4.9 The distribution of the synchrotron light beam on the surface of the focusing mirror when the width of entrance slit is 200 micron and the X-Y aperture is fully opened.	113
4.10 The distribution of the synchrotron light beam on the surface of the focusing mirror when the width of entrance slit is 200 micron, the X-Y aperture is widely opened in horizontal direction and is 500 micron in the vertical direction.	114
4.11 The photo of the grating chamber showing the location of the monitoring pole and image of the light reflected from the focusing mirror incidents on the pole.	115
4.12 The intensity distribution of synchrotron light on the monitoring pole when the width of the entrance slit is 200 micron and the X-Y aperture is (a) fully open and (b) 500 micron in the vertical direction.	116
4.13 The intensity distributions of synchrotron light on the grating when the width of the entrance slit is 200 micron and the X-Y aperture is (a) fully opened and (b) 500 micron in the vertical direction.	119

LIST OF FIGURES (Continued)

Figure	Page
4.14	The intensity distribution of the 40 eV light beam at the exit slit of the monochromator when the width of the entrance slit is 200 micron and the X-Y aperture is (a) fully opened and (b) 500 micron in the vertical direction. 120
4.15	The intensity distribution of the 40 eV light beam on the post-focusing mirror when the widths of the entrance and exit slits are 200 micron and the X-Y aperture is (a) fully opened and (b) 500 micron in the vertical direction..... 123
4.16	The intensity distribution of the 40 eV light at the sample position when the widths of the entrance and exit slits are 200 micron and the X-Y aperture is (a) fully opened and (b) 500 micron in the vertical direction. 124
4.17	The wavelength calibration curves for VLSPG monochromator at the BL-4 beamline determined from the Fermi edge and 4f peaks of the gold spectra. 126
4.18	The values of photon energy of monochromatic light when using experimental and calculated calibration curves..... 127
4.19	PES spectra of gold taking with excitation photon energy of 40 eV using the CLAM2 spectrometer with the new data acquisition and control system..... 130

LIST OF FIGURES (Continued)

Figure	Page
4.20	The energy resolution obtained from ray tracing simulations with the width of the entrance and exit slit are 200 micron, the horizontal opening of the X-Y aperture is widely opened and the vertical opening of the X-Y aperture are 500 micron, 1000 micron, 1500 micron, 2000 micron, 2500 micron and fully opened.
	132
4.21	Photoemission spectra of gold near the Fermi edge. The spectra shown were from the fitted spectra of measurement data to illustrate the shift of Fermi edge when the middle of the vertical opening of the X-Y aperture was offset from the optical axis in the vertical direction.
	133
4.22	The energy distribution of monochromatized synchrotron light resolution obtained from ray tracing simulations with the widths of the entrance and exit slits are 200 micron, the horizontal opening of the X-Y aperture is fully opened and the vertical opening of the aperture is 500 micron. In the simulation, the misalignments of the focusing mirror in the vertical direction of -2 mm, -1 mm, 0 mm (no misalignment), 1 mm and 2 mm were considered.
	135

LIST OF FIGURES (Continued)

Figure	Page
4.23 The energy distribution of monochromatized light resolution obtained from ray tracing simulations with the widths of the entrance and exit slits are 200 micron, the horizontal opening of the X-Y aperture is fully opened and the vertical opening of the aperture is 500 micron. In the simulation, the misalignments of the focusing mirror in the vertical direction was +3 mm and the vertical offset of the X-Y aperture were -2 mm, -1 mm, 0 mm (no misalignment) and +1 mm.....	136
4.24 The energy distribution of monochromatized light resolution obtained from ray tracing simulations with the widths of the entrance and exit slits are 200 micron, the horizontal opening of the X-Y aperture is fully opened and the vertical opening of the aperture is 500 micron. In the simulation, the misalignments of the focusing mirror in the vertical direction was -3 mm and the vertical offset of the X-Y aperture were -1 mm, 0 mm (no misalignment), +1 mm and +2 mm.....	138
4.25 Photoemission spectra of the standard gold sample around the Fermi edge before and after the correction of the grating orientation. The spectra were taken with excitation energy of 40 eV, the entrance and exit slits were 200 micron and the X-Y aperture was fully opened.	140

LIST OF FIGURES (Continued)

Figure	Page
4.26	PES spectra of gold taking with excitation photon energy of 40 eV, entrance and exit slit widths are 200 micron using the CLAM2 spectrometer. These spectra are taken after the correction of the grating orientation.....
	141
4.27	The calculated and experimental resolving power of the monochromator using grating with $N_0 = 300$ lines/mm.
	144
4.28	The calculated and experimental resolving power of the monochromator using grating with $N_0 = 600$ lines/mm.
	145
4.29	The calculated and experimental resolving power of the monochromator using grating with $N_0 = 1200$ lines/mm.
	146
4.30	The photoemission spectrum of gold taken with the monochromatized light from the BL-4 beamline. The photon energy of the first order light was 40 eV. The grating with $N_0 = 300$ lines/mm was used as the dispersive element in the monochromator.
	148
4.31	The photoelectron yield of 6s band as a function of photon energy showing the magnitude of higher order light for grating with $N_0 = 300$ lines/mm.
	149
4.32	The photoelectron yield of 6s band as a function of photon energy showing the magnitude of higher order light for grating with $N_0 = 600$ lines/mm.
	150

LIST OF FIGURES (Continued)

Figure		Page
4.33	The photoelectron yield of 6s band as a function of photon energy showing the magnitude of higher order light for grating with $N_0 =$ 1200 lines/mm.	151

CHAPTER I

INTRODUCTION

1.1 Introductory Remark

This thesis work deals with the construction and commissioning of the BL-4 beamline of the Siam Photon Source of the National Synchrotron Research Center (NSRC) of Thailand. The BL-4 beamline is the first synchrotron light beamline at the Siam Photon Laboratory. The beamline employs a varied line-spacing plane grating (VLSPG) monochromator with three exchangeable VLSPG's. It delivers photons with energy between 20 eV and 240 eV for angle-resolved photoemission (ARPES) experiments as well as angle-integrated photoemission (AIPES) experiments. It is well-known that photoemission using synchrotron light is a very useful technique for investigating both atomic and electronic structures of matter. The knowledge of the atomic arrangement of a material is essential to understand its nature and function. The knowledge of the electronic structure is also indispensable to analyze the physical and chemical nature.

Commissioning of the first synchrotron light beamline is a challenging task. The situation is even more interesting for the BL-4 beamline, since everything involved in this work is the first experience to us. The main goal of the project to set up a Thai synchrotron light research facility, was to stimulate research activities in Thailand. This national project on synchrotron light research is named the Siam Photon Project. Different technologies related to particle accelerators and synchrotron light beamlines

were not established in Thailand when the Siam Photon Project started as mentioned above. Even now, there are still many things for researchers, engineers and graduate students at NSRC to learn. This is essential for them to overcome technical problems and difficulties related to the light source, beamlines and measurement systems. During the course of this thesis work, the instability of the electron beam caused by the broken coils in quadrupole magnets in the storage ring was observed. This trouble was cured and we can now carry out optical measurements in BL-4 beamline. In order to accomplish the commissioning of the BL-4 beamline, a new data acquisition system for AIPES measurements has been developed.

The optical design of the BL-4 beamline has been studied thoroughly. Ray-tracing simulations using a computer ray-tracing program have been carried out to obtain the deep understanding of the optics design. This is essential for the design work. The results from ray-tracing simulations were used not only for the optical designing but for the guidelines for the commissioning the beamline. In ray-tracing simulations, the influences of the mis-alignment of the optical elements on the quality of the synchrotron light beam could be studied. The results from the computer simulations have been compared with experimental results.

In this chapter, we describe the basic properties of synchrotron light, synchrotron light sources, and synchrotron light beamlines. In chapter II, the detailed information of the synchrotron light instrumentation and measurement techniques related to this thesis work will be given. Photoemission is also mentioned briefly in Chapter II though the main goal of this thesis is not to be concerned with photoemission techniques for the investigation of the electronic structure of matter. Photoemission measurements have been carried out for the calibration of the

instrument and for the performance test of the beamline. Chapter III reports the details of a new control and data acquisition system, which I have developed during this thesis work in order to carry out AIPES measurements for the energy calibration and the performance test of the monochromator. The results of the ray-tracing simulation and the beamline commissioning as well as discussion are given in Chapter IV. The conclusion of this thesis work is made in Chapter V.

1.2 Synchrotron Light

Synchrotron light is the electromagnetic wave emitted by relativistic charged particles (electrons or positron) traveling in a curve motion. As most of synchrotron light sources employ electrons, from now on, electrons are referred as the particles to emit synchrotron light. Synchrotron light is emitted in a very narrow beam, which is tangent to the circular path of the electrons. The first observation of man-made synchrotron light was reported by Elder and his coworkers at the General Electric Laboratory, New York, in 1947 (Elder, F.R., Langmuir, R.V., and Pollock, H.C., 1948). With the development of synchrotron light sources over the last two decades, synchrotron light has proved to have excellent characteristics as an excitation source of electron in matter. These outstanding characteristics are summarized as follows:

- (1) Synchrotron light emitted from a bending part of the electron orbit has a continuous spectrum. It covers a wide photon energy range from infrared to hard X-rays, depending on the energy of electrons. In case of synchrotron light produced by insertion devices such as wigglers or undulators, the spectrum is peak feature, depending on the magnetic field strength of the insertion device. Thus, synchrotron light can in principle be

tuned to meet requirements for specific experiments. More importantly, photon-energy dependent experiments such as absorption spectroscopy and resonant photoemission experiments can be carried out.

- (2) Synchrotron light is very highly brilliant. This is brought about by three causes: (i) The flux of emitted light is very high owing to the emission mechanism. (ii) The spatial divergence of emitted light beam is very low owing to the relativistic effect. (iii) The electron storage ring is so design that the cross section of the electron beam is small and the gradient of the electron trajectory with respect to the observation plane are low. The diameter of the cross section of the electron beam is often referred to as the beam size. Synchrotron light opens the possibility for photon-flux demanding experiments, for example, spin-resolved photoemission, ARPES and high resolution photoemission experiments. The brilliant of synchrotron light can further be increased by the installation of undulators. It should be noted that an electron beam with a beam diameter of a few tens micron can be attained in many advanced synchrotron light sources such as those at SPring-8, ESRF, BESSY II, ELLETRA, ALS, APS and NSRL.
- (3) Synchrotron light has a well defined time structure. In a storage ring, electrons are grouped in bunches which are moving synchronously to the phase of the radio frequency field employed to compensate the energy loss in the form of synchrotron light. This leads to the pulse structure of synchrotron light. This property of synchrotron light is used for time-resolved experiments.

- (4) The spectrum of synchrotron light can be predicted theoretically. The prediction is rigorous in the quantitative manner. Thus, in principle, the quantitative spectrum is calculated using a few known parameters such as the beam current, the beam energy and the radius of curvature (or the magnetic field strength). This opens the way that synchrotron light is used as a light intensity standard, particularly, in the region from the vacuum ultraviolet to the x-ray region.
- (5) Synchrotron light is highly polarized. Synchrotron light from bending portions and conventional insertion devices is linearly polarized in the orbital plane. It is elliptically polarized when viewed above or below the orbital plane. At present, specially designed insertion devices such as EPU (elliptical polarization undulator) and a helical undulator can generate elliptical polarized light. By using a retardation plate made of a thin crystal plate, circularly polarized x-rays are obtained.
- (6) Synchrotron light is produced without emitting contaminating gases to measurement system. It is as a clean source useful measurements. Experiments can be carried out at a 10^{-10} mbar or lower. This reduces the degradation of sample surfaces considerably.

1.3 Sources of Synchrotron Light

In designing optical beamlines, the state of the electrons beam in the storage ring must be taken into account because the size of the light source and the divergence of the light beam are crucially affected by the status of the electrons beam. The coordinate system which we consider for the electron motion in the storage ring is

illustrated in Figure 1.1. The x and y directions are the two orthogonal directions which are perpendicular to the direction of the electron motion “ s ”. dx/ds and dy/ds are the divergence of the electron trajectories around the ideal orbit in the x - s and y - s planes. We define the beam size and the beam divergence as $\sigma_x, \sigma_y, \sigma'_x$ and σ'_y .

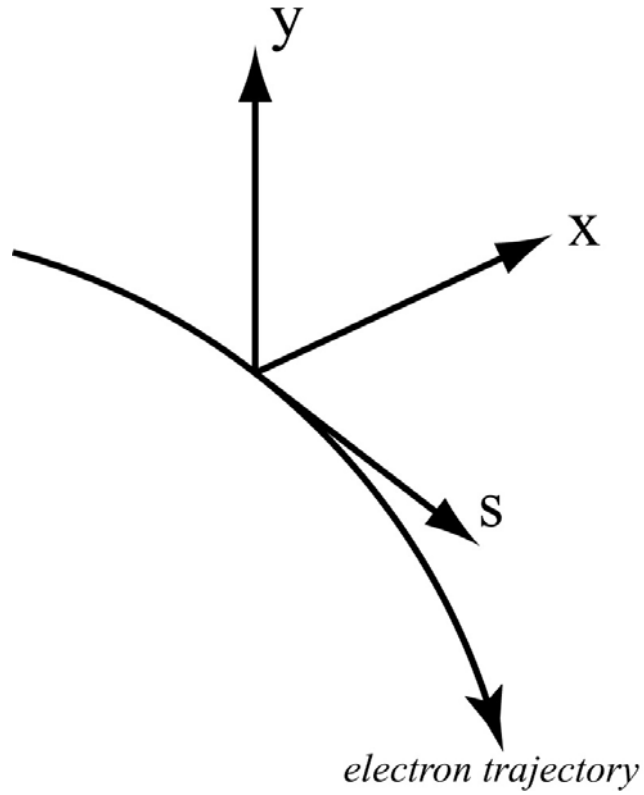


Figure 1.1 Coordinate system for the electron motion in a storage ring.

Since the electron beam is composed of many electrons circulating in the storage ring, it is formed as the bundle of many electron trajectories passing around the central orbit. The detailed analysis of the electron trajectory shows that the coordinate of the trajectory satisfies the following invariant relation:

$$\left. \begin{aligned} \varepsilon_{\xi} &= \gamma_{\xi}(s)\xi^2 + 2\alpha_{\xi}(s)\xi\xi' + \beta_{\xi}(s)\xi'(s) \\ \xi' &= \frac{d\xi}{ds} \\ \xi &= x \text{ or } y \end{aligned} \right\} \quad (1.1)$$

Here we have ignored the momentum deviation from a constant value. Parameters $\alpha_{\xi}(s)$, $\beta_{\xi}(s)$ and $\gamma_{\xi}(s)$ will be explained later. ε_{ξ} is a constant of the storage ring and is referred to as the emittance. The beam size is considered to be a quantity defined as root-mean-square value. We take the beam size as the maximum value of ξ , which is equal to $\sqrt{\varepsilon_{\xi}\beta_{\xi}}$.

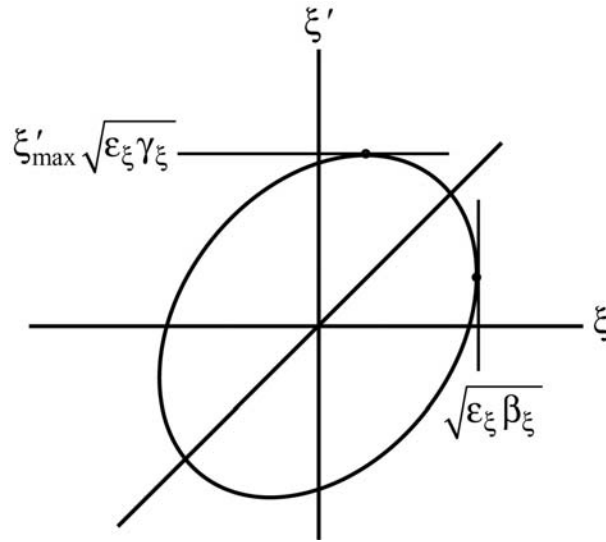


Figure 1.2 Phase space illustration of the electron beam shape.

Because of the coupling between the two orthogonal directions, it is useful to define a horizontal emittance, ε_x , and a vertical emittance, ε_y as follow:

$$\varepsilon_y = C \cdot \varepsilon_x \quad (1.2)$$

where C is the coupling factor, which is also an invariant of the storage ring. This coupling factor ranges between 0.01 and 0.1, depending on the alignment of the magnetic field in the storage ring. The causes of the imperfect alignment are from the imperfection of the manufacturing and misalignment of the magnets. With the perfect alignment, the coupling factor would be zero. In general, the vertical emittance is kept smaller than that in the ring plane making the vertical plane the logical one for dispersion in monochromators.

1.3.1 Electron Beam

The electron beam in a storage ring can be calculated when the parameters of the ring are known. If we solve the equation of motion of an electron in an idealized storage ring, we obtain the electron trajectory as

$$\xi(s) = \sqrt{\varepsilon_\xi \beta_\xi(s)} \cos \left[\int_0^s \frac{d\hat{s}}{\beta(\hat{s})} + \delta \right] \quad (1.3)$$

$\beta(s)$ is the parameter to be determined from the equation of motion. In practice, it satisfies

$$\frac{1}{2} \beta \beta'' - \frac{1}{4} \beta'^2 + k(s) \beta^2 = 1 \quad (1.4)$$

Here, $k(s)$ is the magnetic field strength parameter. The equation of motion is solved by changing the variable as

$$\zeta = \frac{\xi}{\sqrt{\beta(s)}} \quad (1.5)$$

Then the first integral of the equation of motion is given by

$$\varepsilon_\xi = \zeta^2 + \left(\frac{1}{\nu_\xi} \frac{d\zeta}{d\phi} \right)^2 \quad (1.6)$$

$$\left. \begin{aligned} \nu_\xi &= \frac{1}{2\pi} \int_0^L \frac{d\hat{s}}{\beta_\xi(\hat{s})} \\ \phi &= \frac{1}{\nu_\xi} \int_0^s \frac{d\hat{s}}{\beta_\xi(\hat{s})} \end{aligned} \right\} \quad (1.7)$$

L is the circumference of the trajectory. ε_ξ is a constant characterizing the storage ring. δ is a phase constant.

From (1.3) we find that the electron trajectory oscillating around the central orbit. Obviously, $\sqrt{\varepsilon\beta}$ is a factor representing the amplitude of the oscillation in accordance with the comment made regarding the beam size.

In (1.2), we use parameter $\alpha_\xi(s)$ and $\gamma_\xi(s)$ in addition to $\beta_\xi(s)$. They are defined as

$$\left. \begin{aligned} \alpha_x &= -\frac{1}{2} \cdot \frac{d\beta_x(s)}{ds} \\ \alpha_y &= -\frac{1}{2} \cdot \frac{d\beta_y(s)}{ds} \\ \gamma_x(s) &= \frac{1 + \alpha_x(s)^2}{\beta_x(s)} \\ \gamma_y(s) &= \frac{1 + \alpha_y(s)^2}{\beta_y(s)} \end{aligned} \right\} \quad (1.8)$$

The important parameters $\alpha_\xi(s)$, $\gamma_\xi(s)$ and $\beta_\xi(s)$ are called the Twiss parameters. Another important parameter is the dispersion, $\eta(s)$. It is defined as

$$\Delta\xi = \eta(s) \frac{\delta p}{p_0} \quad (1.9)$$

This indicates the amount of the shift of the trajectory when the beam energy changes

as $\frac{dE}{E_0} = \frac{\delta p}{p_0}$, where p is the momentum of the electron.

$\beta_x(s)$ and $\beta_y(s)$ are referred to as the horizontal and vertical betatron functions, respectively. The betatron functions reflect the focusing characteristics of the magnet lattice of the storage ring. They are constant in the straight section but vary strongly in the bending portion. The electron beam size and its divergence can be obtained from the following relationships:

$$\sigma_x(s) = \sqrt{\varepsilon_x \beta_x(s) + [\eta_x(s)(\delta p / p_o)]^2} \quad (1.10)$$

$$\sigma'_x(s) = \sqrt{\varepsilon_x \gamma_x(s) + [\eta'_x(s)(\delta p / p_o)]^2} \quad (1.11)$$

$$\sigma_y(s) = \sqrt{\varepsilon_y \beta_y(s) + [\eta_y(s)(\delta p / p_o)]^2} \quad (1.12)$$

$$\sigma'_y(s) = \sqrt{\varepsilon_y \gamma_y(s) + [\eta'_y(s)(\delta p / p_o)]^2} \quad (1.13)$$

The horizontal dispersion, η_x , is the results from the energy or momentum spread of the electrons. The vertical dispersion, η_y , is zero when there is no misalignment of the magnetic field in the storage ring. That is not the case in practice. However, the vertical dispersion may be approximated to be zero at the straight section of the storage ring. The momentum spread varies from one storage ring to another. However, its value is in the range of 10^{-3} , or lower for low electron beam currents.

1.3.2 Bending Magnet

Synchrotron light from bending magnets occurs in a narrow cone of nominal angular width $\sim 1/\gamma$ and sweeps around the curvature path of the electrons, as illustrated in Figure 1.3. The dimension of the light source produced in a bending magnet is defined by the electron beam size and the angle of emission of the synchrotron light. The angle of the emission can be resolved into the horizontal and vertical angles, σ'_v and σ'_h respectively. The vertical angle of emission is photon-energy (wavelength) dependent, which is given by the following formula:

$$\sigma'_v(\text{mrad}) = \frac{570}{\gamma} \left(\frac{\lambda}{\lambda_c} \right) \quad \text{for } 0.2 < \frac{\lambda}{\lambda_c} < 100 \quad (1.14)$$

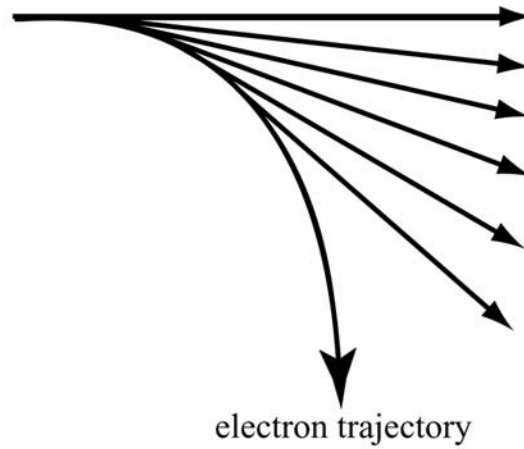
$$\lambda_c(\text{nm}) = 0.559 \rho / E^3 = 1.86 / BE^2 \quad (1.15)$$

$$\gamma = 1957 \cdot E \text{ (the reduced energy)} \quad (1.16)$$

$$\rho(\text{m}) = 3.335 E / B \quad (1.17)$$

where E is the energy of the electrons in GeV, B is the magnetic field in *Tesla* (T) and ρ is the radius of curvature of the electron trajectory in the bending magnet in meter (m). It is obvious from the above formula that the photons with high energy concentrate near the plane of the storage ring. The horizontal angle of emission of synchrotron light in bending magnets to be utilized at the experimental station of the beamline is defined by the geometry of the opening aperture in the front-end of the beamline. For large horizontal opening angle, the effective electron beam width increases.

(a) Top view



(b) Side view

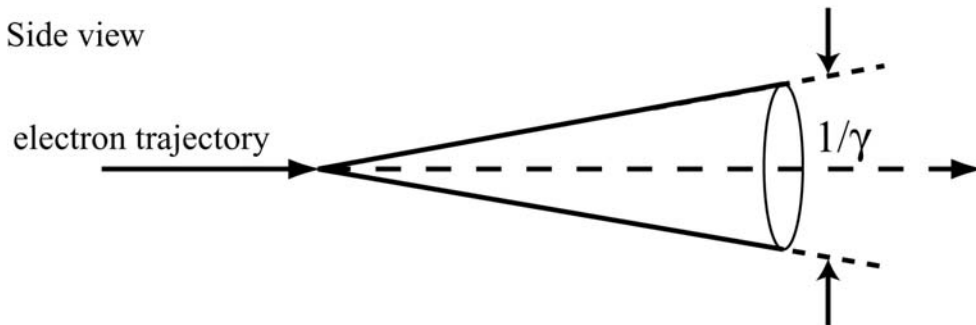


Figure 1.3 Emission of synchrotron light from bending magnets: (a) top view and (b) side view.

Electrons traveling around the storage ring lose energy by emitting synchrotron light. Thus, an RF cavity is installed in the ring to restore the lost energy. The power loss of the electrons in each revolution is given by

$$P_{total} (kW) = 88.5 I E^4 / \rho = 26.5 E^3 I B \quad (1.18)$$

where I is the electron beam current.

The spectral distribution of the power emitted synchrotron light from the bending magnet is given by

$$P(W/(mrad \cdot 1\%BW)) = 5.95 \times 10^{-15} \left(\frac{\gamma^4 I}{\rho} \right) G_2 \left(\lambda / \lambda_c \right) \quad (1.19)$$

Where
$$G_2 = \left(\lambda / \lambda_c \right)^2 \int K_{5/3}(\eta) d\eta \quad (1.20)$$

$G_2(\lambda / \lambda_c)$ is the integral over a Bessel function of the second kind (Krinsky, Perlman, and Weston, 1983). The photon flux is given by the following:

$$\text{Photon flux (photons/(s} \cdot \text{mrad} \cdot 1\%BW))} = \gamma \cdot I \cdot F(\lambda / \lambda_c) \quad (1.21)$$

where $F(\lambda / \lambda_c)$ is the modified Bessel function (Krinsky, Perlman, and Weston, 1983). Synchrotron light from bending magnets is 100% linearly polarized in the plane of the storage ring. Above and below the plane, it is elliptically polarized.

1.3.3 Insertion Devices

Synchrotron light from insertion devices is different from that of bending magnets in magnitude, spectral shape, and in spatial and angular size. Wigglers are used for shifting the synchrotron light toward short wavelength region while undulators are normally used for increasing the brightness. With current technology, more undulators have been constructed for producing synchrotron light with elliptical polarization.

In an ordinary undulator or wiggler, the stored electrons pass through a magnetic field which varies approximately sinusoidally in the vertical plane. This results in an approximately sinusoidal motion of the electron in the horizontal plane.

The electrons motion in the insertion devices is characterized by the deflection parameter K , which is given by

$$K = \frac{e\lambda_o B_o}{2\pi mc} = 0.934 B_o \lambda_o \quad (1.22)$$

where λ_o is the period of the sinusoidal magnetic field in centimeter and B_o is the magnetic field amplitude in *Tesla*. The periodic magnetic structure is called a wiggler when K is large ($K \gg 1$). It is called an undulator when K is moderate ($K \leq 1$).

Spectral shape of synchrotron light from wigglers and undulators is somewhat more complicated than that from bending magnets. Typical spectra of synchrotron light from the insertion devices are shown in Figure 1.5. The wavelength of synchrotron light from a wiggler is given by

$$\lambda = \frac{\lambda_o}{2\gamma^2 k} \left(1 + \frac{K^2}{2} + \gamma^2 \theta^2 \right) \quad (1.23)$$

where θ is the observation angle with respect to the unperturbed orbit and k is the number of the odd harmonic. The total power lost in a wiggler in the form of synchrotron light is given by

$$P_{total}(W) = 6.33 E^2 B^2 L \cdot I \quad (1.24)$$

where $L = \lambda_o \cdot N$ is the total length of the wiggler in centimeter and N is the number of period.

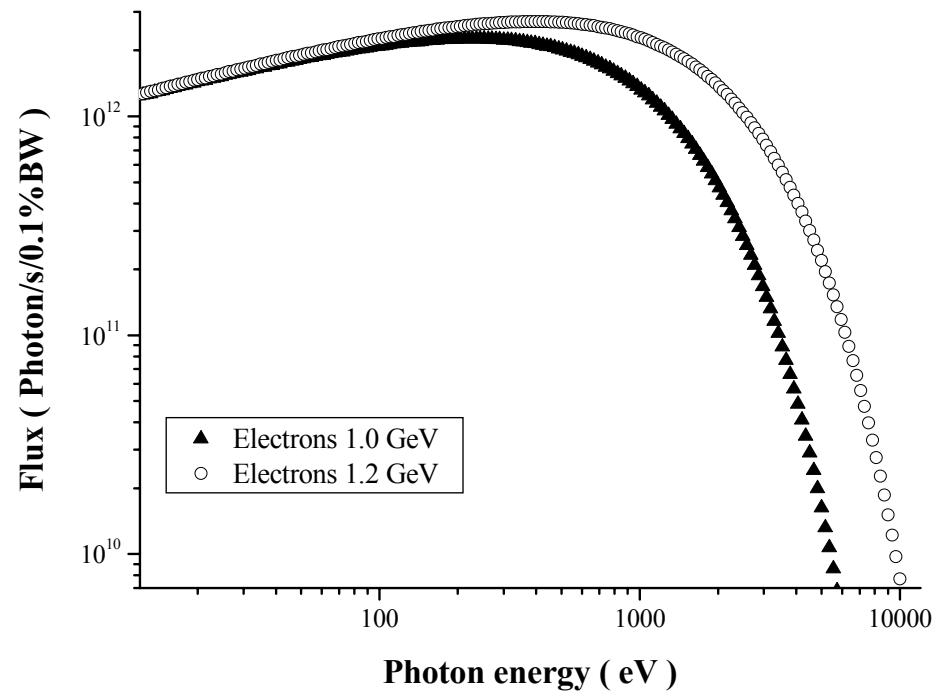
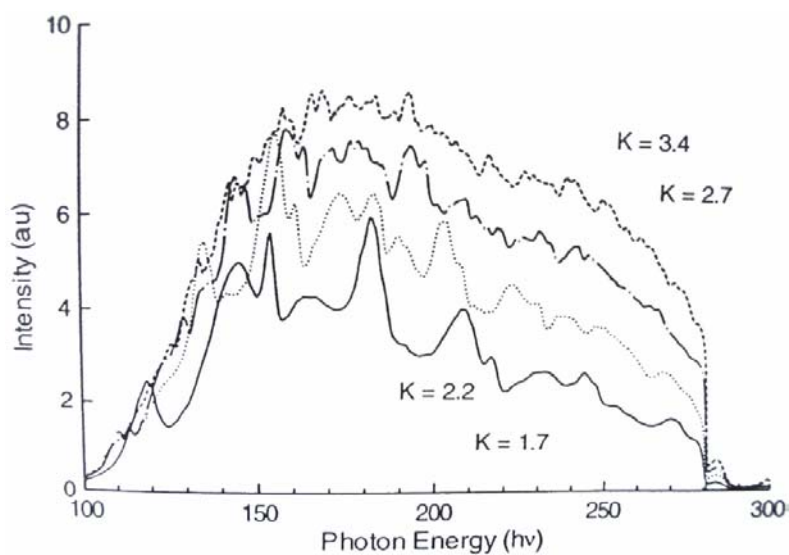
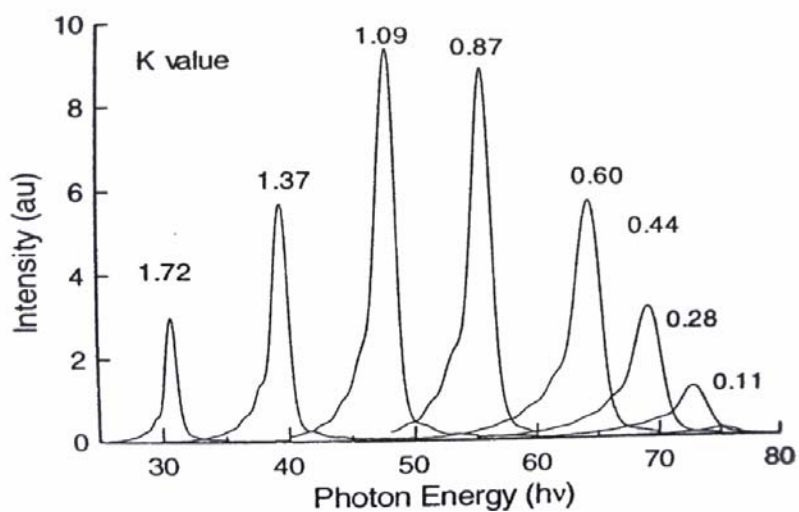


Figure 1.4 The spectrum of synchrotron light produced from 1.0 GeV and 1.2 GeV electrons in a bending magnet with a radius of 2.78 m.



(a) Typical wiggler spectra



(b) Typical undulator spectra

Figure 1.5 Typical spectra of synchrotron light produced by (a) a wiggler and (b) an undulator.

1.4 Synchrotron Light Beamlines

1.4.1 Definition of Synchrotron Light Beamline

A beamline, or synchrotron light beamline, is a photon delivery system that begins at the storage ring vacuum chamber and extends onto the experimental floor to include the experimental station. A beamline might have multiple branch optical beamlines to accommodate different optical instrumentation. Each branch optical beamline might have multiple end-stations to optimize time sharing of the synchrotron light beam. Figure 1.6 shows the schematic drawing of beamline components. The three major beamline components are a front-end, branch optical beamlines and end-stations.

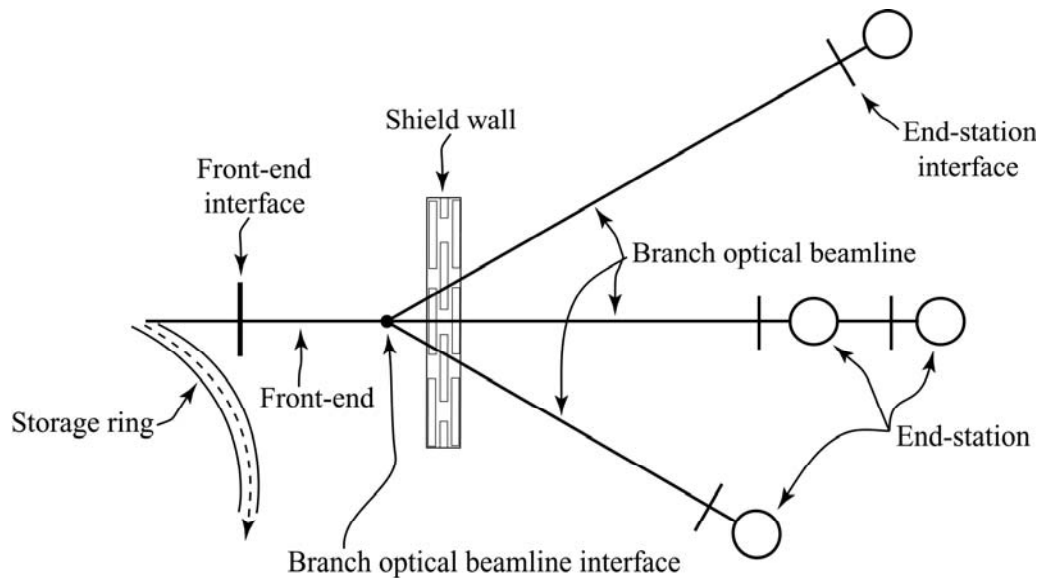


Figure 1.6 The major components of synchrotron light beamlines.

The front-end begins at the storage ring vacuum chamber and end at the branch optical beamline interface, which is generally located immediately downstream (toward the experimental station) from the bremsstrahlung shutter at the shield wall. Each beamline has one front-end shared by all branch optical beamlines. The major front-end components are masks, vacuum valves, a heat absorber and a bremsstrahlung shutter. Masks are used for allowing a partial of synchrotron light beam to downstream components while protecting the downstream components from thermal damage. A heat absorber is a water-cooled photon shutter. Its function is to interrupt transmission of the synchrotron light beam. Vacuum valves are used for vacuum-isolate different sections of the front-end. A bremsstrahlung shutter is used for providing bremsstrahlung radiation shielding for branch optical beamlines. Normally, the bremsstrahlung shutter is located as close to the radiation shield wall as possible for effective radiation shield.

An (branch) optical beamline consists of optical elements and mechanical components, which begins at the interface to the front-end and ends at the first component of the experimental station. The optical beamline is used to filter, focus and monochromatize synchrotron light. The main optical elements are focusing mirrors and a monochromator. The optical beamline also include beam diagnostic components and vacuum components.

The end-station, or experimental station, is connected to the downstream end of the (branch) optical beamline. The configuration of experimental station varies depending on the type of experiments being conducted.

1.4.2 Synchrotron Light Optics

1.4.2.1 The Optical Path

Understanding of the mathematical treatment of the focusing properties of a grating or mirror surface is important for the design of advanced synchrotron light beamlines. In the VUV and soft X-rays regions, conventional refracting type of optical elements cannot be used because the absorption coefficient for all materials in these regions is very high. Thus, the grazing incidence reflection type of the optical elements is used. When the grazing angles are used in conjunction with mirrors of various shapes, the resolving powers critically depend on image quality and hence on controlling the aberrations or deviation from a perfect image. Thus, understanding optical aberrations is required in order to design a path which will maintain the brilliance of the source as well as possible. The aberrations results from differences in the possible optical paths from one point to another via some geometrical surfaces.

P. de Fermat has provided the principle of least time in 1657 to explain the phenomena of refraction and reflection. The Fermat's principle postulates that the optical path from point A to point B must be an extremum. The application of Fermat's principle to the light path function is illustrated in Figure 1.7, where rays of light from the point A impinge on an optical surface $P(\xi, \omega, l)$ and form an image at point B . The calculation of focusing or imaging properties is carried out by the use of analytical formulas for the optical path function F , which can be written as

$$F = \overline{AP} + \overline{PB} + G \quad (1.25)$$

where G is the groove function introduced to cope with the physical optics of diffraction. All paths via the mirror surface $P(\xi, \omega, l)$ which lead to a focus must fulfill the following:

$$\frac{\partial F}{\partial \omega} = 0 \quad (\text{meridional focus}), \quad (1.26)$$

$$\frac{\partial F}{\partial \ell} = 0 \quad (\text{sagital focus}). \quad (1.27)$$

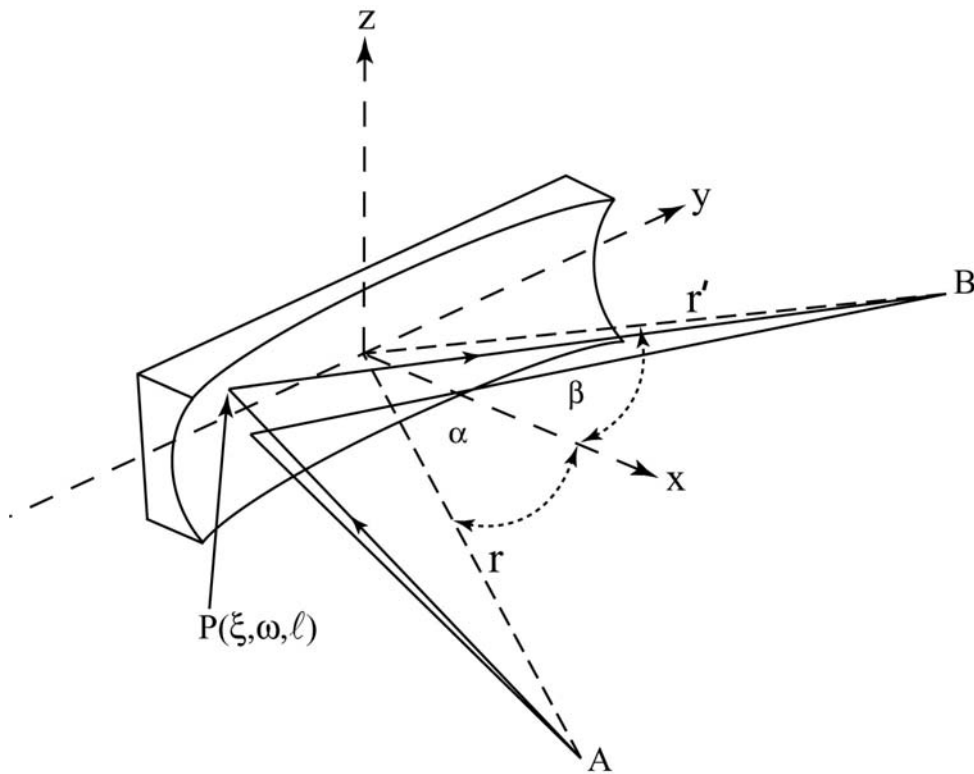


Figure 1.7 Light rays from the source A incident on a surface $P(\xi, \omega, \ell)$ and form an image at B .

The general form of the surface can be expressed by the equation

$$\xi = \sum_{i=0}^{\infty} \sum_{j=0}^{\infty} a_{ij} \omega^i l^j \quad (1.28)$$

and $a_{00} = a_{10} = 0$; $j = \text{even}$ as dictated by the choice of origin and the fact that the x - y plane is a symmetry plane. The a_{ij} coefficients for toroidal, paraboloid, ellipsoidal and plane surfaces are given in Table 1.1. The conventional definitions of those surfaces are given in Figure 1.8.

The distance of \overline{AP} and \overline{PB} are expressed in polar coordinate by

$$\overline{AP} = \sqrt{r_1^2 + w^2 + l^2 - 2wr_1 \sin \alpha} \quad (1.29)$$

$$\overline{PB} = \sqrt{r_2^2 + w^2 + l^2 - 2wr_2 \sin \beta} \quad (1.30)$$

Substituting equations (1.28), (1.29) and (1.30) into equation (1.25), the light path function is then expressed into a power series of w and l by

$$\begin{aligned} F = & F_{000} + wF_{100} + \frac{1}{2}w^2F_{200} + \frac{1}{2}l^2F_{020} + \frac{1}{2}w^3F_{300} + \frac{1}{2}wl^2F_{120} + \frac{1}{8}w^4F_{400} + \frac{1}{4}w^2l^2F_{220} \\ & + \frac{1}{8}l^4F_{040} + lF_{011} + wlF_{111} + \frac{1}{2}wF_{102} + \frac{1}{4}w^2F_{202} + \frac{1}{2}w^2lF_{211} + \dots \end{aligned} \quad (1.31)$$

where the important F_{ijk} terms are given below (Noda, Namioka, and Seya, 1974).

$$F_{000} = r + r' \quad (1.32)$$

$$F_{100} = Nk\lambda - (\sin \alpha + \sin \beta) \quad (\text{grating equation}) \quad (1.33)$$

$$F_{200} = \left(\frac{\cos^2 \alpha}{r} \right) + \left(\frac{\cos^2 \beta}{r'} \right) - 2a_{20}(\cos \alpha + \cos \beta) \quad (\text{meridional focus}) \quad (1.34)$$

$$F_{020} = \frac{1}{r} + \frac{1}{r'} - 2a_{20}(\cos \alpha + \cos \beta) \quad (\text{sagittal focus}) \quad (1.35)$$

$$F_{300} = \left[\frac{T(r, \alpha)}{r} \right] \sin \alpha + \left[\frac{T(r', \beta)}{r'} \right] \sin \beta - 2a_{30}(\cos \alpha + \cos \beta) \quad (\text{primary coma}) \quad (1.36)$$

$$F_{120} = \left[\frac{S(r, \alpha)}{r} \right] \sin \alpha + \left[\frac{S(r', \beta)}{r'} \right] \sin \beta - 2a_{12}(\cos \alpha + \cos \beta) \quad (\text{astigmatic coma}) \quad (1.37)$$

$$F_{400} = \frac{4T(r, \alpha)}{r^2} \sin^2 \alpha - \frac{T^2(r, \alpha)}{r} + \frac{4T(r', \beta)}{r'^2} \sin^2 \beta - \frac{T^2(r', \beta)}{r'} - 8a_{30} \left[\frac{1}{r} (\sin \alpha \cos \alpha) + \frac{1}{r'} (\sin \beta \cos \beta) \right] - 8a_{40}(\cos \alpha + \cos \beta) + 4a_{20}^2 \left[\frac{1}{r} + \frac{1}{r'} \right] \quad (1.38)$$

$$F_{220} = \frac{2S(r, \alpha)}{r^2} \sin^2 \alpha + \frac{2S(r', \beta)}{r'^2} \sin^2 \beta - \frac{T(r, \alpha)S(r, \alpha)}{r} - \frac{T(r', \beta)S(r', \beta)}{r'} + 4a_{20}a_{02} \left[\frac{1}{r} + \frac{1}{r'} \right] - 4a_{22}(\cos \alpha + \cos \beta) - 4a_{12} \left[\frac{1}{r} (\sin \alpha \cos \alpha) + \frac{1}{r'} (\sin \beta \cos \beta) \right] \quad (1.39)$$

$$F_{040} = 4a_{02}^2 \left[\frac{1}{r} + \frac{1}{r'} \right] - 8a_{04}(\cos \alpha + \cos \beta) \quad (1.40)$$

$$F_{011} = -\frac{z}{r} - \frac{z'}{r'} \quad (1.41)$$

$$F_{111} = -\frac{z \sin \alpha}{r^2} - \frac{z' \sin \beta}{r'^2} \quad (1.42)$$

$$F_{102} = \frac{z^2 \sin \alpha}{r^2} + \frac{z'^2 \sin \beta}{r'^2} \quad (1.43)$$

$$F_{202} = \left(\frac{z}{r} \right)^2 \left[\frac{2 \sin^2 \alpha}{r} - T(r, \alpha) \right] + \left(\frac{z'}{r'} \right)^2 \left[\frac{2 \sin^2 \beta}{r'} - T(r', \beta) \right] \quad (1.44)$$

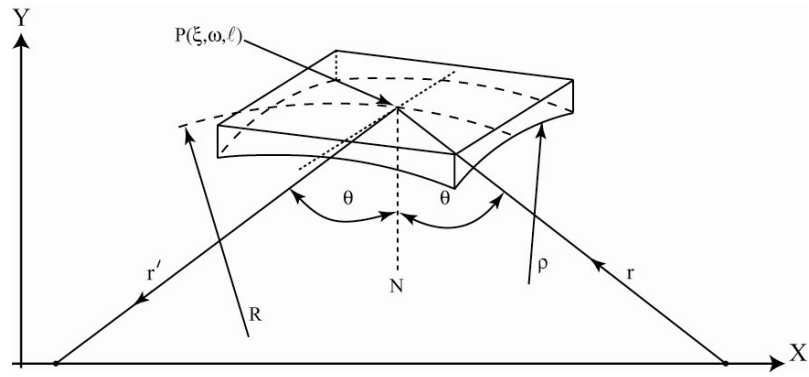
$$F_{211} = \frac{z}{r^2} \left[T(r, \alpha) - \frac{2 \sin^2 \alpha}{r} \right] + \frac{z'}{r'^2} \left[T(r', \beta) - \frac{2 \sin^2 \beta}{r'} \right] \quad (1.45)$$

...

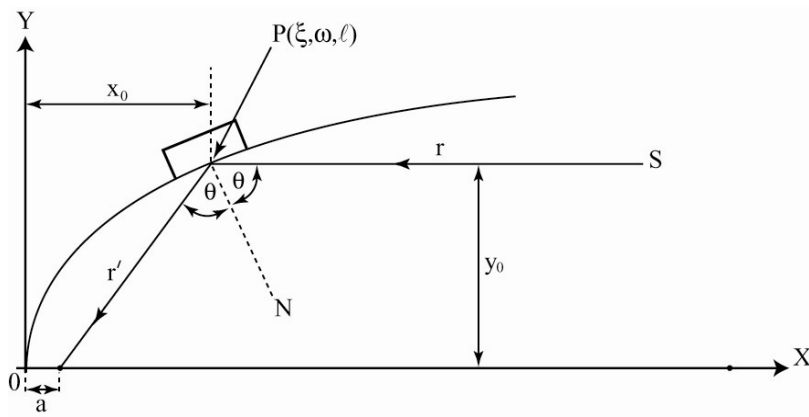
...

where $T(r, \alpha) = (\cos 2\alpha / r) - 2a_{20} \cos \alpha$ and $S(r, \alpha) = (1/r) - 2a_{02} \cos \alpha$ and with analogous expression for $T(r', \beta)$ and $S(r', \beta)$. N is the groove density of a classical grating. k is the order of diffraction.

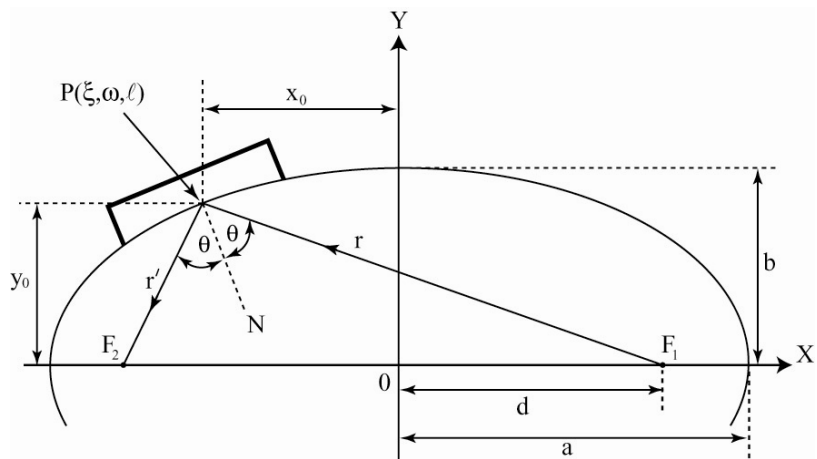
An optical system is aberration-free when all F_{ijk} terms vanish, which is not the case for VUV and soft X-ray optics. This is due to the grazing incidence geometry employed. In most optics designs, the first seven terms are thus considered to suppress high-order aberrations.



(a) toroid



(b) paraboloid



(c) ellipsoid

Figure 1.8 The definition of the parameters for different surfaces.

Table 1.1 The coefficients of a_{ij} for toroid, paraboloid and ellipsoid surfaces.

a_{ij}	Toroid	Paraboloid	Ellipsoid
a_{02}	$\frac{1}{2\rho}$	$\frac{1}{4r'\cos\theta}$	$\frac{1}{4f\cos\theta}$
a_{04}	$\frac{1}{8\rho^3}$	$\frac{\sin^2\theta}{64r'^3\cos^3\theta}$	$\frac{b^2}{64f^3\cos^3\theta}\left[\frac{\sin^2\theta}{b^2}+\frac{1}{a^2}\right]$
a_{12}	0	$-\frac{\tan\theta}{8r'^2}$	$\frac{\tan\theta}{8f^2\cos\theta}(e^2-\sin^2\theta)^{1/2}$
a_{20}	$\frac{1}{2R}$	$\frac{\cos\theta}{4r'}$	$\frac{\cos\theta}{4f}$
a_{22}	$\frac{1}{4R^2\rho}$	$\frac{3\sin^2\theta}{32r'^3\cos\theta}$	$\frac{\sin^2\theta}{16f^3\cos^3\theta}\left[\frac{3}{2}\cos^2\theta-\frac{b^2}{a^2}\left(1-\frac{\cos^2\theta}{2}\right)\right]$
a_{30}	0	$-\frac{\sin\theta\cos\theta}{8r'^2}$	$\frac{\sin\theta}{8f^2}(e^2-\sin^2\theta)^{1/2}$
a_{40}	$\frac{1}{8R^3}$	$\frac{5\sin^2\theta\cos\theta}{64r'^3}$	$\frac{b^2}{64f^3\cos\theta}\left[\frac{5\sin^2\theta\cos^2\theta}{b^2}-\frac{5\sin^2\theta}{a^2}+\frac{1}{a^2}\right]$

1.4.2.2 Mirrors

Mirrors for the VUV and soft X-ray optics are different from those for the visible light. This is due the fact that photons in these spectral ranges interact strongly with all materials, even air. Thus, the optical system has to be under vacuum. The reflectivity of the optical materials can be increased only by increasing the angle of incidence. Normally, the angles of incidence are close to 90° and that the mirrors are used in a grazing incidence configuration. It is well-known that the grazing-incidence instruments introduce problems with astigmatism and other aberrations and is not the geometry of choice.

The generalized Fresnel equation for reflection provides information of the relation between the optical constants of a surface, the angle of incidence and the reflectivity. The reflectivity of the component whose electric field vector is perpendicular (R_s) and parallel (R_p) are respectively given below:

$$R_s = [(a - \cos \theta)^2 + b^2] / [(a + \cos \theta)^2 + b^2] \quad (1.46)$$

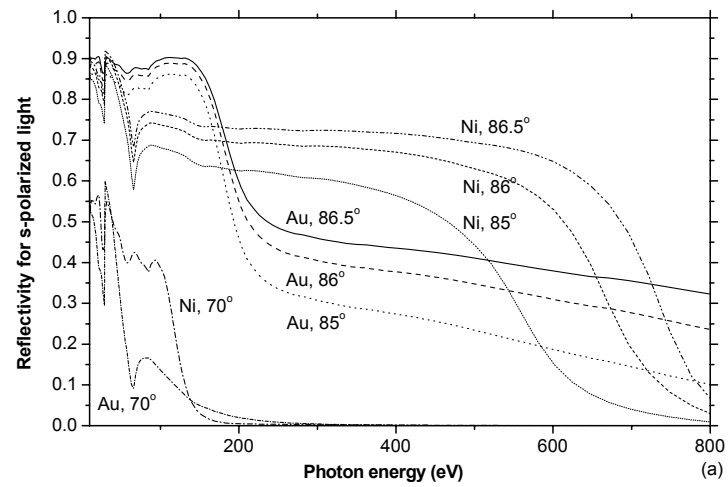
$$R_p = R_s [(a - \sin \theta \tan \theta)^2 + b^2] / [(a + \sin \theta \tan \theta)^2 + b^2] \quad (1.47)$$

where θ is the angle of incidence with respect to the surface normal,

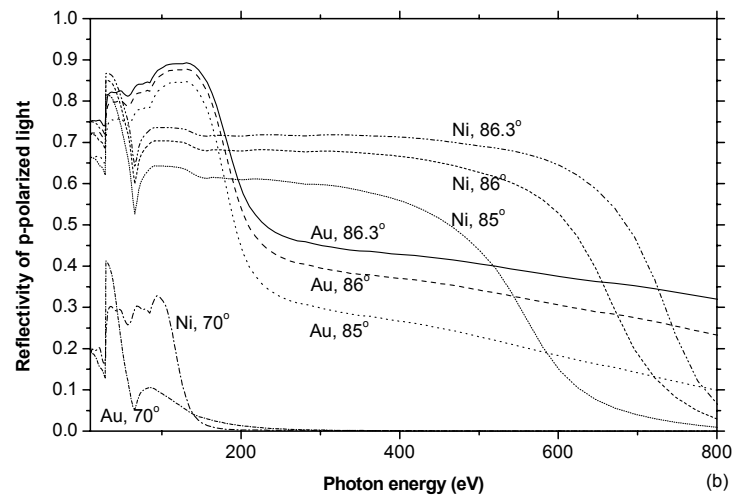
$$a^2 = 0.5 \{ [(n^2 - k^2 - \sin^2 \theta)^2 + 4n^2 k^2]^{0.5} + (n^2 - k^2 - \sin^2 \theta) \}, \quad (1.48)$$

$$b^2 = 0.5 \{ [(n^2 - k^2 - \sin^2 \theta)^2 + 4n^2 k^2]^{0.5} - (n^2 - k^2 - \sin^2 \theta) \}. \quad (1.49)$$

n and k are the real and imaginary parts of the complex index of refraction. Thus the reflectivity can be calculated if the optical constants are known. The calculated reflectivity from the above formulas is in good agreement with measurements for commonly used optical materials such as gold, platinum, nickel, carbon and silicon carbide. Figure 1.9 shows the reflectivity of gold and nickel as a function of photon energy for different angles of incidence.



(a) s-polarized light



(b) p-polarized light

Figure 1.9 Reflectivity of gold and nickel as a function of photon energy for the angles of incidence of 86.5°, 86°, 85° and 70° for (a) s-polarized light and (b) p-polarized light.

The images created by mirrors used in the VUV and soft X-ray region are never perfect. This is due to the intrinsic optical aberrations resulting from the grazing incidence geometry. Single-sphere focusing systems suffer inherently from spherical aberrations, astigmatism, line curvature, distortion and coma. Even an ellipsoidal surface has no vanished aberrations terms. For a given optical system, the intrinsic aberrations can be minimized only by the compensation of the aberrations of the optical elements in the system, i.e. the aberration of one element is reduced by another.

An example of a combine mirrors system to reduce the aberrations is the Kirkpatrick-Baez design of a two-mirror system (Kirkpatrick and Baez, 1948). The Kirkpatrick-Baez system consists of two focusing mirrors oriented perpendicular to each other, as shown in Figure 1.10, to allow the beam independently focused in the two orthogonal planes. The two mirrors are normally toroidal mirrors, which provide no coupling for the focusing properties in the two planes. Spherical mirrors can also be used in the Kirkpatrick-Baez configuration. In such a case, small coupling between the two planes exists. The degree of the coupling depends on the angle of incidence. In advanced synchrotron light beamline, this type of the mirror system is used as the pre-focusing mirror system to reflect the beam into the monochromator. With this design, it is possible to optimize the geometry, the figure accuracy and the heat load aspects in the dispersive plane of the monochromator, the resolution determining plane.

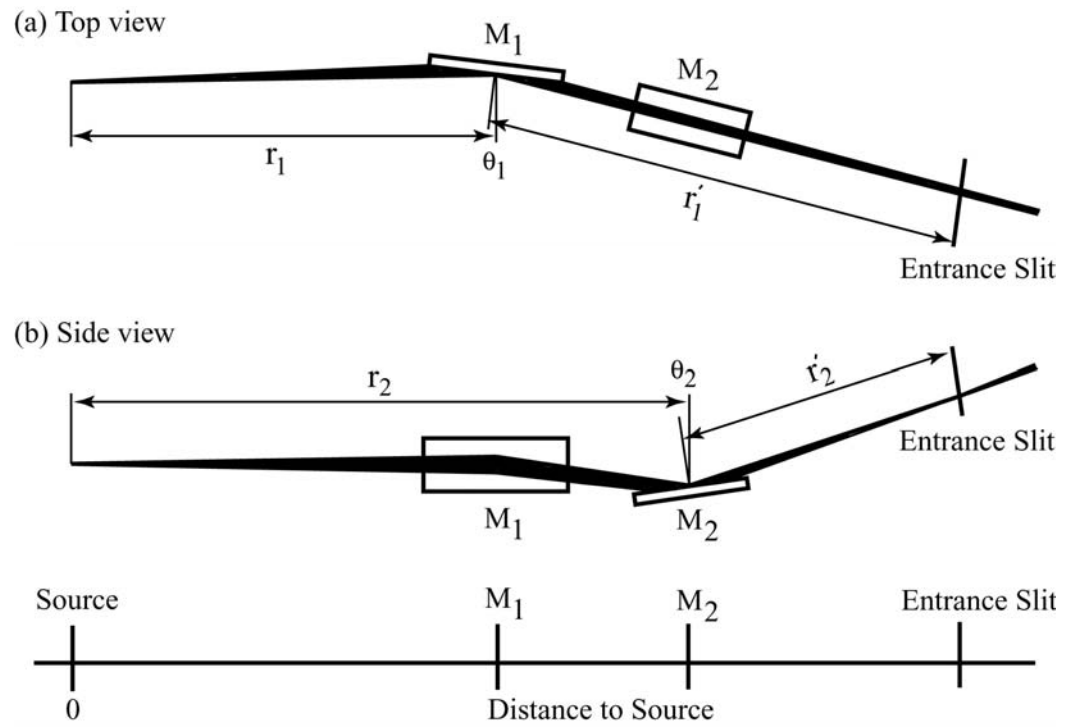


Figure 1.10 The Kirkpatrick-Baez mirror system (Kirkpatrick and Baez, 1948).

It is well-known that the influence of tangent error of a mirror on the sagittal focusing properties of that mirror is reduced by the factor of $\sin\theta_g$, where θ_g is the grazing angle of incidence on the mirror, which is typically $2^\circ - 5^\circ$ and thus $\sin\theta_g$ is $0.035 - 0.087$. The influence of the tangent error is reduced by the factor of $28 - 11$. When the Kirkpatrick-Baez design is adopted, the first mirror is aligned to focus the beam in the plane perpendicular to the dispersive plane of the monochromator. It is known that the first mirror absorbs the largest heat load, which might cause the geometry error in addition to the manufacturing deficiencies. Thus the focusing properties of the first mirror might greatly deviate from the design values. However, it does not have big influence on the resolution of the beamline as the focusing plane is not in the diffractive plane of the monochromator. The second mirror of the Kirkpatrick-Baez system focuses the beam in the resolution determining plane of the monochromator, and thus it should maintain an especially high geometrical accuracy of its reflecting surface to provide the beam with minimized aberrations.

Many beamlines require very small size of the beam at the position where experiments to be conducted. The size of the beam depends on the total focusing power of the focusing optical elements in the beamline. “Demagnification” is a parameter to indicate the degree of how much the size of the beam can be reduced. The higher values of the demagnification of the focusing elements are used, the smaller beam size is obtained. However, there is a limit for the reduction of the size of the beam. This is due to the fact that VUV and soft X-ray optics employs grazing incidence geometry, in which the optical aberrations are enhanced when the demagnification increases.

Imperfection of the manufacturing processes introduces the deficiencies to the optical elements that can degrade the performance of the optical systems. Figure error, or slope error, and roughness are the major imperfections that can increase the optical aberrations of the optical system. With advance technology, the slope error of the surfaces of optical elements for synchrotron light beamline can be suppressed below 1 arcsec. The roughness of the surfaces, which cause the diffusion of light beam, can be kept below 5 Å.

1.4.2.3 Gratings

A reflecting type of gratings is used as diffractive optical elements in most VUV and soft X-ray synchrotron light beamlines. A few exceptional beamlines employ Fresnel zone plates, a circular transmission grating. Diffraction gratings are usually used in the monochromators while Fresnel zone plates are used for in focusing system. In this section, the optical path function will be applied to the analysis of the relations between the optical aberrations and the resolution of a diffraction grating. For a simple grating with constants groove density, the F_{100} term of the optical path function is the grating equation, i.e.

$$kN\lambda = \sin \alpha + \sin \beta . \quad (1.50)$$

The sign convention for the diffraction angle β is shown in Figure 1.11. The angle α and β have opposite sign if they are on opposite side of the normal. The order of diffraction k is negative order, or outside order, when the angle β is greater than that of the zero-order beam.

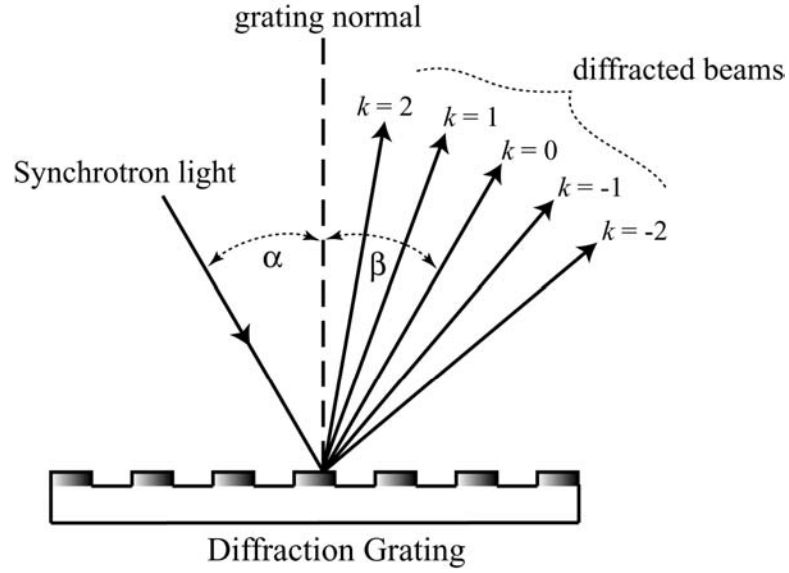


Figure 1.11 A diffraction grating showing the diffraction orders.

Noda and co-worker have developed the geometrical theory of diffraction grating based on the optical path function (Noda, Namioka, and Seya, 1974). In order to demonstrate the relations between the optical aberrations and the resolution of the beamline/monochromator, a toroidal grating is chosen. Other surfaces commonly employed in beamline such as plane, spherical and cylindrical surfaces are treated as the special cases, e.g. a spherical surface ($\rho = R$), a cylindrical (either ρ or $R = \infty$) and a plane surface ($\rho = R = \infty$). For a general case, the density of the groove is a function of ω , i.e.

$$N(\omega) = N_0(1 + a_1\omega + a_2\omega^2 + a_3\omega^3 + \dots) \quad (1.51)$$

where N_0 is the groove density at the center of the grating and a_i ($i = 1, 2, 3, \dots$) are the space variation parameters. For gratings with a constant groove density, all space variation parameters vanish. The optical path, F , can be rewritten as:

$$F = \overline{AP} + \overline{PB} + k\lambda \int_0^\omega N(\omega) d\omega \quad (1.52)$$

Considering on the $k\lambda \int_0^\omega N(\omega) d\omega$ term:

$$k\lambda \int_0^\omega N(\omega) d\omega = k\lambda N_0 \left(\omega + \frac{1}{2} a_1 \omega^2 + \frac{1}{3} a_2 \omega^3 + \frac{1}{4} a_3 \omega^4 + \dots \right) \quad (1.53)$$

Substitution of the grating terms in the optical path function, the most important F_{ijk} terms are expressed by:

$$F_{000} = r + r' \quad (1.54)$$

$$F_{100} = Nk\lambda - (\sin \alpha + \sin \beta) \quad (1.55)$$

$$F_{200} = \frac{\cos^2 \alpha}{r} + \frac{\cos^2 \beta}{r'} + k\lambda N_0 a_1 \quad (1.56)$$

$$F_{300} = \frac{\sin \alpha \cos^2 \alpha}{r^2} + \frac{\sin \beta \cos^2 \beta}{r'^2} + \frac{2}{3} k\lambda N_0 a_2 \quad (1.57)$$

$$F_{120} = \frac{\sin \alpha}{r^2} + \frac{\sin \beta}{r'^2} \quad (1.58)$$

$$F_{400} = \frac{\cos^2 \alpha}{r^3} (4 \sin^2 \alpha - \cos^2 \alpha) + \frac{\cos^2 \beta}{r'^3} (4 \sin^2 \beta - \cos^2 \beta - \cos^2 \beta) + 2k\lambda N_0 a_3 \quad (1.59)$$

The relation between the optical aberrations and the resolution, $\Delta\lambda/\lambda$ or $\Delta E/E$, is as the follow:

$$\frac{\Delta\lambda}{\lambda} = \frac{1}{Nk\lambda} \left[\omega F_{200} + l F_{020} + \frac{3}{2} \omega^2 F_{300} + \frac{1}{2} l^2 F_{120} + \frac{1}{2} \omega^3 F_{400} + \dots \right] \quad (1.60)$$

The major F_{ijk} terms are F_{200} , F_{300} , F_{120} and F_{400} , which are called defocus, coma, astigmatic and spherical aberration, respectively. The contribution of different types of the optical aberrations to the resolution, $\Delta\lambda/\lambda$, can explicitly be written as follow:

$$\left. \frac{\Delta\lambda}{\lambda} \right|_{Defocus} = \frac{W}{Nk\lambda} F_{200} \quad (1.61)$$

$$\left. \frac{\Delta\lambda}{\lambda} \right|_{Coma} = \frac{3}{2} \frac{W^2}{Nk\lambda} F_{300} \quad (1.62)$$

$$\left. \frac{\Delta\lambda}{\lambda} \right|_{Astigmatic} = \frac{1}{2} \frac{L^2}{Nk\lambda} F_{120} \quad (1.63)$$

$$\left. \frac{\Delta\lambda}{\lambda} \right|_{Spherical} = \frac{1}{2} \frac{W^3}{Nk\lambda} F_{400} \quad (1.64)$$

It is obvious that the total resolution cannot be zero for the whole energy range of the monochromator. However, it is possible to minimize the total resolution by making different optical aberrations vanished at certain photon energy, as will be illustrated in Chapter II in the optics design of the BL-4 beamline.

For a VLSPG monochromator, the spacing variation parameters of VLSPG are obtained through the minimization of the optical aberrations. When two values of photon energy are selected to make the defocusing term vanished, i.e.

$$F_{200}(E_1) = F_{200}(E_2) = 0. \quad (1.65)$$

One can find the spacing variation parameter a_1 and the exit arm length of VLSPG, r_2 , through the following relationships:

$$a_1 = \frac{-1}{k\lambda_1 N_0} \left(\frac{\cos^2 \alpha_1}{r_1} + \frac{\cos^2 \beta_1}{r_2} \right) \quad (1.66)$$

$$r_2 = \frac{\lambda_2 \cos^2 \beta_1 - \lambda_1 \cos^2 \beta_2}{\lambda_1 \cos^2 \alpha_2 - \lambda_2 \cos^2 \alpha_1} r_1 \quad (1.67)$$

The spacing variation parameters a_2 and a_3 can be obtained by making the coma and spherical aberration terms vanished at photon energies E_3 and E_4 , respectively. We obtain

$$a_2 = \frac{-3}{2k\lambda N_0} \left(\frac{\sin \alpha \cos^2 \alpha}{r_1^2} + \frac{\sin \beta \cos^2 \beta}{r_2^2} \right) \quad (1.68)$$

$$a_3 = \frac{-1}{2k\lambda N_0} \left(\frac{\cos^2 \alpha}{r_1^3} (4 \sin^2 \alpha - \cos^2 \alpha) + \frac{\cos^2 \beta}{r_2^3} (4 \sin^2 \beta - \cos^2 \beta) \right) \quad (1.69)$$

In addition to the contribution of the major optical aberrations, the figure slope error of the grating and the slit width are also important contributions limiting the resolution of the monochromator. The contribution of the figure slope error of the grating to resolution is given as

$$\Delta\lambda/\lambda|_{slope} = (4.7\sigma_{se} \cos \beta)/\lambda Nk \quad (1.70)$$

where σ_{se} and β are the *root-mean-square (rms)* figure slope error of the grating and the angle of diffraction, respectively. The slit limited resolution can be derived directly from the grating equation. The resolution defined by the entrance and exit slit are given as

$$\frac{\Delta\lambda}{\lambda} = \frac{1}{Nk\lambda} \left(\frac{\Delta S_1}{r} \cos \alpha \right) \quad (\text{Entrance slit}) \quad (1.71)$$

$$\frac{\Delta\lambda}{\lambda} = \frac{1}{Nk\lambda} \left(\frac{\Delta S_2}{r'} \cos \beta \right) \quad (\text{Exit slit}) \quad (1.72)$$

Where ΔS_1 and ΔS_2 are the width of the entrance and exit slits, respectively.

1.4.2.4 Monochromators

Monochromator is a system of optical elements that can resolve photons with different energies. It is an essential system of optical beamlines that provide monochromatic light for different experiments. The designs of monochromator vary with photon energy range. Even at the same photon energy range, different types of monochromator have been used. There has been a big progress in the development of VUV and soft X-ray monochromators over the last twenty years so that some types of the monochromators with admirable performance in the past are no longer being built. The choice of a monochromator is always a delicate one as well as the design because there are many aspects have to be carefully considered such as photon energy range, resolution, photon flux, beam size and divergence, the grating type and number of grating, higher order light suppression, the optical components, space available for the beamline and including the cost of the entire beamline (Peatman, 1997).

VUV and soft X-ray monochromators are based on the reflection type of diffraction gratings operated in the grazing incidence geometry (Johnson, 1983). This is due to the fact that it is not possible to use the conventional refracting type because of the strong absorption of electromagnetic wave by all materials in this wavelength region. The grazing incidence geometry is required so that the reflectivity of the materials of the optical element is enhanced.

There are different ways to classify VUV and soft X-ray monochromators. Monochromators may be classified according to their shape of the reflecting surface as plane grating monochromator, spherical grating monochromator and toroidal grating monochromator. The monochromators may also be classified according to the included angle, $\alpha - \beta$, i.e. constant and varied included angle

monochromators. Monochromators with a constant included angle at the grating have been constructed for many beamlines in different synchrotron light research facilities. This is because of the mechanical simplicity for their photon energy scanning systems. The energy scanning can be done simply by a rotation of the grating about a line at the center of the grating and perpendicular to the dispersive plane. There are a big variation of monochromators in this class for examples; toroidal/spherical grating monochromator (Dietz, Braun, Bradshaw, and Johnson, 1985; Chen and Sette, 1989), plane grating monochromator (Itou, Harada, and Kita, 1989), the Seya-Namioka monochromator (Namioka and Seya, 1970) and nearly all aberration-reduced holographic spherical/plane grating monochromators (Koike and Namioka, 1997). The monochromator employed in the BL-4 beamline, VLSPG monochromator (Songsiriritthigul, 2001), is also in this class.

Monochromators with a varied included angle at the grating offer high performance. This class of monochromators includes the popular Grasshopper and Extended Range Grasshopper (ERG) monochromators. Most monochromators in this type employ the constant angle of incidence geometry. From the grating equation, the relationship between photon energy and the diffraction angle can be obtained when the angle of incidence is fixed. A monochromator in this type covers a wide range of photon energy. This is due to the increase of degree of freedom of the photon energy scanning mechanism. Thus, the mechanical motion of the scanning system is complicated, consisting of more than one motions of the mirror or/and grating.

CHAPTER II

INSTRUMENTATION AND TECHNIQUES

This Chapter provides information of the instrumentation such as the light source, beamline and the experimental station employed during the course of this thesis work. The techniques used in this work will also be mentioned. This work has been carried at the Siam Photon Laboratory of the National Synchrotron Research Center, Thailand. The main work of thesis is the development and commission of the BL-4 beamline, which is the first beamline at the Siam Photon Laboratory. The BL-4 beamline utilizes synchrotron light source from the bending magnet of the storage ring of the Siam Photon Source. The beamline is originally designed to deliver photons generated by the BM4 bending magnet of the storage ring to the end station for ARPES experiments. The optics design, photon scanning mechanism and the experimental station will be mentioned in details because the information of these three parts is necessary for the development of the data acquisition and control system for the beamline and for the interpretation and discussion of the results obtained during the commissioning of the beamline. The front-end part of the beamline, which is the interface between the optical beamline and the storage ring, will briefly be mentioned. Computer ray-tracing simulations have also been carried out to assist the beamline alignment and to verify the experimental results.

2.1 Siam Photon Source

The Siam Photon Source is the first synchrotron light source modified from the light source donated by the SORTEC Cooperation in Japan (Kengkan, Pairsuwan, Isoyama, and Ishii, 1988). The original machine was designed for lithographic research for microelectronics industry. The Siam Photon Source consists of two main parts, i.e. the storage ring and the injection system. Figure 2.1 shows the schematic diagram of the Siam Photon Source. The storage ring is installed on the ground-level floor while the injection system is in the under ground hall. The detailed information of the two parts is given below.

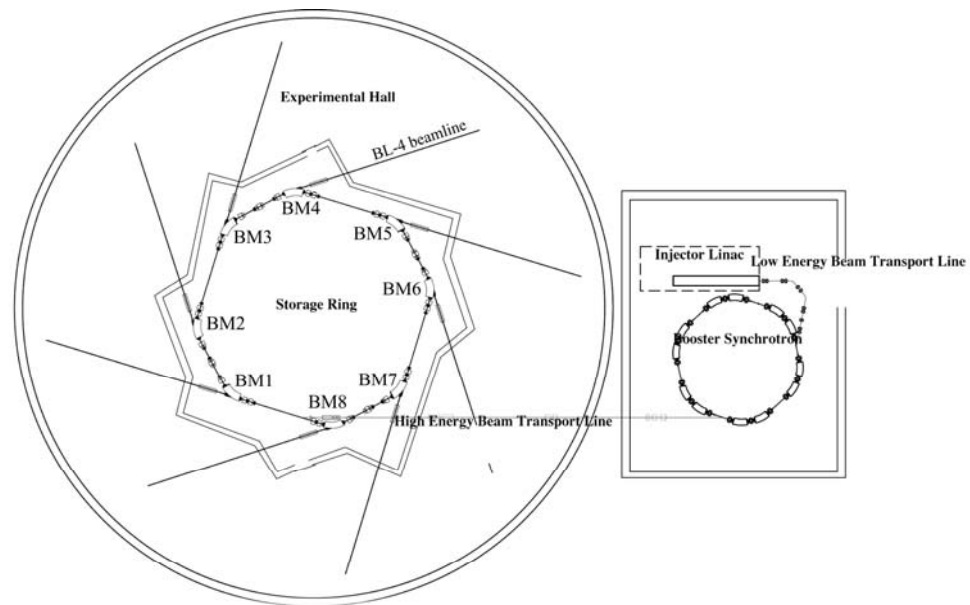


Figure 2.1 The schematic diagram of the Siam Photon Source.

2.1.1 Injection System

The injection system consists of a linear accelerator (LINAC), a low energy transport line (LBT), a booster synchrotron and a high energy beam transport line (HBT). The only part of the injection system that has been modified from the original machine is HBT (Pairsuwan and Ishii, 2003). This is due to the fact that the storage ring of the original machine was installed in the same floor as the injection system. The rest of the injection system is used without any modifications.

The injection system produces 1 GeV electrons beam and inject into the storage ring. The electrons produced at the electron gun of LINAC are accelerated in resonant cavities of LINAC up to energy of ~ 40 MeV and then transported via LBT into the booster synchrotron. The electrons are accelerated further in the synchrotron by gaining more energy in the RF acceleration cavity of the synchrotron until the energy of the electrons reaches 1 GeV. The high energy electrons are transported via HBT and injected into the storage ring located on the ground-level floor. The specifications of the synchrotron are summarized in Table 2.1.

2.1.2 Storage Ring

The storage ring of the Siam Photon Source is considered as a new ring. The design of the ring is totally different from that of the original SORTEC machine. In general, the new ring provides synchrotron light for broader research areas. To achieve that goal, the quality of the electrons beam had to be improved. The size of the ring has been increased almost double while the emittance of the electron beam was reduced from $500 \text{ nm}\cdot\text{mrad}$ to $74 \text{ nm}\cdot\text{mrad}$. This provides better quality beam of synchrotron light. The straight sections of the new ring allow installation of insertions devices such as wigglers and undulators.

The storage ring of the Siam Photon Source design employs the double bend achromat (DBA) magnet lattice with four-fold symmetry. The DBA lattice is shown in Figure 2.2. The dimensions shown in the figure are in millimeter. The total length of the four lattices, the circumference of the ring, is 81.3 meters (Sanguansak et al., 2002). There are four long straight sections and four short straight sections. The long sections are for installation of insertion devices. The specifications of the DBA lattice and storage ring are given in Tables 2.2 and 2.3, respectively.

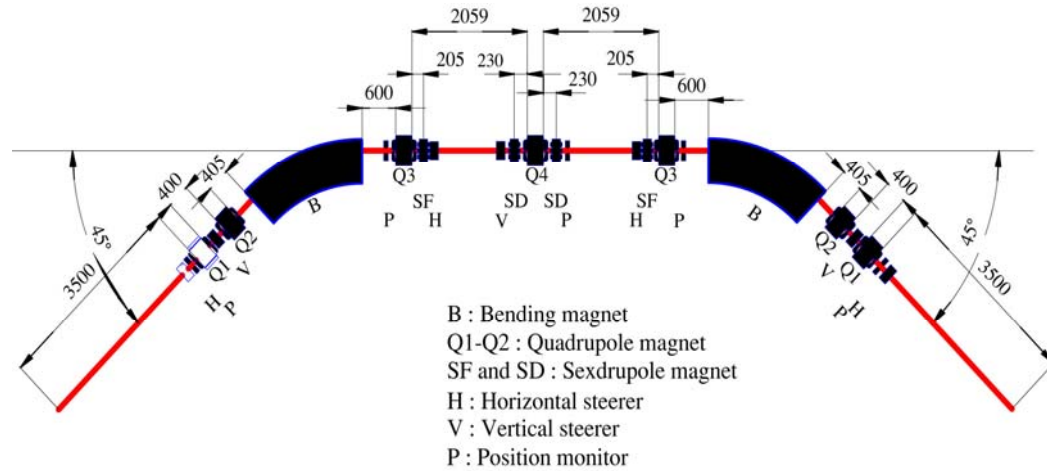


Figure 2.2 The DBA lattice of the storage ring of the Siam Photon Source.

Table 2.1 The specifications of the booster synchrotron of the Siam Photon Source

Initial energy	40 MeV
Final energy	1 GeV
Circumference	43.19 m
Radius of curvature	3.03 m
Magnet lattice	FODO
Electron beam current	30 mA
Repetition rate	1.25 Hz
Betatron tune (ν_x/ν_y)	2.25/1.25
Maximum field of bending magnet	1.1 T
Magnetic field gradient of quadrupole magnet	4.8 T/m
RF frequency	118 MHz
Maximum RF voltage	60 kV
Vacuum pressure during operation	$< 1 \times 10^{-6}$ mbar

Table 2.2 The specifications of the DBA lattice of the storage ring of the Siam Photon Source.

<i>Bending magnets B</i>	
Type	sector bend
Quantity	8
Deflection angle	45°
Radius of curvature	2.78 m
Maximum field	1.2 T
<i>Quadrupole magnets Q1-Q4</i>	
Quantity	28
Pole length	0.29 m
Maximum field gradient $ dB_z/dx $	13 T/m
<i>Sextupole magnet SF, SD</i>	
Quantity; <i>SF, SD</i>	8, 8
Pole length; <i>SF, SD</i>	0.15, 0.2 m
maximum field gradient $ d^2B_z/dx^2 $	60 T/m ²

Table 2.3 The specifications of the storage ring of the Siam Photon Source.

Energy	1 GeV
Circumference	81.3 m
Type of magnet lattice	DBA
Superperiodicity	4
Length of long straight sections	7 m \times 4
Betatron wave numbers; ν_x, ν_y	4.76, 2.82
Momentum compaction factor	$\alpha = 0.0214$
Natural chromaticities; ξ_x, ξ_y	7.59, -6.73
Natural emittance	74π nm rad
Damping partition number; J_x, J_y, J_ϵ	0.9, 1.0, 2.1
Damping time; $\tau_x, \tau_y, \tau_\epsilon$	18.9, 17.0, 8.1 ms
RF frequency	118 MHz
Maximum RF volage	100 kV
Harmonic number	32
Critical energy	0.8 keV

Figure 2.3 shows the horizontal and vertical betatron functions and the horizontal dispersion function of the DBA lattice. The betatron functions are relatively constant in the straight sections and are varied strongly in the magnets. The horizontal dispersion function vanishes at the straight sections. The vertical dispersion is zero for the perfect alignment of the magnetic field. For all storage rings, the vertical dispersion cannot be kept at the zero value because of the filed errors cause by the imperfection of magnet manufacturing and of the alignment.

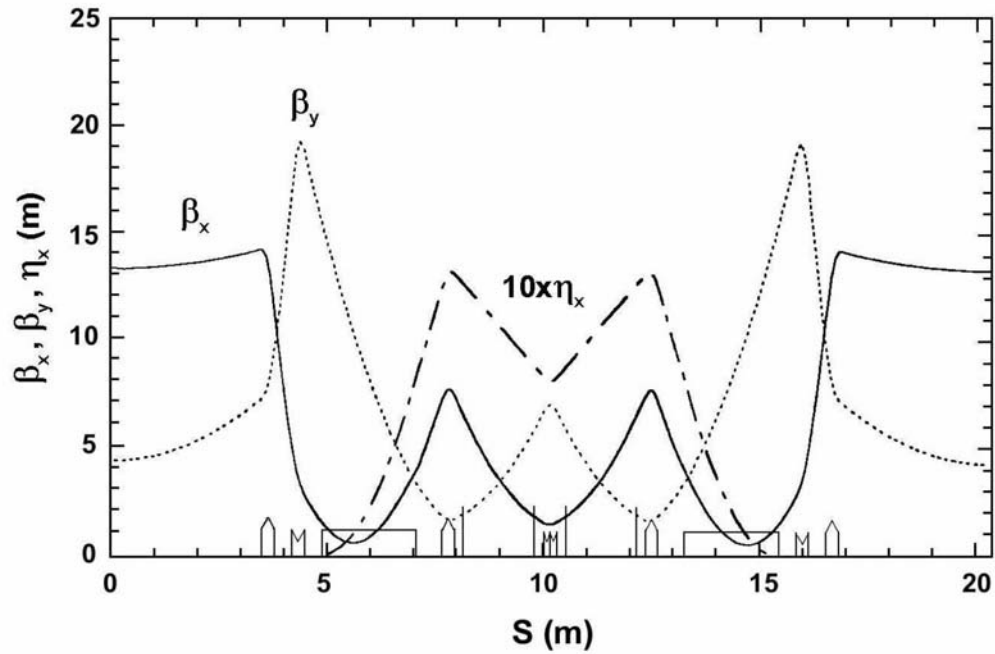


Figure 2.3 The vertical and horizontal betatron functions and the horizontal dispersion function of the DBA lattice of the storage ring of the Siam Photon Source.

Figure 2.4 shows the calculated spectra of synchrotron light from the bending magnet, undulator and wiggler for the Siam Photon Source. With 1 GeV electrons, synchrotron light from the bending magnet of the Siam Photon Source is mostly in the VUV and soft X-ray spectral ranges. The critical energy of synchrotron light from the bending magnet is 0.8 keV. Higher intensity of VUV can be obtained from a planar undulator, which has already been purchased from DanFysik (Denmark). The brilliance of the first and third harmonics synchrotron light from the undulator is more than four orders of magnitude higher than that from the bending magnet. Such light is required for photon-flux demanding experiments such as high-energy resolution spectroscopy. The figure also shows that hard X-ray can also be obtained from a 1 GeV storage ring when a superconductor magnet wiggler (SMW) with very high field is used. For a 7.5 tesla SMW, sufficient intensity of the hard X-rays with ~ 1 Å wavelength can be obtained.

The storage ring has eight beam channels. Thus eight beamlines, with or without branch optical beamline, can be constructed. Four beam channels at the four bending magnets (BM2, BM4, BM6 and BM8) located downstream of the short straight sections are used for the beamlines that utilize synchrotron light from the bending magnets. While the other four beam channels are planned for insertion device beamlines.

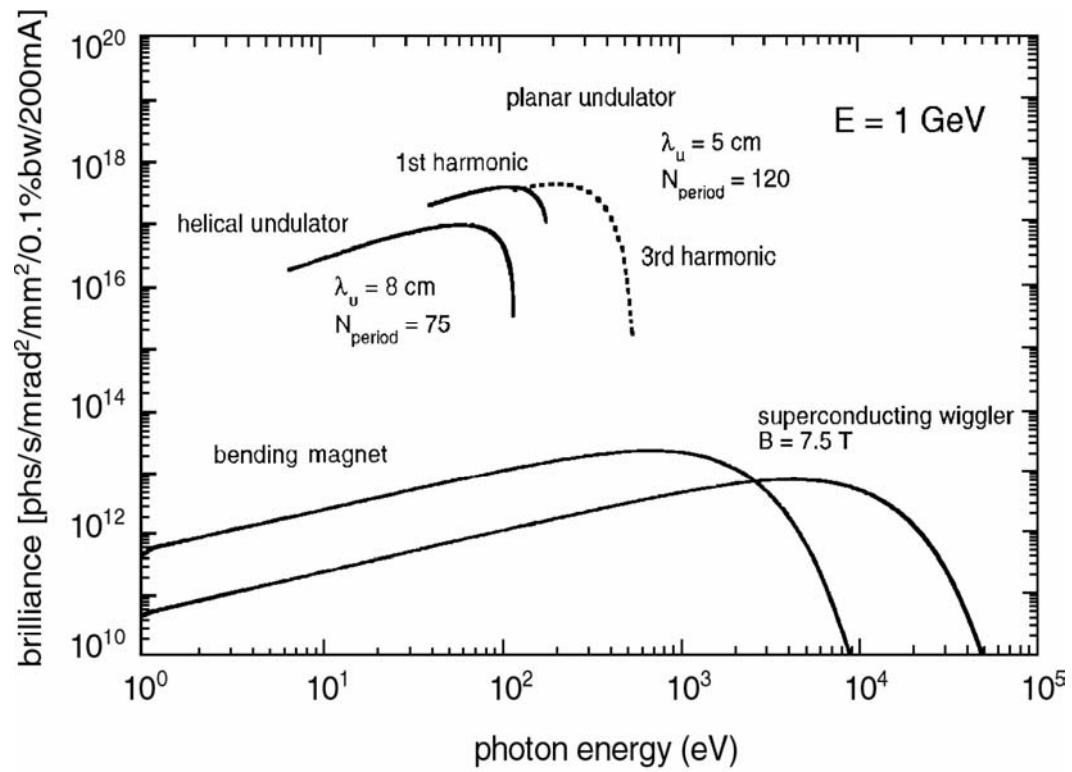


Figure 2.4 The calculated spectra of synchrotron light from the bending magnet, undulator and wiggler for the Siam Photon Source.

2.2 BL-4 Beamline

2.2.1 Front-end

The front-end of the BL-4 beamline is connected to the beam channel of the vacuum chamber of the BM4 bending magnet of the storage ring. The front-end serves primarily to prevent damage to the storage ring and radiation hazards to the users of the beamline. The front-end design of the BL-4 beamline is rather simple. The top and side views of the design drawings of the front-end are shown in Figure 2.5. The main components of the front-end are vacuum valves, a heat absorber (ABS), two masks (Mask I and Mask II), and a beam shutter (BS). ABS is a water-cooled photon shutter. Its function is to interrupt transmission of the synchrotron-light beam. It is made of OFHC copper to assure good thermal conductivity. The front face of ABS is aligned 45° with respect to the beam axis. Thus, the reflected synchrotron-radiation beam will be incident on a water-cooled CF flange. The water-cooled copper Mask I is located just in front of ABS. It is used for protecting the downstream components from thermal damage. The solid angle, or the opening angle, of the synchrotron-light beam is defined by Mask II, which has the acceptance angles of 3 mrad and 5 mrad in the horizontal and vertical directions, respectively. BS is used for providing bremsstrahlung radiation shielding for the beamline. Thus BS is always located as close to the radiation shield wall as possible for effective radiation shield.

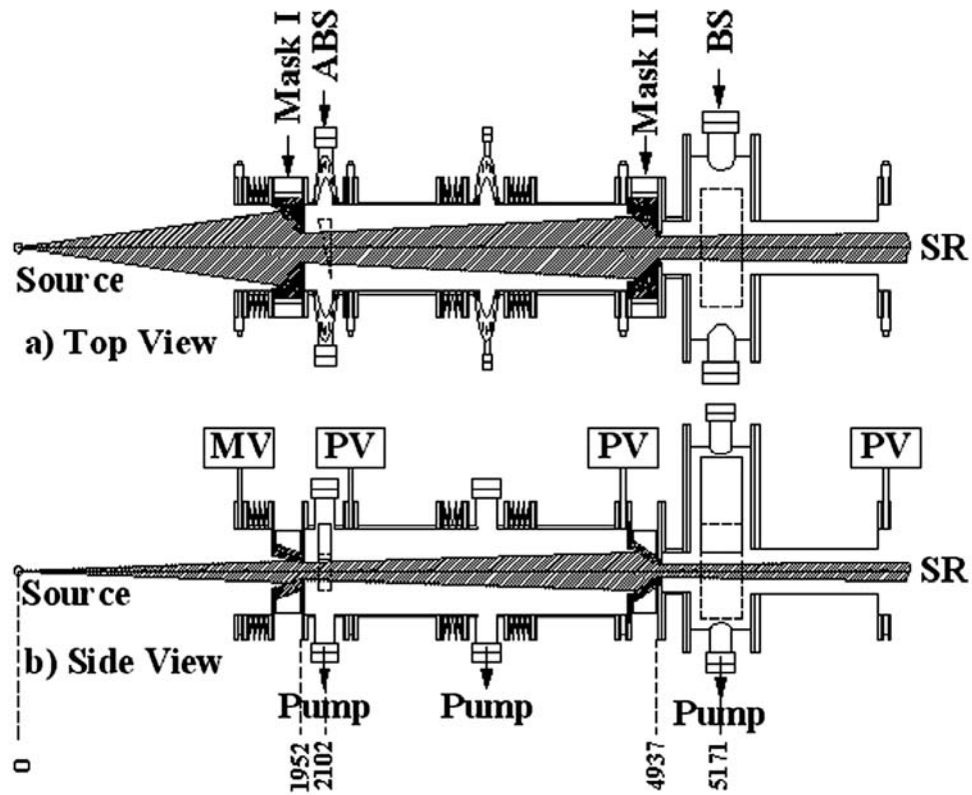


Figure 2.5 Top view (a) and side view (b) drawings of the front-end of the BL-4 beamline. The acceptance angle of synchrotron radiation of the beamline is defined by Mask II. The scale in the direction along SR is different from the scale in the direction perpendicular to synchrotron light. MV and PV stand for a manual valve and a pneumatic valve, respectively.

The components of the front-end are installed inside the radiation shield wall and along a line tangential to the designed electron orbit in the storage ring, as shown in Figure 2.6. The tangent point has been chosen to be 10° downstream from the entrance of the BM4 bending magnets. The vacuum system of the front-end consists of three main chambers connected together by two vacuum ducts. Each chamber is equipped with a sputter ion pump and a titanium sublimation pump. Ultra-high vacuum of 2×10^{-10} mbar or better in the front-end is obtained after well-baked at 150°C for a week. Two CF152 pneumatic gate valves are used to vacuum-isolate the three chambers. The vacuum condition of the front-end can also be isolated from the vacuum in the storage ring by a CF203 manual gate valve. The last valve is used only during the shutdown of the light source for maintenance.

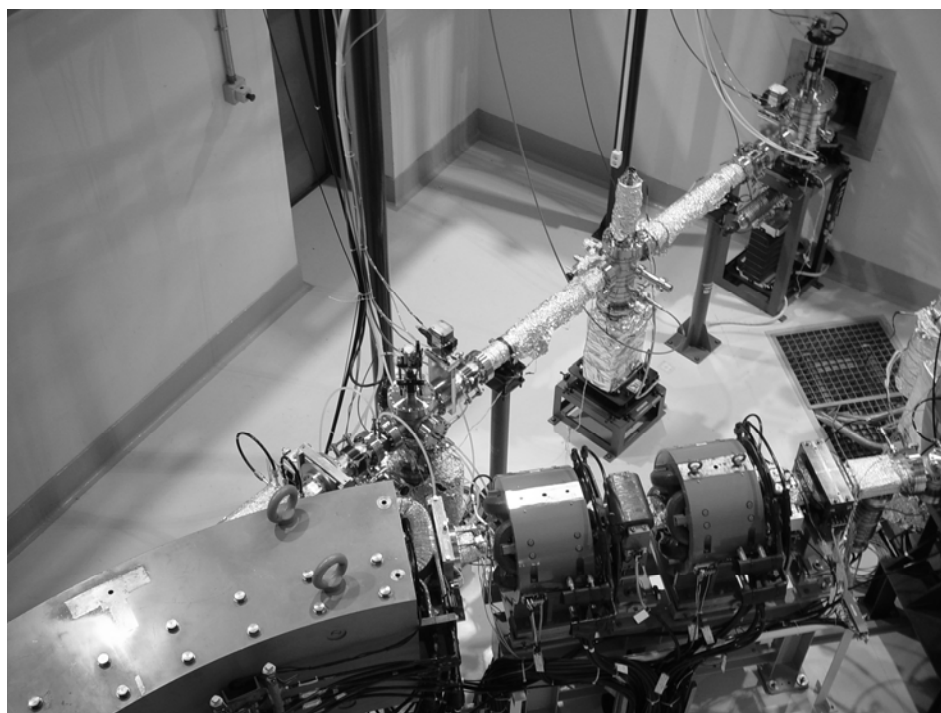


Figure 2.6 The photo of the front-end of the BL-4 beamline connected to the beam channel of the vacuum chamber of the BM4 bending magnet.

2.2.2 Optical Beamline

The BL-4 beamline has been designed and constructed for ARPES. Required performance of the BL-4 beamline are the maximum resolving power of 5000, the size of the light beam of less than 1mm in diameter and the photon flux of more than 10^9 photon/s. More importantly, as the BL-4 beamline is the first beamline at the Siam Photon Laboratory, the ease of operation had to be taken into consideration in the design.

Although the design of the BL-4 beamline is not a part of this thesis work, it is worth mentioning the optics design for this beamline because it is essential for understanding the results obtained from ray-tracing simulations and from the commissioning of the beamline. In the optics design, the resolving power of the monochromator, the size of the monochromatized light beam and the photon flux at the sample position have been considered to meet the requirements for ARPES experiments (Songsiriritthigul, Pairsuwan, Ishii, and Kakizaki, 2001). A VLSPG monochromator was chosen for its simple photon energy scanning mechanism. Toriodal mirrors were adopted as the pre- and post-focusing mirrors. A toriodal surface provides focusing power in two directions with a single mirror. Thus the number of mirror can be minimized, resulting in high transmission to satisfy the required photon flux at the sample.

The total length of the beamline is limited by the size of the available space in the experimental hall. The distance from the source position to the sample position of the BL-4 beamline is 23.4 m. The optical layout of the BL-4 beamline is illustrated in Figure 2.7. It consists of two Masks, a pre-focusing mirror (M0), a VLSPG monochomator and a post-focusing mirror (M2). The Masks are installed in

the front-end part. They are used for defining the size of the synchrotron-light beam and protecting the downstream components from thermal damage. Detailed information of the Masks has already given in Section 2.2.1.

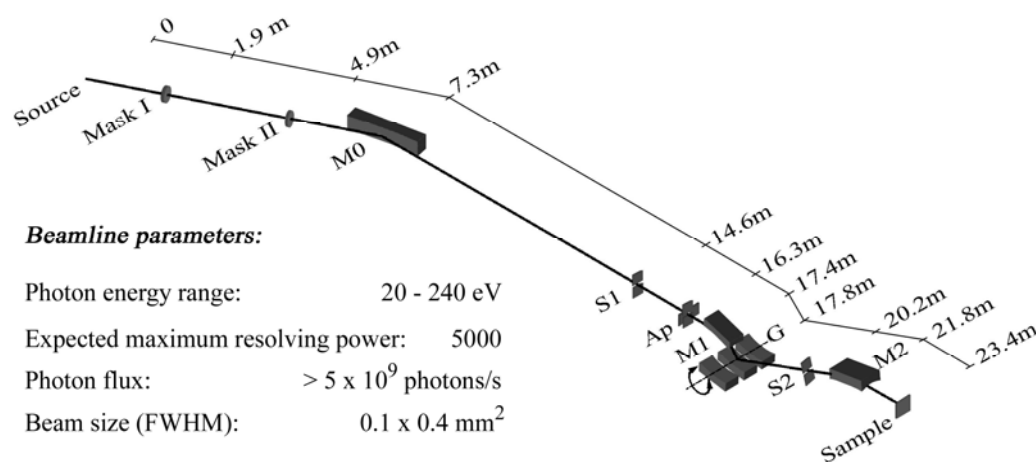


Figure 2.7 Optical layout and some parameters of the BL-4 beamline at the Siam Photon Laboratory.

2.2.2.1 Monochromator

The VLSPG monochromator employed in the BL-4 beamline operates in the constant included angle geometry with an included angle of 165° . The optical system of the VLSPG monochromator consists of the entrance slit (S1), a focusing spherical mirror (M1), three varied line-spacing plane gratings (VLSPGs) and the exit slit (S2). The entrance slit illuminated by light reflected from a toroidal mirror acts as a source for the monochromators. An X-Y aperture (Ap) inserted between the entrance slit and the focusing mirror is used to reduce coma and spherical aberrations to obtain high resolution. The demagnification of the focusing mirror in the dispersion plane equals one, i.e. the ratio of the entrance and exit arm-lengths of the focusing mirror is 1:1. The entrance and exit arm-lengths of the focusing mirror are 2800 mm. It is found that three gratings are necessary to cover a photon energy range of 20-240 eV. The gratings with a groove density at the center of the gratings of 300, 600 and 1200 lines/mm are used to cover photon energy ranges of 20-60 eV, 40-120 eV and 80-240 eV, respectively. All grating are holographically recorded ion-beam-etched laminar gratings manufactured by Carl Zeiss Laser Optics GmbH, Germany. The gratings are interchangeable by a linear translation mechanism and the photon energy scanning is made by grating rotation. The first positive order of diffraction (inside order) is considered to give the maximum dispersion.

Figure 2.8 illustrates a convergent synchrotron light beam incidents on VLSPG. The convergent beam is the reflected beam from the upstream focusing mirror M1. As illustrated in the figure, the angles of incidence, thus the angles of diffraction, at point 1 and point 2 are slightly different. This causes the broadening of the energy width of the light passing through the exit slit S2. To minimize the F_{100}

term (equation 1.55), the groove density of the grating must be varied along the ω direction, the direction which is perpendicular to the groove line. This is the principle of a VLSPG monochromator that the spacing variation is required to compensate the differences of the angles of incidence and diffraction at both ends of the grating. This type of monochromators requires a focusing mirror to produce a convergent incident beam for the grating. This focusing mirror is a critical optical element which has a significant influence on the performance of the monochromator. The alignment of this mirror is as important as the miss-shaped of the reflection surface. Most of VLSPG monochromator employs a spherical mirror as the focusing mirror (Underwood and Koch, 1997; Kiyokura, Maeda and Wanatabe, 1998; Kitajima et al., 1998; Underwood, 2000 and Ono et al., 2001). This is due to the easy to manufacture spherical surface with small figure errors. The monochromator of the BL-4 is also a spherical mirror as the focusing element.

The entrance slit of the VLSPG monochromator acts as the light source of the monochromator. Thus, the distance between the entrance slit and the spherical mirror is the entrance arm length of the spherical mirror, which is 2800 mm. To minimize the coma aberration, the radius of the spherical surface of the mirror is chosen in such a way that the ratio of the entrance and exit arm length of the mirror is 1:1, i.e. the demagnification of the mirror is 1.0. The detailed specifications of the spherical mirror is given in Table 2.6. The divergent light beam from the entrance slit incidents on the spherical mirror. The reflected light from the mirror is focused, thus the convergent beam is illuminated on the grating. The light source of the grating is a virtual one located the back side of the grating, as illustrated in Figure 2.8.

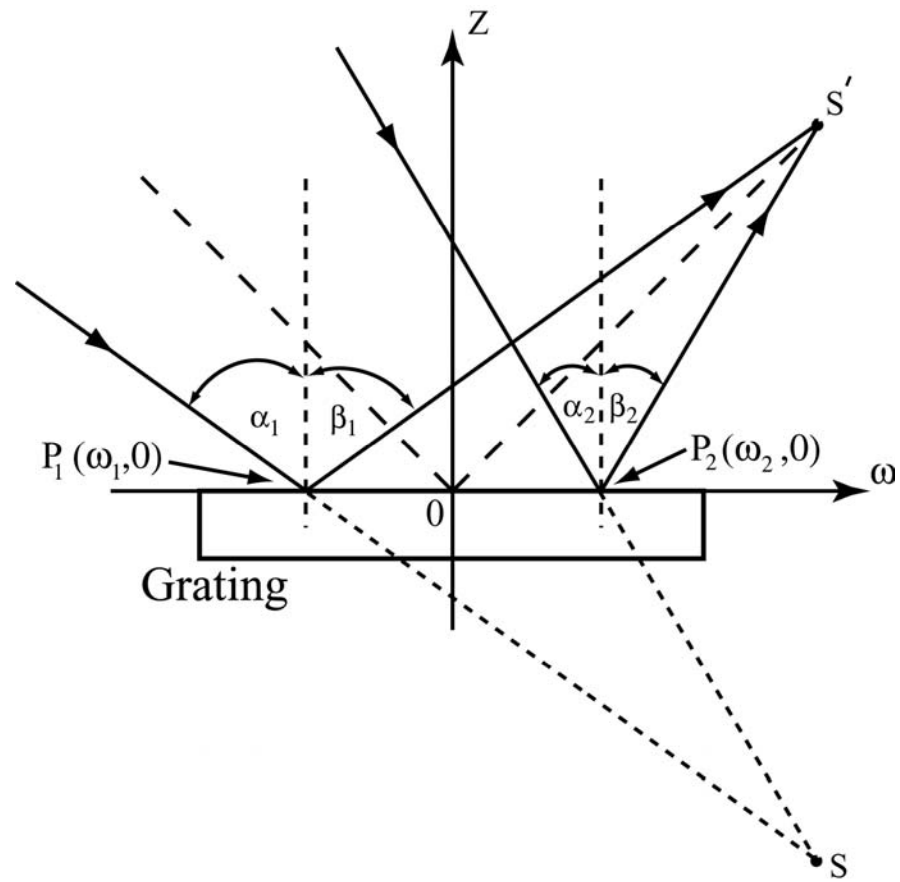


Figure 2.8 A convergent light beam incidents on VLSPG. It should be noted that the differences of angles of incidence and the angles of diffraction at point 1 and 2 are exacterated.

The coefficient a_1 , a_2 and a_3 and the exit arm length of the grating are determined by minimizing the major aberrations, i.e. the defocus, coma and spherical aberrations. In practice, VLSPG used in the monochromator covers a certain range of photon energy. To minimize the aberrations for the whole energy range, the aberrations are made vanised at appropriate values of photon energy (Hettrick, 1990). This is nowadays done by help of a computer. For the monochromator of the BL-4 beamline, the appropriate photon energies E_1 , E_2 , E_3 and E_4 were chosen to satisfy the condition $F_{20}(E_1) = F_{20}(E_2) = F_{30}(E_3) = F_{40}(E_4) = 0$. The values of E_1 , E_2 , E_3 and E_4 are given in Table 2.4. The exit arm-length, a_1 , a_2 and a_3 for all VLSPG's were found to be 2406.56 mm, $-8.219 \times 10^{-4} \text{ mm}^{-1}$, $5.023 \times 10^{-7} \text{ mm}^{-2}$ and $-2.702 \times 10^{-10} \text{ mm}^{-3}$, respectively (Songsiriritthigul et al., 2001).

Table 2.4 The optimum values of E_1 , E_2 , E_3 and E_4 used for determining the line-spacing variation coefficients, r_2 of varied line-spacing plane gratings (VLSPG's).

Grating No.	E_1 (eV)	E_2 (eV)	E_3 (eV)	E_4 (eV)
VLSPG 1	22	52.5	30	40
VLSPG 2	44	105	60	80
VLSPG 3	88	210	120	160

Table 2.5 Specifications of the VLSPG of the BL-4 beamline.

	VLSPG1 grating	VLSPG2 grating	VLSPG3 grating
Profile	Laminar holographic	Laminar holographic	Laminar holographic
Material	Silicon	Silicon	Silicon
Coating	Gold	Gold	Nickel
Grating area	135 x 22 mm ²	135 x 22 mm ²	135 x 22 mm ²
Line density at the center	300 lines/ mm	600 lines/ mm	1200 lines/ mm
Energy range	20 – 60 eV	40 – 120 eV	80 – 240 eV
Deviation angle	165°	165°	165°
Roughness	≤ 50 nm rms	≤ 50 nm rms	≤ 50 nm rms
Slope error (arcsec rms)	Tangential: ≤ 0.2 Sagittal: ≤ 0.5	Tangential: ≤ 0.2 Sagittal: ≤ 0.5	Tangential: ≤ 0.2 Sagittal: ≤ 0.5

Figure 2.9 shows the resolution, $\Delta\lambda/\lambda$ or $\Delta E/E$, of the VLSPG monochromator of the BL-4 beamline obtained from the analytical calculations using the equations described in Chapter I with the spacing variation parameters of the gratings mentioned above. In the calculations, the widths of the entrance and exit slits are varied with photon energy so that the contribution to the resolution caused by

the slit width is fixed at 2×10^{-4} . The widths of the entrance and exit slits for a fixed resolution of 2×10^{-4} are given in Figure 2.10. The figure slope error of the VLSPGs used in this beamline is 0.2 arcsec. It is obvious that, the figure slope error of the VLSPGs and the slit width are the main contributions to the resolution. The contribution of the figure slope error increases with increasing photon energy.

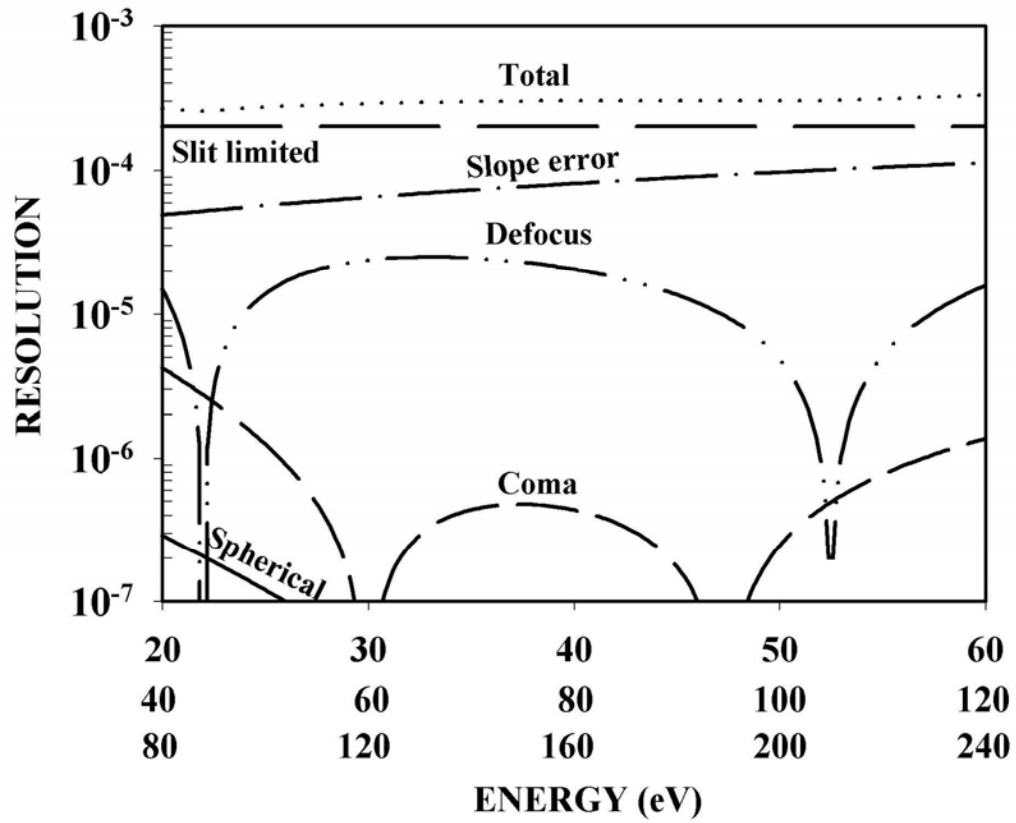


Figure 2.9 The calculated spherical, coma, defocus and slope error aberrations and the resolution limited by the width of the entrance and exit slit of the VLSPG monochromator.

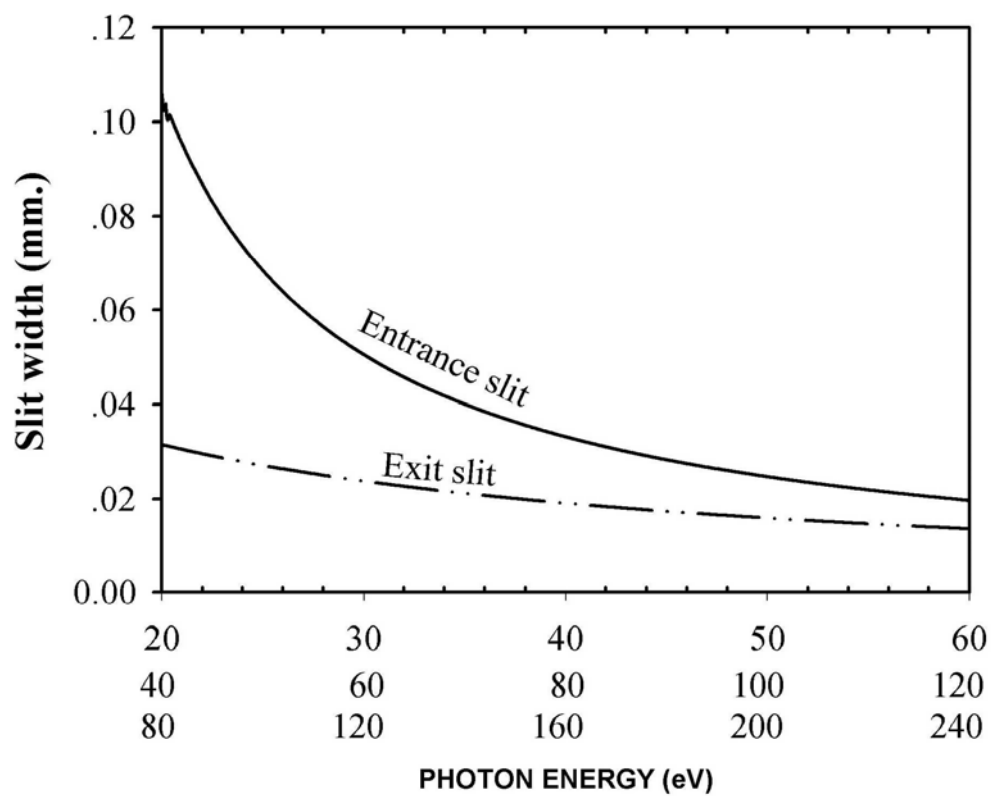


Figure 2.10 The widths of the entrance and exit slits to obtained a resolution limited by the slit width of 2×10^{-4} .

2.2.2.2 Pre- and Post Focusing Mirrors

The pre- and post-focusing mirrors are toriodal mirrors. This type of the mirror allows focusing power in two directions (saggittal and meridional foci) to be adjusted independently. Therefore, there is no need to use two mirrors to focus synchrotron-light beam in two directions. Both pre- and post-focusing mirrors are mode of silicon. The surfaces of the mirrors are coated with gold of approximately 50 nm to increase the reflectivity.

The angle of incidence for the pre- and post-focusing mirrors are 85° and 86.5° , respectively. Detailed specifications of the two mirrors are given in Table 2.6. The pre-focusing mirror is mounted on a water-cooled holder to prevent thermal damage to the mirror due to the heat load from synchrotron light.

The pre-focusing mirror was chosen to be located just outside the shield wall to allow the access for positioning the mirror while the light source is in operation. Due to a limited space available in the experimental hall, the pre-focusing mirror has to be located as near to the source position as possible. However, for the ease of handling thus the entrance arm-length of the pre-focusing mirror was fixed to be 7300 mm. To minimize the aberration, the magnification of the pre-focusing mirror was chosen to be 1.0, i.e. the ratio of the entrance and exit arm-length is 1:1. As the dispersion plane of the monochromator is in the vertical plane, the pre-focusing mirror is oriented to horizontally deflect and focus the synchrotron-light beam into the entrance slit of the monochromator. It should be noted that the plane of electron orbit is in the horizontal plane.

Table 2.6 Parameters of the pre-focusing, focusing and post-focusing mirrors.

Mirror	Surface shape	Roughness (nm rms)	Slope error (arcsec rms)	Specifications parameter
M0	Toroidal Si coated Au	Specified ≤ 0.5 Measured = 0.17-0.19	<u>Tangential</u> : Specified = 1 Measured = 0.8 <u>Sagittal</u> : Specified = 2 Measured = 1.8	$\rho = 636.2 \text{ mm } (\pm 5\%)$ $\rho_{\text{measured}} = 637.0 \text{ mm}$ $R = 94122 \text{ mm } (\pm 1\%)$ $R_{\text{measured}} = 94300 \text{ mm}$ Size = $550 \times 55 \times 40 \text{ mm}^2$ Active area = $520 \times 45 \text{ mm}^2$
M1	Spherical Si coated Au	Specified ≤ 0.5 Measured = 0.12-0.13	<u>Tangential</u> : Specified = 0.2 Measured = 0.19 <u>Sagittal</u> : Specified = 0.5 Measured = 0.38	$R = 40140 \text{ mm } (\pm 1\%)$ $R_{\text{measured}} = 39880 \text{ mm}$ Size = $140 \times 50 \times 40 \text{ mm}^2$ Active area = $120 \times 40 \text{ mm}^2$
M2	Toroidal Si coated Au	Specified ≤ 0.5 Measured = 0.13-0.34	<u>Tangential</u> : Specified = 1 Measured = 1 <u>Sagittal</u> : Specified = 5 Measured = 2.4	$\rho = 148.8 \text{ mm } (\pm 5\%)$ $\rho_{\text{measured}} = 148.7 \text{ mm}$ $R = 26220 \text{ mm } (\pm 1\%)$ $R_{\text{measured}} = 26181 \text{ mm}$ Size = $140 \times 55 \times 40 \text{ mm}^2$ Active area = $120 \times 40 \text{ mm}^2$

Figure 2.11 shows schematic diagram of the focusing optical element in the BL-4 beamline both in the vertical and horizontal planes. The figure shows the entrance and exit arm-lengths of all mirrors from which the total magnification of the beamline can easily be calculated. The size of the beam on the sample can easily be calculated from the magnification of all mirrors in the beamline. The magnification of each mirror is the ratio of the exit arm-length to entrance arm-length of the mirror. The total demagnification is the multiplication of the demagnifications of all mirrors in the beamline. In the vertical direction, the ratio of the entrance and exit arm-length of all mirrors is 1:1. The arm-length of the pre-focusing, focusing and post-focusing mirrors are 7300 mm, 2800 mm and 1600 mm, respectively. Thus the demagnification of the optical system in the vertical direction equals 1. The vertical beam size at the sample position is the same as that of the source when optical aberrations are not taken into consideration. In the horizontal direction, the entrance arm lengths the pre-focusing, focusing and post-focusing mirrors are 7300 mm, 739.33 mm and 5139.78 mm and the exit arm lengths are 9361.67 mm, -739.78 mm and 1600 mm for the pre-focusing, focusing and post focusing mirrors, respectively. Thus the demagnification of the optical beamline in the horizontal direction equals 2.5. The horizontal beam size at the sample position will be, in principle, 2.5 times smaller than that of the source. The demagnification in vertical and horizontal direction gives a rough estimated size of light beam at the position of the sample in the experimental station.

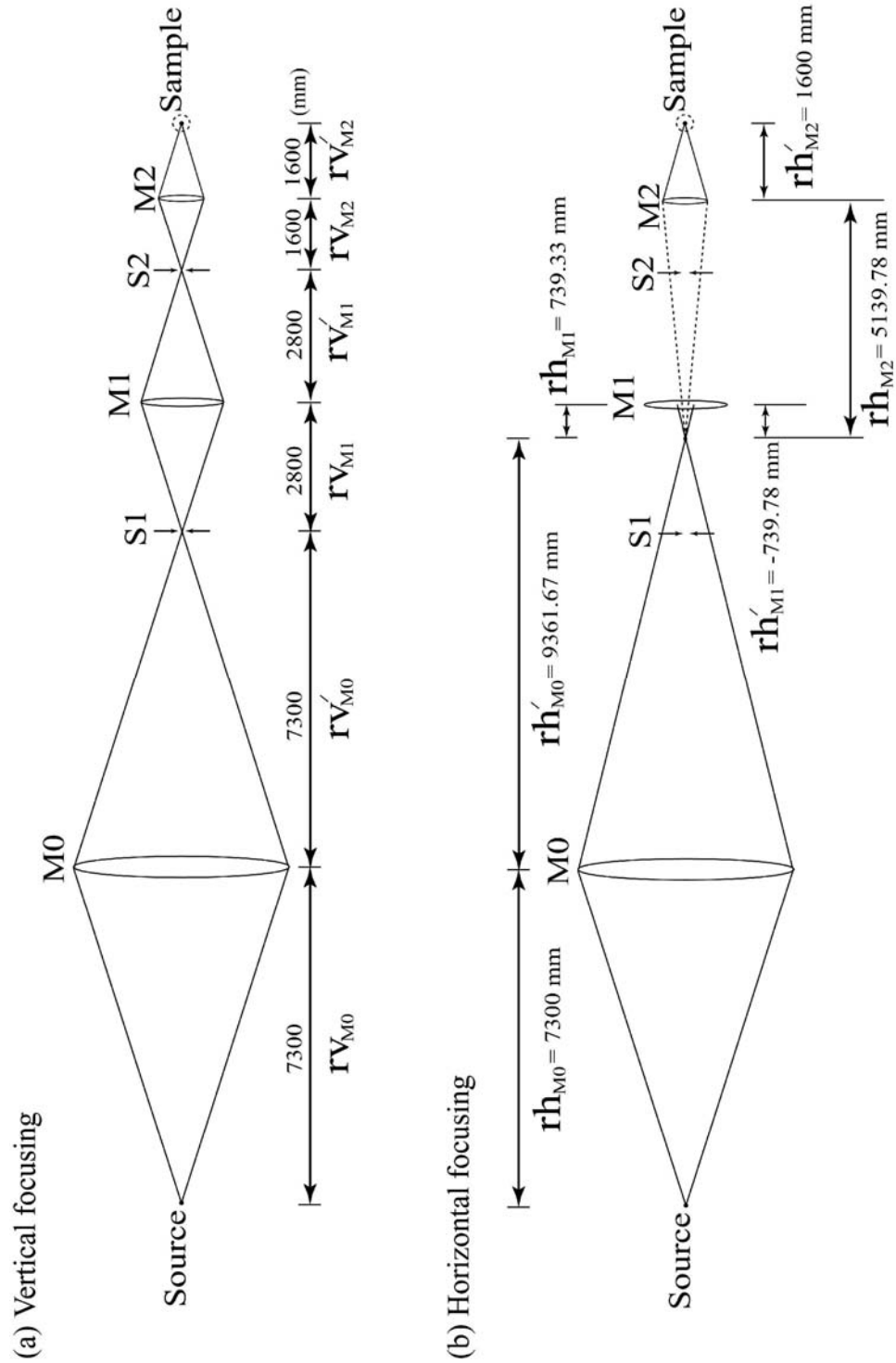


Figure 2.11 The schematic diagram of the focusing optical element in the BL-4 beamline (a) in the vertical plane and (b) in the horizontal plane.

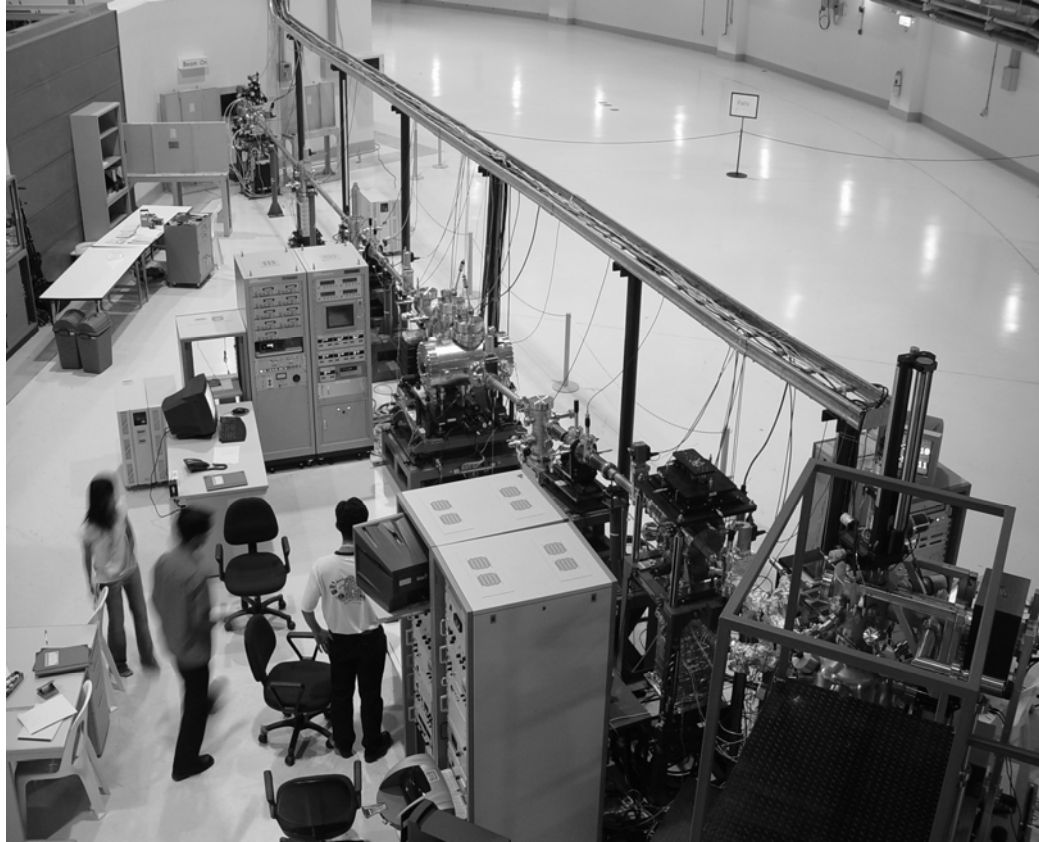


Figure 2.12 Photo of the BL-4 beamline at the Siam Photon Laboratory.

2.2.2.3 Photon Energy Scanning Mechanism

This part is the background for the data acquisition and control system for BL-4 beamline that I have developed. Scanning of photon energy of this monochromator of the BL-4 beamline is simply done by a rotation of the gratings. The rotation of the gratings is performed by a sine-bar driven by a DC stepping motor under the control of the home-developed software written using the LabView program. Thus, in this configuration of photon energy scanning, only a linear movement driven by a step motor is required. A linear encoder is employed to assure the reproducibility of the linear movement of the scanning mechanism. For accurate

linear motion, the high precision ND281B Heidenhain linear encoder scale is used. The resolution of the encoder is $0.01\text{ }\mu\text{m}$. The three gratings are installed on a rotation table. Exchange of the gratings is done by a linear movement by a manual linear drive. The external of the grating chamber is shown in Figure 2.13.

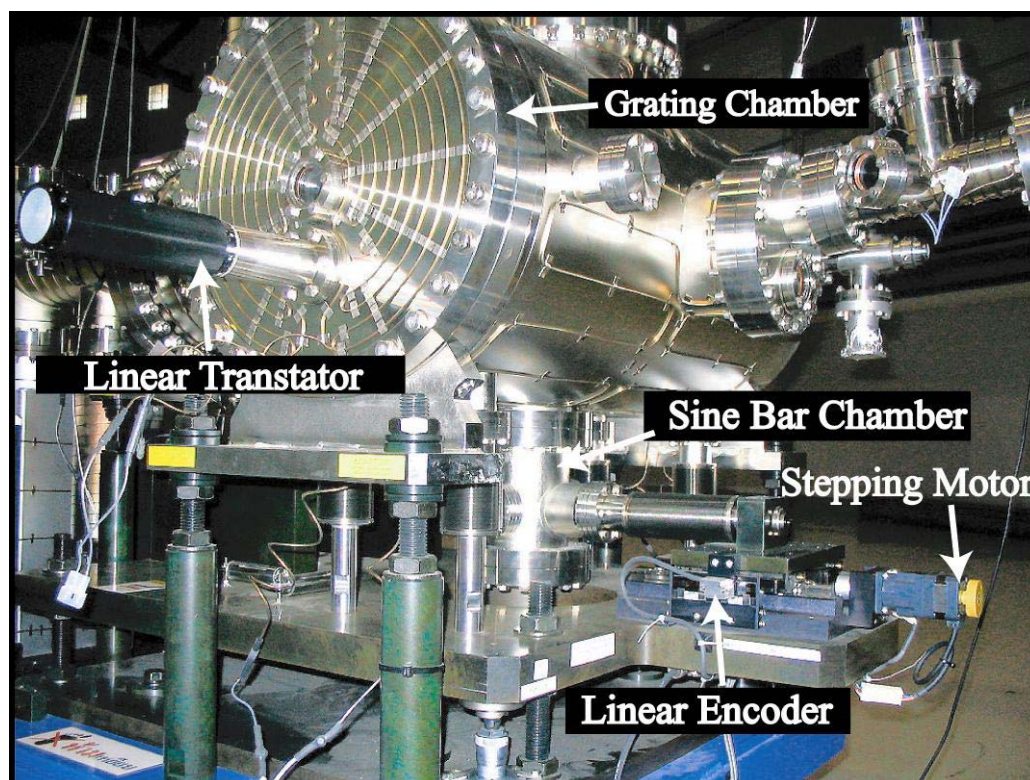


Figure 2.13 The photo of the grating chamber. The step motor for driving the sine bar and the linear encoder are installed outside the grating chamber. The sine bar located inside the UHV chamber is connected to the step motor via the bellows. The linear translator located on the left flange is used for exchanging the gratings.

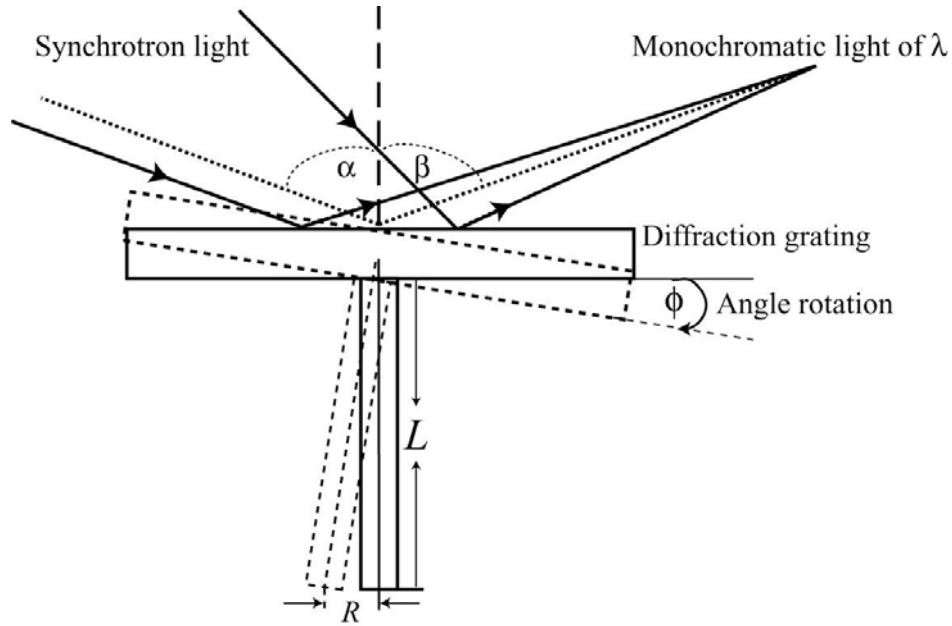


Figure 2.14 The sine bar for the rotation of the grating in monochromators with a constant included angle.

For a constant included angle monochromator, the grating equation can be written as

$$Nk\lambda = 2 \cos \theta \sin \phi \quad (2.1)$$

where $2\theta = \alpha - \beta$ is the included angle (which is 165° for the monochromator of the BL-4 beamline), ϕ is the rotating angle with respect to the normal of the surface plane of the grating when zero-order light passing through the entrance and exit slits, which is obtained from the relation $2\phi = \alpha + \beta$. For the zero-order light, θ is the angles of incidence and reflection, which is 82.5° . It is obvious that the wavelength of the diffraction beam is merely a function of the rotating angle of the grating. The rotation

of the grating is performed by a linear motion drive as shown in Figure 2.14. The relationship between the linear displacement (R) and the rotating angle is given as

$$R = L \sin \phi \quad (2.2)$$

where L is the length of the sine bar. Substitution Equation (2.2) into Equation (2.1), the relationship between the linear motion and the rotating angle can be easily found as follow.

$$\lambda = \left(\frac{2 \cos \theta}{NkL} \right) \cdot R \quad (2.3)$$

The relationship between the wavelength and photon energy is given as

$$\lambda(nm) = \frac{1239.85}{E(eV)} \quad (2.4)$$

2.2.3 End Station

The end station of the BL-4 is for ARPES experiments. The experimental station was designed for the investigations of electronic structures of solids and solid surfaces. The system consists of three main chambers, i.e. an analysis chamber, a sample preparation chamber and a load-lock (or fast-entry-air-lock, FEAL) chamber.

The FEAL chamber is used to prevent breaking of UHV condition in the analysis chamber during introducing the sample to the sample holder. The load-lock chamber is evacuated by a turbo-molecular pump backed by a two-stage rotary pump. The ultimate vacuum pressure in the FEAL chamber is $\sim 1 \times 10^{-7}$ mbar. A magnetic coupling linear transfer device is used for transferring the sample from FEAL to the analysis chamber. A grip is used to take the sample from the linear transfer device and insert into the sample holder on the manipulator in the analysis chamber.

The sample preparation chamber is mounted on top of the analysis chamber, as shown in Figure 2.15. A UHV gate valve inserted between the preparation chamber and the analysis chamber can separate the the vacuum condition of each chamber. The sample manipulator is mounted on top of the preparation chamber. With a long linear translation of the manipulator, the sample can be transferred between the preparation chamber and the analysis chamber. The sample preparation chamber is equipped with a 3 kV ion gun and a mini electron-beam evaporator. The sample can be cleaned in the preparation chamber by electron-beam heating or by ion sputtering. A thin metal film can also be grown on the sample by electron-beam evaporation. After a well baking cycle, the base pressure of the preparation chamber of 2×10^{-10} mbar is obtained by using a 300 l/s sputter ion pump combined with a titanium sublimation pump.

The analysis chamber is made of mu-metal to prevent the disturbance of the electron trajectory from external magnetic field such as the earth magnetic field. The chamber is pumped by a 500 l/s sputter ion pump combined with a titanium sublimation pump. The base pressure is 2×10^{-10} mbar or better. The main instruments in the analysis chamber are a LEED system, a Thermal VG Scientific (TVGS) ARUP10 energy analyzer, a TVGS CLAM2 energy analyzer, a twin-anode X-ray source, a UV discharged lamp and a 5 kV electron gun. The LEED system is used for checking the surface crystal structure of the sample. The combination of the energy analyzers and the excitation sources allows different surface-sensitive measurement techniques such as UPS, XPS and AES to be carried out in the analysis chamber. In addition, photoemission experiments using synchrotron light can also be performed.

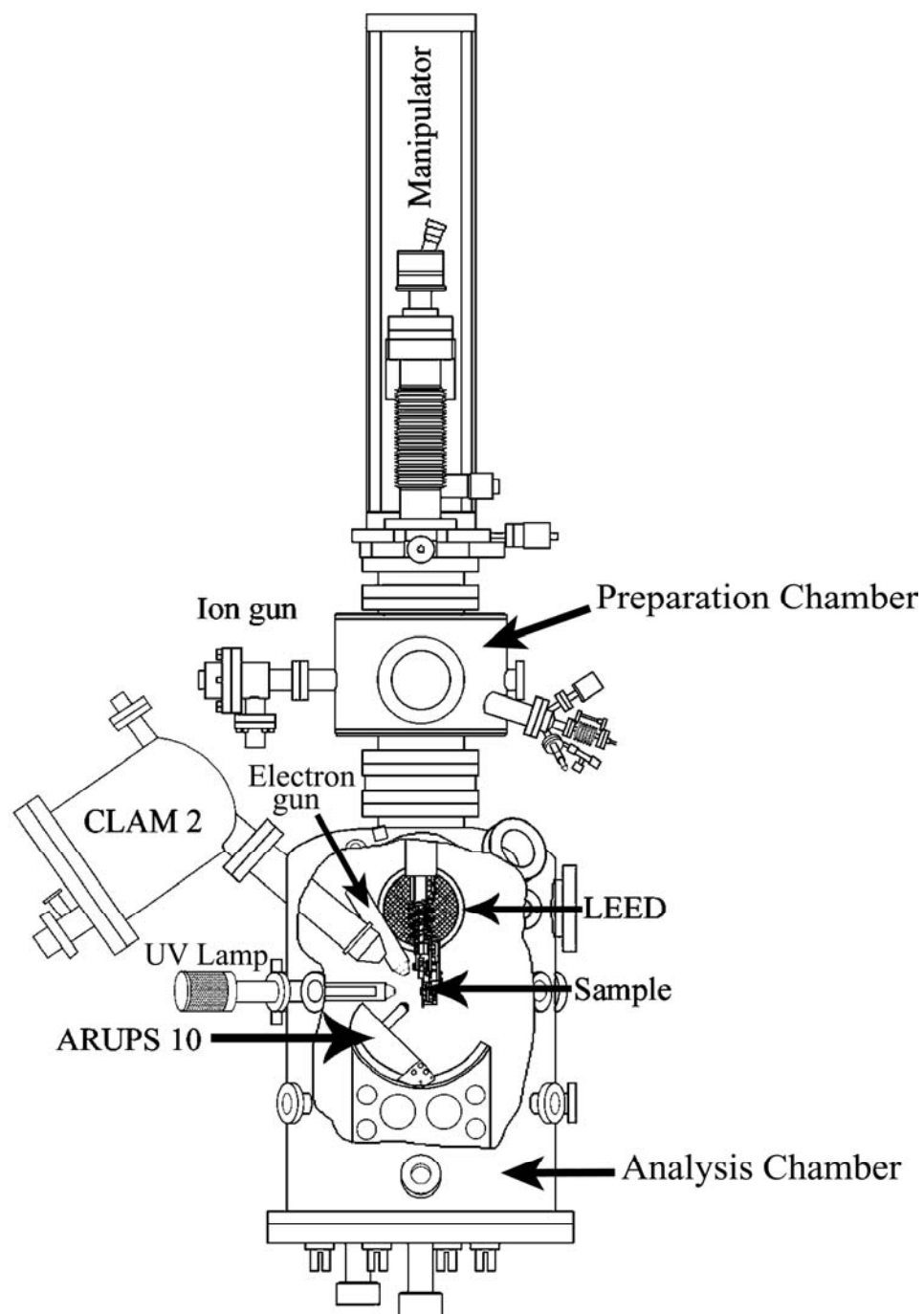


Figure 2.15 The schematic diagram of the experimental station of the BL-4 beamline shows the major instruments.

2.2.4 Vacuum System

Light in the VUV and soft X-ray regions is strongly absorbed by gas molecules in air, thus the optical path of the light must be evacuated. Good vacuum condition also minimizes the contamination on the surface of the optical elements that will reduce their transmission. VUV and soft X-ray beamlines are normally operated at the base pressure of $\sim 10^{-10}$ mbar, which is in the UHV range. The schematic diagrams of the vacuum systems of the front-end and optical beamline of the BL-4 beamline are shown in Figure 2.16. The vacuum system of the beamline has been designed and constructed for UHV for the whole length of the beamline. This allows an easy interface to the storage ring, since the pressure in the storage ring is also in the range of 10^{-10} mbar. The end-station of the BL-4 is also an UHV system, which is a necessary condition for photoemission experiments. The vacuum ducts and chambers are made of stainless steel. All seals use copper gaskets. The vacuum of the front-end and the optical beamline is divided into three and six sections, respectively. They are vacuum isolated by vacuum gate valves. This configuration provides the easy operation and maintenance. The vacuum system of the end-station is also vacuum-isolated by a vacuum gate valve and a sight-through valve. The use of the two valves allows the disconnection of the end-station from the optical beamline without breaking the vacuum condition of the optical beamline and of the end station.

Some mechanical components in the beamline such as scanning mechanics for grating and mechanical parts of the manipulators of mirror are made of aluminum. The magnitudes of the pressure in the whole beamline are in the range of 10^{-10} mbar. To obtain such good vacuum condition, long degassing procedures have been carried out. After the vacuum components were installed and before the optical

elements were placed in the chambers, the mechanical parts of the whole beamline have been baked at 200°C for 72 hours. It is noted that some heat-sensitive components were baked at lower temperatures. After the gratings and the mirrors were installed, only the sections where the optical elements are located have been baked further at 120°C for 25 days. Sputter ion pumps are used in combination of titanium sublimation pumps to produce ultra-high vacuum condition. Cold cathode gauges and hot filament gauges (NIG) are used for measuring the vacuum pressure in the beamline. The residual gases in the system have been analyzed by quadrupole mass spectrometers. The major residual gases after baking are H₂, CO, CO₂, CH₄ and Ar.

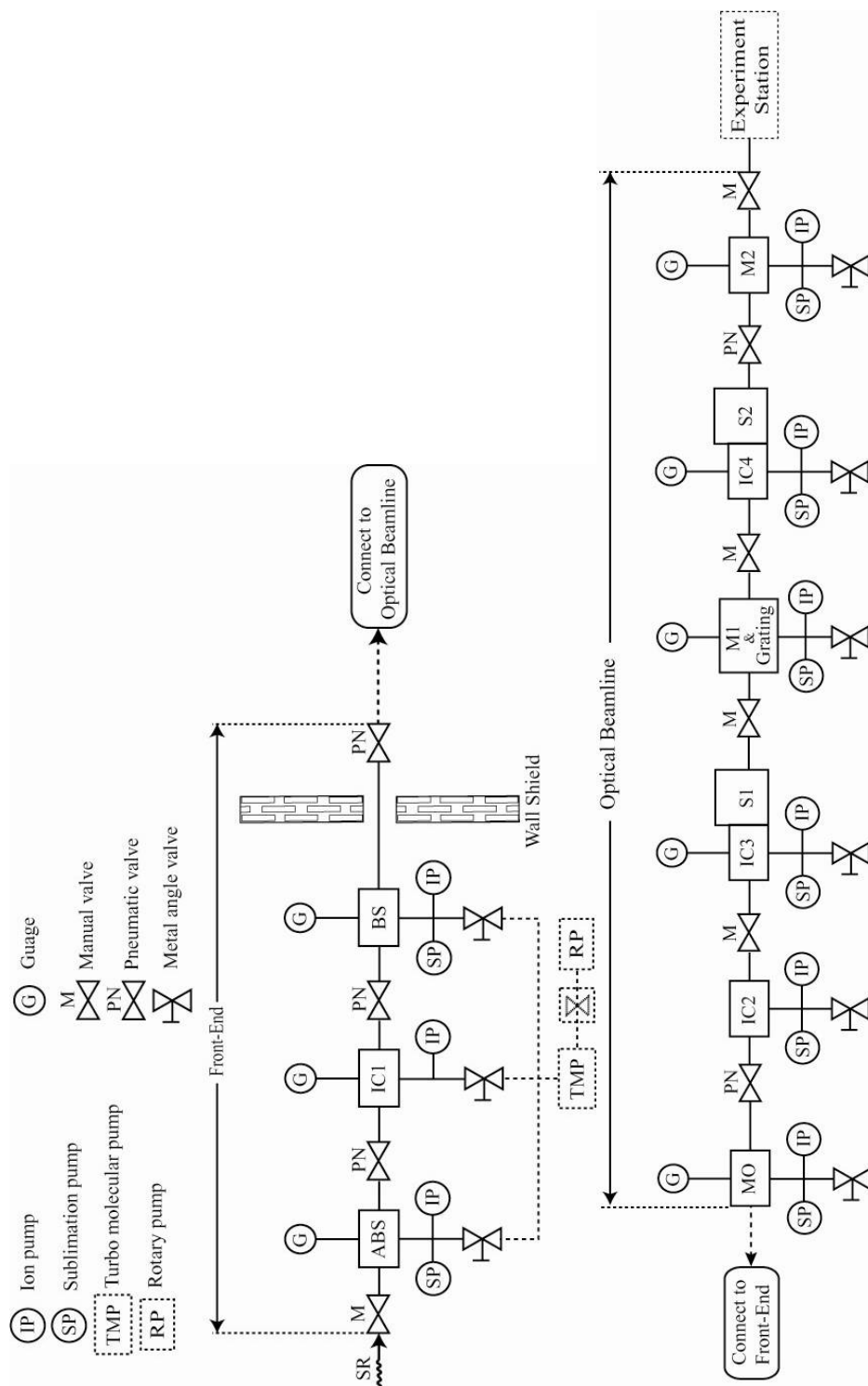


Figure 2.16 The schematic diagram of the vacuum systems of the front-end and optical beamline.

2.2.5 Interlock System

The basic concept of the interlock system of the BL-4 beamline is illustrated in the diagram shown in Figure 2.17. It consists of two sub-systems, i.e. the vacuum and beam interlock sub-system. The vacuum interlock sub-system is designed to protect the storage ring vacuum from an accidental break in the vacuum system of the beamline or end-station. The beam interlock sub-system is necessary for radiation safety and prevention of thermal damage of the downstream components.

The hardware of the interlock system comprises of an OMRON CS1 series programmable logic controller with input and output units and interface units. The status of the ion pumps (IPs), the storage ring, status of utilities, the vacuum pressure and the manual and pneumatic valves (MV, PVs), ABS and BS are displayed on a touch screen. The touch screen is also used as a man-machine interface to control the actions of ABS, BS and PVs.

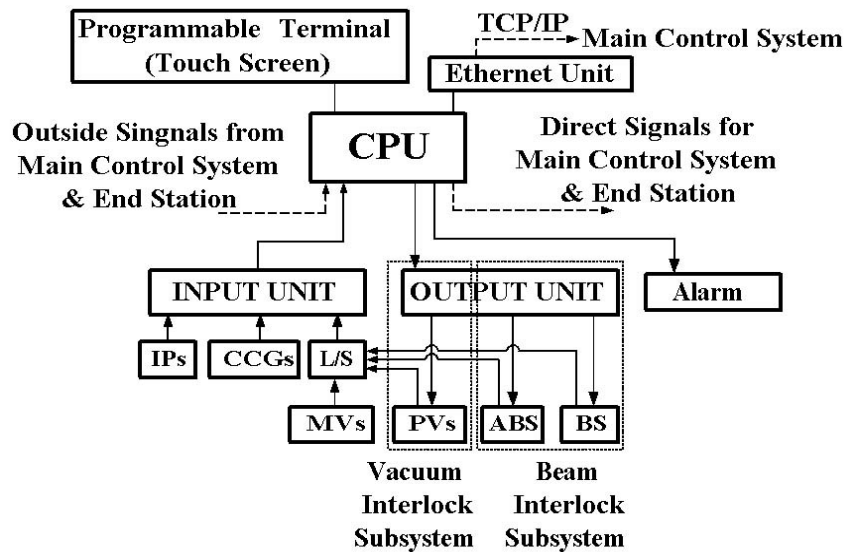


Figure 2.17 Schematic diagram of the interlock system for the BL-4 beamline at the Siam Photon Laboratory.

2.3 Ray Tracing

Optical path function analysis enables optics design for synchrotron light beamline to be conceived and analyzed in a way that allows their shortcomings to be understood. The ultimate test of any optics design is accomplished by ray tracing. The basic idea of ray tracing is simple, i.e. optical paths, or rays, are traced through a system of optical elements, the law of geometrical optics being observed at all time. There are only three optical principles required for the basic of ray tracing in the VUV and soft X-ray region as the following:

- The optical path between physical elements of the optical system is a straight line,
- The angle of reflection equals the angle of incidence and
- Diffraction phenomena is governed by Bragg's law.

Effective ray tracing is performed by using computers, where a number of rays (up to million rays) can be simulated. Many computer ray tracing simulation programs have been developed in the past. There are two well established programs, i.e. RAY (Schäfers, 1996) and SHADOW (Lai and Cerrina, 1986). The simulation software used in this thesis work is RAY, which has been developed at BESSY, Germany (Schäfers, 1996). The ray-tracing program RAY simulates the imaging and focusing properties of an optical system such as a synchrotron light beamline. It randomly creates a set of rays for various types of light source and traces them through one or more optical elements onto image planes. The geometric distribution of the rays at the source, all optical elements and the image planes can be visualized. One advantage of a ray tracing program is that it reveals the way the aberrations of one optical element

combine with those of another. Thus, it can be used to check compensation of the aberration of a combined optical elements system.

The RAY simulation program has been used in this thesis work. The software is for Alpha computers running under OpenVMS operating system. Figure 2.18 shows the coordinate system and angle used in the RAY simulation program for vertical and horizontal deviation mounts. The optical element is in the x-z plane, the optical path is always in the x-y plane.

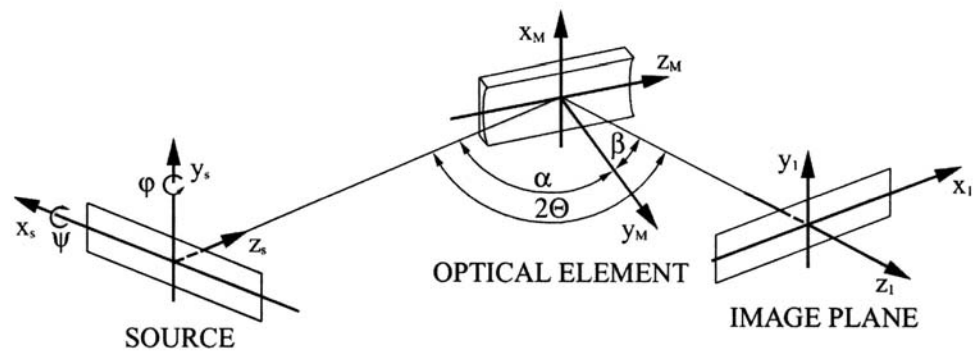


Figure 2.18 The coordinate system used in ray-tracing simulations (Schäfers, 1996).

2.4 Photoemission Technique

Photoemission spectroscopy (PES) is an indispensable technique, and perhaps the only one that allows direct observation of occupied electronic states in materials. When excitation light with sufficient photon energy, from a discharge UV lamp or a synchrotron light source, is incident upon a solid surface, photoelectrons are emitted. PES involves measurements of the kinetic energy distributions of photoelectrons. The spectrum of photoelectron intensity versus kinetic energy, called the energy distribution curve (EDC), is expected to present the electron density of states in the ground state. If a monochromatic light source is employed, then the kinetic energy distribution reflects the filled density of states (DOS) of the material. The DOS contains information related to the electronic structure and chemical composition of the near-surface region and to the bonding of adsorbates. Because the mean free path for electrons traveling in solids is fairly short, of the order of atomic dimensions, a PES spectrum reflects the DOS of the outermost few atomic layers of the solid. The escape depth can be approximated by the mean free path for a photoelectron. As a result, the escape depth of a primary photoelectron is very short. The escape depth is dependent on the kinetic energy of the photoelectron in the solid. This means that the photoemission process is quite surface sensitive. Thus, photoemission spectroscopy has become the most effective method for investigating the electronic structures of the surface and interfaces.

In photoemission process, a photon is absorbed by direct excitation of a bound electron to a final state above the vacuum level, E_{vac} . If a certain photon energy, $\hbar\omega$, is absorbed, an electron from a bound atomic core level is subsequently excited.

If the electron is excited above E_{vac} , it is emitted from the surface and it can be measured by an electron spectrometer. This process is illustrated in Figure 2.19.

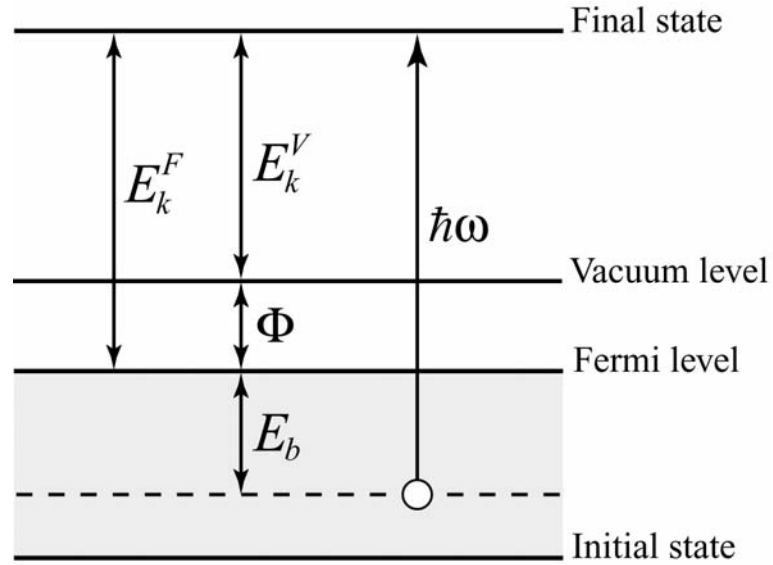


Figure 2.19 Schematic illustration of the energy diagrams of a photoelectron.

The binding energy, E_b , is the minimum energy required to remove an electron from a bound state. In other words, E_b is the energy needed to excite the electron to the first empty state of the solid, which is just above the Fermi level. In order to escape into vacuum, the electron also needs sufficient energy to overcome the surface work function, Φ . Thus, the conservation of energy implies that

$$\hbar\omega = E_b + E_k^V + \Phi \quad (2.5)$$

The outcome of the photoelectric effect is to translate the filled DOS, represented by the valence band and core level, to energies above the vacuum level.

2.4.1 Energy Analyzer

An electron energy analyzer is an essential instrument for an electron spectrometer used in the measurements of electron energy spectra. An electrostatic energy analyzer has from the beginning been adopted for measuring electron energy spectra in surface analysis techniques. This is due to the ease of construction and easy to handle in an UHV environment, comparing to analyzers employing magnetic field. Among different configurations of electrostatic analyzers, a concentric hemispherical analyzer (CHA) has been proven to be the most suitable for measuring photoelectrons. The best energy resolution of such an analyzer has been improved to the range of a few meV (Kevan, 1983). The CLAM2 energy analyzer used in this work is also an electrostatic CHA.

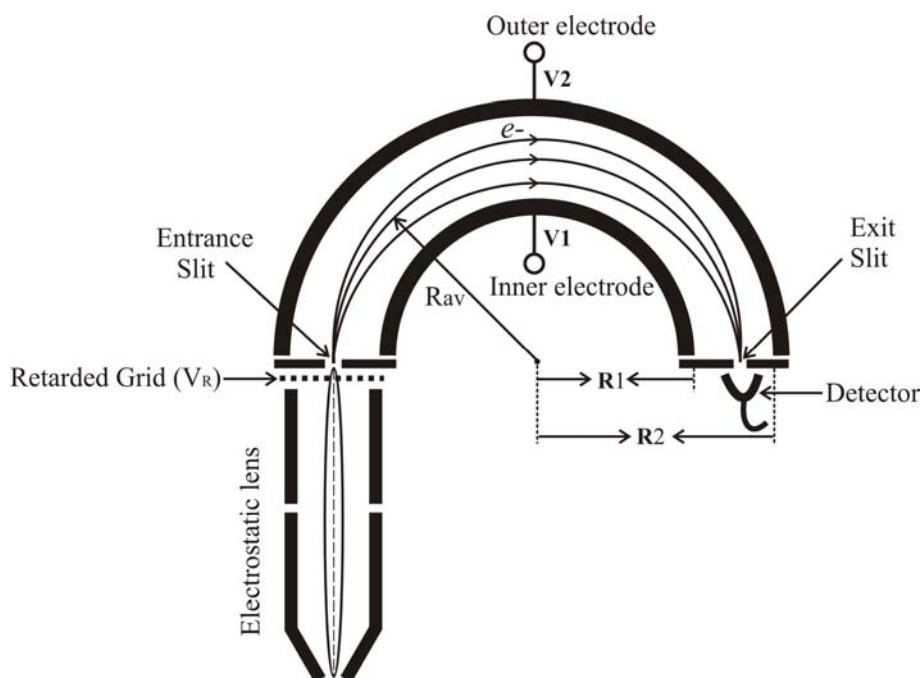


Figure 2.20 A feature cross section of a concentric hemispherical energy analyzer.

Figure 2.20 shows diagrammatically the cross-section of a conventional CHA and the energy diagram when a conducting sample contacts with the CHA. The CHA consists of an electrostatic lens, a hemispherical deflector with entrance and exit slits, and an electron detector, which may be a channeltron or a microchannelplate electron detector. The hemispherical deflector of the analyzer consists of two concentric hemispherical electrodes with the inner and outer hemisphere of radii R_1 and R_2 , respectively. The inner and outer hemispheres are applied with potentials V_1 and V_2 , with V_1 greater than V_2 . For the CLAM2 analyzer, the potentials applied to the inner and outer spherical sectors are the same magnitude but with different polarity. The potential of the outer spherical sector is negative with respect to the inner one, i.e. $V_2 = -V_1$.

The potential $V(r)$ along the equipotential surface between the two hemispheres with radius r can be obtained by solving the Laplace's equation in spherical coordinates (Kenneth, 1998). The potential $V(r)$ is given in equation (2.6).

$$V(r) = V(R_{av}) + 2k_R \left(\frac{R_{av}}{r} - 1 \right) \Delta V \quad (2.6)$$

where R_{av} is the median radius (R_{av} is 100 mm for CLAM2), k_R is the analyzer

constant ($k_R = \frac{R_1 R_2}{R_2^2 - R_1^2}$), ΔV is the potential difference between the inner and outer

hemispheres, and $V(R_{av})$ is the potential along the median surface, which is given by

$$V(R_{av}) = k_R \Delta V \quad (2.7)$$

If photoelectrons with the kinetic energy $E_p = eV(R_{av})$ enter the analyzer at the center of entrance slit within a small cone around the normal angle,

they will travel along the median equipotential surface and pass through the exit slit. Such the kinetic energy E_p is called the pass energy. Electrons with kinetic energy higher than E_p are deflected to hit the outer spherical sector while those with kinetic energy lower than E_p hit the inner spherical sector. E_p may be rewritten as given in equation (2.8).

$$E_p = ek_R \Delta V \quad (2.8)$$

For a given analyzer, the pass energy of the analyzer is a function of the potential difference between the inner and the outer hemispheres.

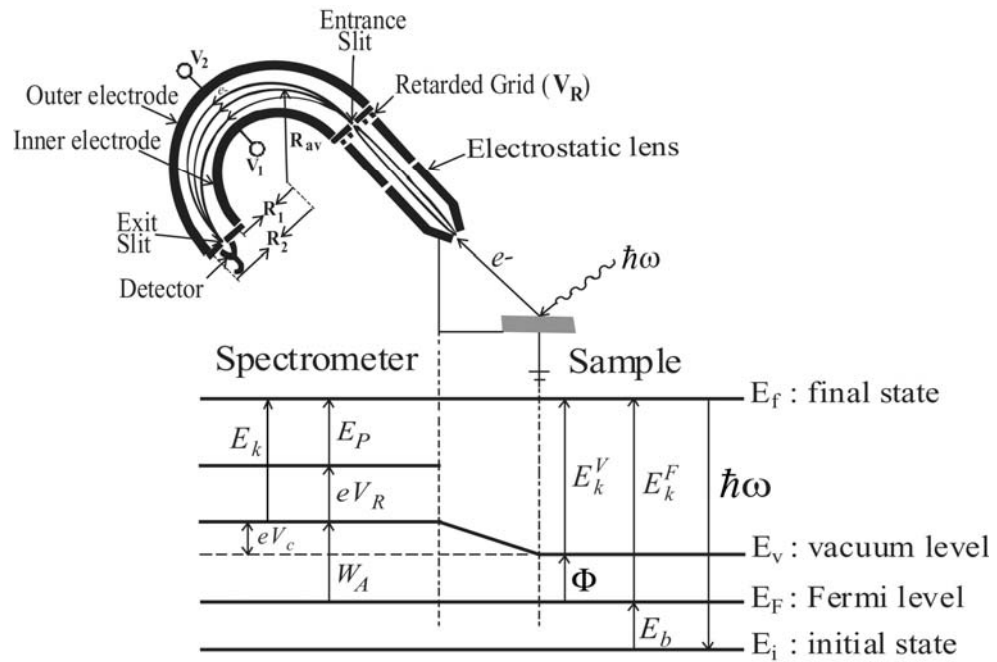


Figure 2.21 The schematically diagram of energy level contacting between metallic sample and spectrometer of PES measurement.

The photoelectrons emitted from the conducting sample, illustrated in Figure 2.21, are focused in to the entrance slit of the analyzer. Before entering the entrance slit the photoelectrons are decelerated or accelerated by the potential of V_R . The photoelectrons with appropriate kinetic energy according to equation (2.9) will travel passing through the exit slit. The numbers of the photoelectrons are then counted by the detector located at the exit slit.

$$E_k^F = eV_R + E_P + W_A \quad (2.9)$$

where W_A is the work function of the analyzer. Generally, energy analyzers can be operated in two energy analyzing modes, i.e. a constant analyzer energy (CAE) mode and a constant retard ratio (CRR) mode. The CAE mode is normally used for photoelectrons measurements such as UPS, XPS, and synchrotron light photoemission. In this mode, the energy spectra are obtained by varying V_R while the pass energy is fixed. To obtain spectra in CRR mode, E_p is varied with V_R in such a way that the ratio between V_R and E_p is kept constant. The CRR mode is normally used for AES measurements.

In some applications, the binding energy, E_b , is referred. The relation between the binding energy and the kinetic energy measured, E_k , is given as

$$E_b = \hbar\omega - E_k - W_A \quad (2.10)$$

2.4.2 The CLAM2 Spectrometer

The CLAM2 spectrometer system diagram is shown in Figure 2.22, consists of the Thermo VG Scientific (TVGS) CLAM2 energy analyzer and control electronics units such as the TVGS 362 spectrometer controller unit (SCU362), TVGS 8508 Lens Power Supply, TVGS 434 Rate Meter and TVGS 8006 Digital Meter. The system delivered to NSRC with a data acquisition software VGX900, allowing the data acquisition to be done by using a personal computer.

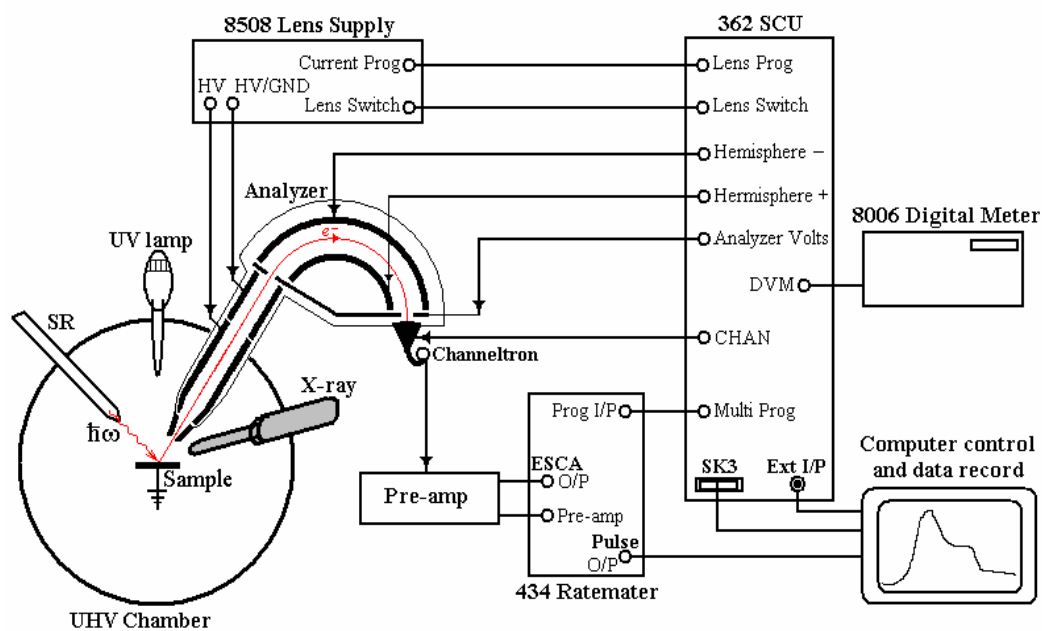


Figure 2.22 The schematic diagram of the CLAM2 spectrometer system.

The CLAM2 analyzer is an electrostatic concentric 150° spherical sector analyzer with mean radius of 100 mm. The major components of the CLAM2 analyzer are an electrostatic lens, apertures, an electron energy analyzer and a single channel electron multiplier (channeltron). All of these components of the CLAM2 spectrometer are shielded and contained within an UHV chamber, which is constructed of a low magnetic permeability material such as mu-metal to avoid the disturbance of the trajectory of electrons from external magnetic

The CLAM2 spectrometer can be operated in two different energy analysis modes, i.e. CAE (constant analyzer energy) and CRR (constant retard ratio) modes of measurement.

In the CAE mode operation of the CLAM2, the pass energy is fixed value selected by a constant and the retarding voltage on the input lens ramp with the kinetic energy. Consequently, the range of electron passable energies (i.e. the energy resolution ΔE) is a constant. The energy resolution (Damascelli, 2002, and Stevens, Donoho, Turner, and Erskine, 1983) is given as

$$\Delta E = E_P \left(\frac{d}{2R_{av}} + \frac{\alpha^2}{4} \right) \quad (2.11)$$

The energy resolution ΔE would be the full width at half maximum (FWHM) of a recorded peak. Where d is slit width and α is the acceptance angle of electrons beam. The CLAM2 is designed that the width of the exit slit equal to the width of entrance slit. The CAE mode is used for UPS and XPS, with selectable values are 0.1, 0.25, 0.5, 1, 2.5, 5 and 10 eV pass energies under computer operation.

In the CRR mode operation the pass energy and the energy resolution are not constant during a spectrum scan. But the ratio of the retarding potential to pass energy, V_R/E_p , is constant. The values of CRR is given as

$$CRR = \frac{E_k}{E_p} = \frac{V_R}{E_p} + 1 \quad (2.12)$$

The available values of CRR of the CLAM2 spectrometer are 1, 2, 4, 10, 20, 40 and 100. Typically, this mode is used for AES where peaks occur at low kinetic energy. In addition Auger peaks tend to be broader than photoelectron peaks and energy resolution is not important.

CHAPTER III

DEVELOPMENT OF CONTROL AND DATA ACQUISITION SYSTEM

This chapter describes the control and data acquisition system that I have developed for the BL-4 beamline of the Siam Photon Laboratory. The design considerations and the design of the system, as well as the main components of the system, are explained. The new control and data acquisition system allowed the commissioning of the BL-4 beamline possible. Moreover, the system also provides AIPES experiments using synchrotron light to be carried out at the BL-4 beamline.

3.1 Design Considerations

The BL-4 beamline was originally designed for ARPES experiments using a movable ARUPS10 energy analyzer. However, at the time of my thesis work, ARPES measurement could not be performed because of the insufficient photon flux at the sample position. Thus, the existing spectrometer employing the CLAM2 energy analyzer, which was originally planned for AES, UPS and XPS measurements using laboratory excitation sources, has been adopted to be used for photoemission measurements using synchrotron light in addition to the available techniques. Thus, a new control and data acquisition system has been developed. The newly home-developed allows the AIPES technique to be performed using the synchrotron light from the BL-4 beamline. The system design takes advantage of the salient properties

of synchrotron light, providing various modes of measurement that could not be done by using general laboratory excitation sources such as an X-ray tube, a UV discharge lamp or an electron gun such as the constant initial state (CIS), constant final state (CFS) modes of measurement.

The original spectrometer employing the CLAM2 energy analyzer has been designed only for UPS, XPS, and AES measurements. The Thermo VG Scientific VGX900 software was supplied by the manufacturer of the analyzer for data collection and data analysis. The software has been developed for the measurement techniques using laboratory excitation sources, thus only EDC can be obtained. In the EDC mode, the intensity of photoelectrons is measured as a function of their kinetic energy measuring at fix excitation photon energy. Moreover, the software employs rather out-of-date ISA-bus computer-interfacing hardware. Then, a newly software has been developed for employing the CLAM2 analyzer to measure using synchrotron radiation. In the design of a new control and data acquisition, the following considerations have been taken into account.

- The new system should provide different modes for measuring photoelectrons to take advantage of a tunable synchrotron light source. The energy of photons from the BL-4 beamline can be selected between 20eV and 240eV. This opens the opportunity to measure photoelectrons in two new modes of measurement other than the EDC mode, i.e. CIS and CIF modes. In the CIS mode, the intensity of photoelectrons excited from a given binding energy is measured as a function of excitation energy of photons. While in the CFS mode, the intensity of photoelectrons with a given kinetic energy is measured as a function of excitation energy of photons. A total yield of photoelectrons

emitted from the sample as function of photon energy should also be measured.

- A minimum number of new hardware should be added. In fact, only the out-of-date interfacing card is replaced by a new PCI interfacing card. Moreover, both monochromator and spectrometer system are fully controlled by only one personal computer.
- Finally, the new software should have powerful, flexible and user-friendly interface feature.

3.2 System Design

3.2.1 Hardware

Figure 3.1 shows the schematic diagram of a new data acquisition using the CLAM2 spectrometer installed at the experimental station of the BL-4 beamline. The newly home-developed software has been written using the LabView program of the National Instrument (NI) running under the Microsoft Window 2000 operating system. Only one personal computer is employed to control the monochromator of the beamline, the CLAM2 spectrometer and the pico-ammeters. RS232C interfacing protocol is used for the communication between the computer and the control electronics of the monochromator, i.e. the controller of the steppermotors and the linear encoder. A PCI GPIB interface card is used for communicating with the pico-ammeters. An NI PCI-6052E interface card is used for the communication between the computer and the SCU362 spectrometer control unit of the CLAM2 spectrometer. One of the analog inputs of the NI PCI-6052E card is also used for receiving the electron beam current in the storage ring of the light source. This beam current is used

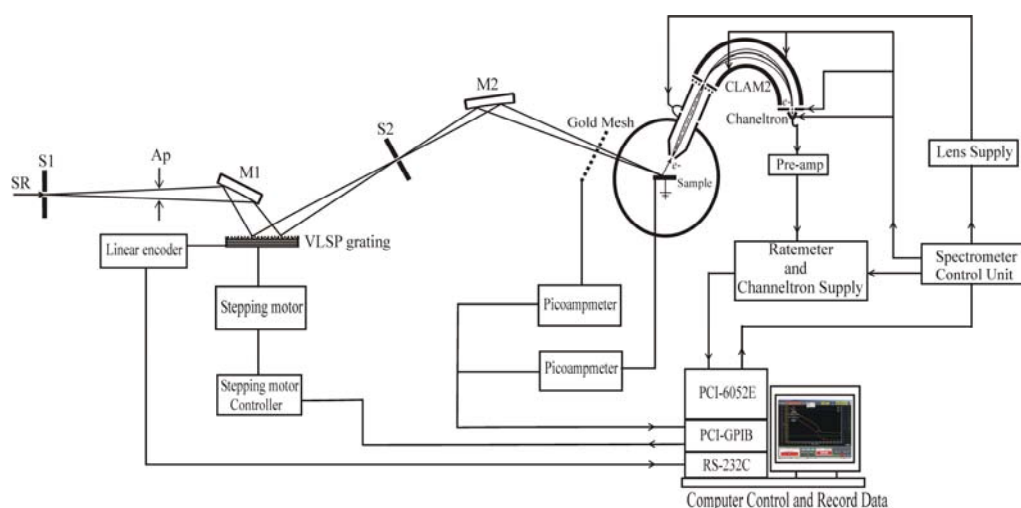


Figure 3.1 The schematic diagram of a new data acquisition using the CLAM2 spectrometer installed at the experimental station of the BL-4 beamline.

The new data acquisition system controls the CLAM2 analyzer via the SCU362 spectrometer control unit. Five digital outputs from the NI PCI-6052E interface card are used for selecting the energy range of the analyzer, the energy analyzing modes (CAE or CRR modes) and the pass energy. One analog output (0-10 V) from the same interface card is used for controlling the retarded potential. One of the four counters of the interface card is used for counting the signals from the channeltron, representing the number of the detected photoelectrons passing through the exit slit of the analyzer.

Figure 3.2 shows the wiring diagram between the interface card and the SCU362 unit. The CAE/CRR signal is used for selecting the energy analyzing mode. When the CAE/CRR is in a high status (+5 V), the analyzer is operated in the CAE mode. For the CRR mode, the CAE/CRR is in a low status (0 V). The status of the other four TTL signals summarized in Tables 3.1, 3.2, and 3.3 are used for the settings of the energy range, the pass energy (or the CAE value), and the CRR values.

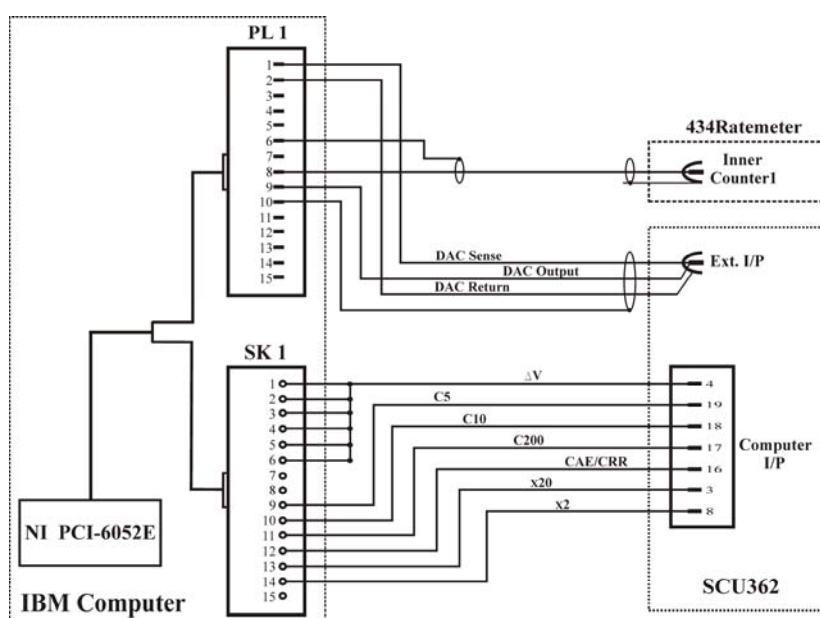


Figure 3.2 The wiring diagram between the interface card and the SCU362 unit.

Table 3.1 The status of TTL signals for different settings of the energy range of the spectrometer.

Energy range	Input status on SCU362	
	Pin x20	Pin x2
81.9 eV	0	1
163.84 eV	0	0
1638.4 eV	1	1
3276.8 eV	1	0

Table 3.2 The status of TTL signals for different pass energies of the analyzer in the EDC mode of measurement. UPS represents the 81.9 eV and 163.84 eV energy ranges, while XPS represents the 1638.4 eV and 3276.8 eV energy ranges.

Pass energy		Input status on SCU362		
UPS	XPS	Pin C200	Pin C10	Pin C5
0.1	2	1	0	0
0.2	5	1	1	0
0.5	10	1	0	1
1.0	20	1	1	1
2.5	50	0	1	0
5	100	0	0	1
10	200	0	1	1

Table 3.3 The status of TTL signals for different settings of the CRR values.

CRR	Input status on SCU362		
	Pin C200	Pin C10	Pin C5
1	0	1	1
2	0	0	1
4	0	1	0
10	1	1	1
20	1	0	1
40	1	1	0
100	1	0	0

When the analyzer is operated in the CAE mode, the 0-10 V analog signal is used to provide suitable retarding voltage to allow the electrons with required kinetic energy to pass through the analyzer. In the CRR, however, the pass energy is varied with the retarded voltage to keep a constant ratio between the pass energy and the kinetic energy of the detected electrons, and thus to keep a constant transmission across the energy range.

The new data acquisition system supports different measurement techniques, i.e. UPS, XPS, AES, and SL-PES (photoelectron spectroscopy using synchrotron light. For UPS, XPS, and SL-PES, the CLAM2 analyzer is operated in CAE mode, while in AES measurement, the analyzer is operated in the CRR mode. Only the EDC measurement mode is employed for UPS, XPS, and AES measurements because the energies of the excitation photons are fixed. When synchrotron light is used in photoemission measurements, different modes of measurements such as EDC,

CIS, and CIF modes can be performed without or with a simultaneous total-yield measurement.

3.2.2 Software

The LabView program has been used to write new software for controlling the monochromator of the BL-4 beamline and the CLAM2 spectrometer. Feedback signals from the beamline and the electron beam current are also collected for the monitoring synchrotron light beam, and thus the electron beam in the storage ring. The data from the feedback system might be used for the normalization of the photoelectron yield measured by using the CLAM2 spectrometer, particularly when the beam is not stable or when there is changed in the light intensity.

The software is has the user-friendly graphic interface feature. Setting of the parameters of the monochromator and spectrometer for different modes of measurements can simply be done by changing the values at six dialog boxes. He detailed description of each dialog boxes is given below.

- Measurement Technique and Modes dialog box: There are four technique measurements, i.e. UPS, XPS, AES and PES by using synchrotron light. The first three techniques requires only the EDC mode of measurement. Thus the mode of measurement is automatically selected by the computer to be the EDC mode. When choosing PES using synchrotron light, different modes of measurement can be performed, i.e. EDC, CFS, CIS, and CIS in a combination with the total electrons yield spectrum modes.



Figure 3.3 Graphical feature of the control and data acquisition software of the BL-4 beamline.

- Photon energy dialog box: This is the input parameters for monochromator. The dialog box is used only for the photoemission experimental technique using synchrotron light. The photon energy can be selected in this dialog box for EDC measurements. In the CIF, CFS and total yield measurements, the photon energy range and the scanning step must be specified. The appropriated gratings must be selected. It should be note that the exchange of the gratings is done manually by a linear drive mechanism. Thus, it should be kept in mind that the required grating is placed in the correct position.
- Kinetic energy and step size dialog box: This is the input parameters for the CLAM2 spectrometer. In the EDC mode of measurement, the range of kinetic energy of photoelectrons and the scanning energy step must be specified in this dialog box. For CIF, CFS and total yield measurement, only the specific value of the kinetic energy is required.
- Pass energy dialog box: This is also the input parameter for the CLAM2 spectrometer. The values of the pass energy to be selected are 0.1, 0.25, 0.5, 1, 2.5, 5 and 10 eV.
- Number of scan dialog box: This dialog box allows users to repeat the measurement several times to the signal-to-noise ratio.
- Number of Sampling dialog box: The NI PCI-6052E interface card used in this data acquisition system has two internal counters. The information obtained is the count rate in counts per second unit. Increasing the number of sampling results also in the improved signal-to-noise ratio.

3.3 Energy Calibration of the CLAM2 Spectrometer

The calibration curve showing the relation between the kinetic energy of an electron, E_k , and the retarding voltage, V_R , must be obtained before using the CLAM2 spectrometer with the new interface card and new software. The retarding voltage is supplied from the output voltage of the SCU362 spectrometer control unit. This output voltage can be remotely controlled by an analog signal (0-10 V DC). This DC voltage can be supplied by the NI PCI-6052E interface card. Thus, the analog DC output of the NI PCI-6052E interface is used instead of the retarding voltage in the calibration of the CLAM2 spectrometer.

The calibration of the kinetic energy of measured electrons has been performed using standard gold and copper samples. Table 3.4 shows the binding energies of core electrons of copper and gold, and the kinetic energy of Cu L_3MM Auger electrons used as the reference in the energy calibration of the CLAM2 spectrometer. From equation (2.9), the kinetic energy of electrons that can pass through the energy analyzer is a linear function of the retarding voltage. For the CLAM2 spectrometer, the retarding voltage is controlled by the 0-10 V analog signal driven by the NI PCI-6052E interface card. Figure 3.4 is the calibration curves showing the relation between the kinetic energy of electrons measured by the CLAM2 spectrometer and the control voltage of the NI PCI-6052E card for different energy ranges. Mg K_α radiation ($\hbar\omega = 1253.6$ eV) has been used for the excitation in the calibration procedure. The work function of the spectrometer, claimed by the manufacturer, is 4.2 eV. This value is confirmed by measuring photoelectrons near the Fermi edge of gold using He I radiation ($\hbar\omega = 21.2$ eV) for the excitation, as shown in Figure 3.5.

Table 3.4 The binding energies are used as the reference in the energy calibration of the CLAM2 spectrometer.

Peak	Binding energy (eV)	reference
Cu 2p _{3/2}	933.00	Oswald (2000)
Cu L _{3MM}	334.94	Seah and Smith (1996)
Cu 3p _{3/2}	75.00	Oswald (2000)
Au 4f _{5/2}	87.60	Fuggle and Mårtensson (1980)
Au 4f _{7/2}	84.00	Seah and Smith (1996)

Table 3.5 The energy calibration curve for the CLAM2 spectrometer obtained and used in this work. V_{dc} and E_k are the control voltage for the spectrometer and the electron kinetic energy, respectively.

Photoemission	Energy ranges	Linear equations
UPS	0-81.92 eV	$V_{dc} = 0.12114 E_k + 1.38000 \times 10^{-4}$
UPS	0-163.48 eV	$V_{dc} = 0.06056 E_k + 1.38717 \times 10^{-4}$
XPS	0-1634.8 eV	$V_{dc} = 0.00610 E_k - 5.30900 \times 10^{-4}$
AES	0-3276.8 eV	$V_{dc} = 0.00304 E_k - 2.95000 \times 10^{-3}$

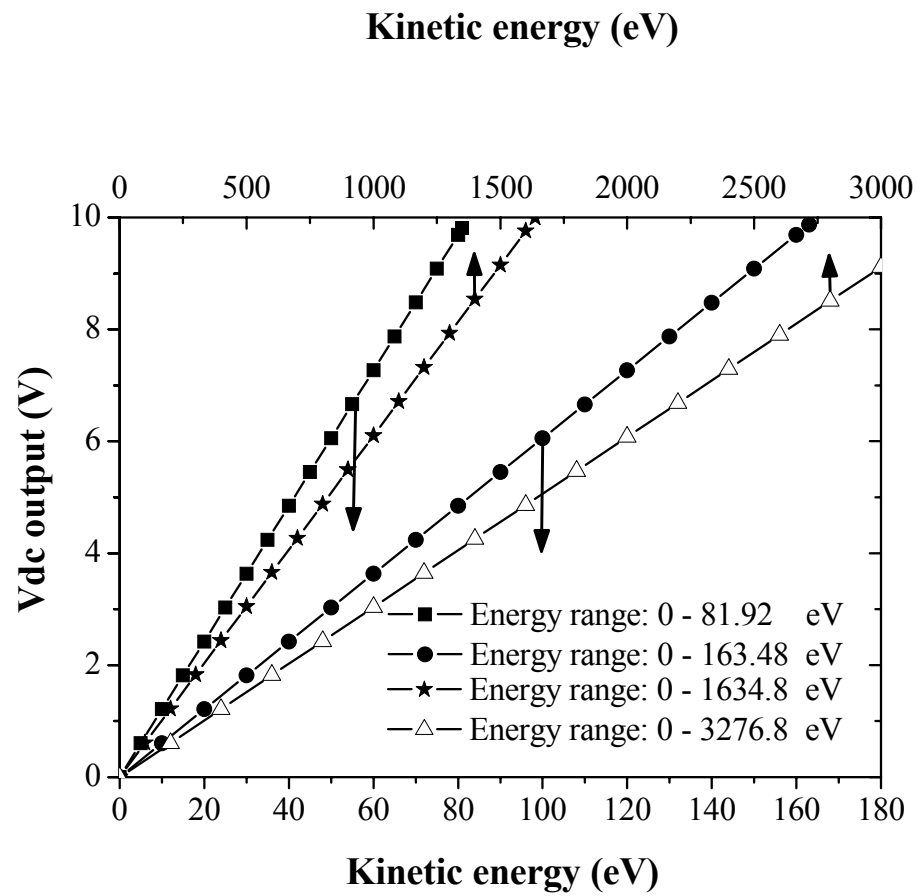


Figure 3.4 The calibration curve showing the analog 0-10V DC input of the SCU362 spectrometer control unit as a function of the kinetic energy of electron.

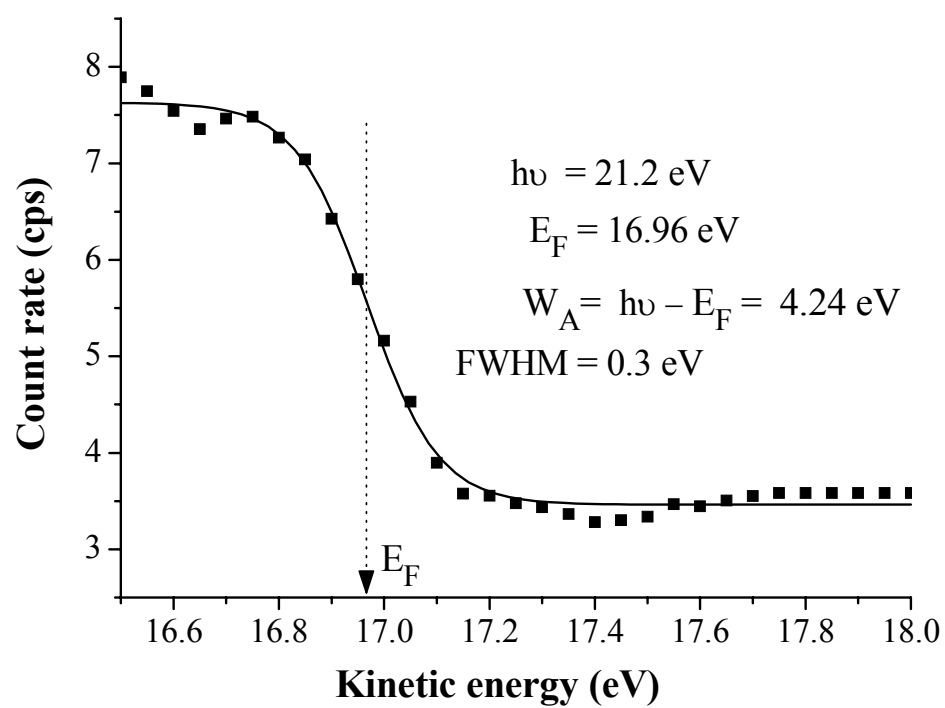


Figure 3.5 The photoemission spectra of gold showing the Fermi edge.

The new data acquisition has been tested by taking spectra in different modes of measurement. The results are shown in Figure 3.6 and Figure 3.7. Figure 3.6 shows XPS spectra taken from copper and gold samples using Mg K_{α} radiation. Figure 3.7 is an AES spectrum taken from a cleaned Cu sample using 5 keV electrons for the excitation.

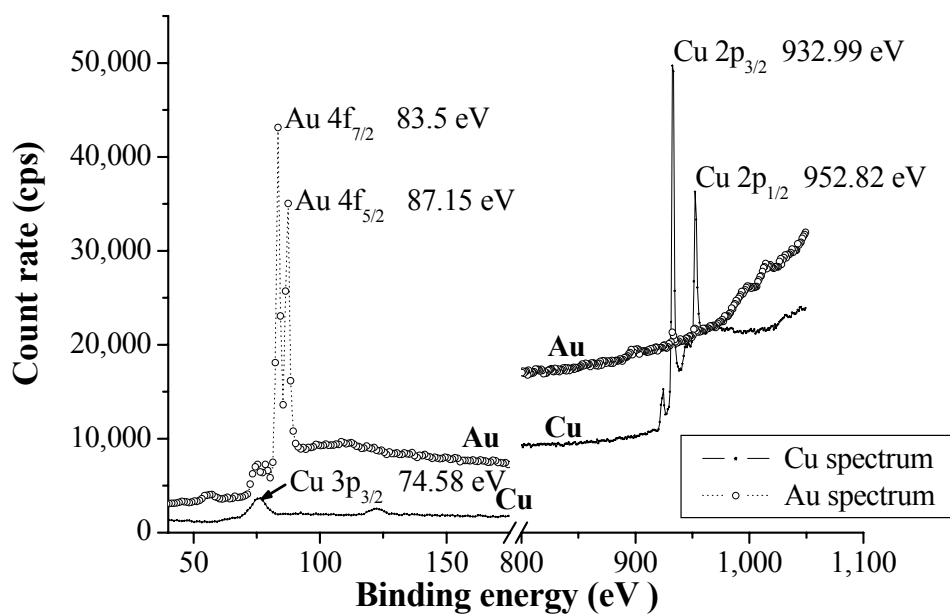


Figure 3.6 Photoemission spectra of gold and copper taken by using the new control and data acquisition system developed in this thesis work.

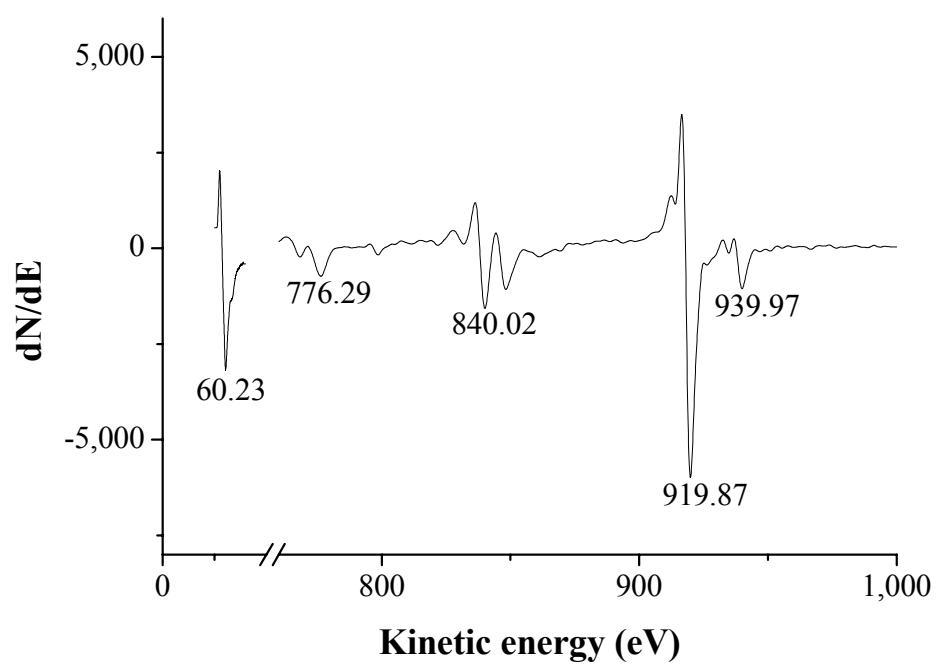


Figure 3.7 The Auger spectrum of copper taken by using the new control and data acquisition system developed in this thesis work.

CHAPTER IV

RESULTS AND DISCUSSIONS

This chapter reports the results obtained from the commissioning of the BL-4 beamline of the Siam Photon Laboratory. The results obtained from the measurements are compared to those obtained from ray-tracing simulations. The causes for the discrepancies of the measurement results from the expected theoretical values are discussed. The optical path analysis is also treated to check the possible causes.

4.1 Source

The BL-4 beamline utilize synchrotron light produced in the BM4 bending magnet of the storage ring. Figure 4.1 shows the intensity distributions of synchrotron light at the source position and at the distance of 7300mm from the source generated by ray-tracing computer simulations. The source point is in the BM4 bending magnet, at the position where synchrotron light is used for the BL-4 beamline. The input parameters of the source for the simulation are given in Table 4.1. It should be noted that the x -axis is the direction perpendicular to the optical axis. The source has a Gaussian-like distribution. The dimension of the source is thus defined by the standard deviation (σ) or the full-width-at-half-maximum ($FWHM$). $FWHM$'s of the intensity distributions of the source in the horizontal and vertical directions are 0.469 mm and 0.191 mm, respectively.

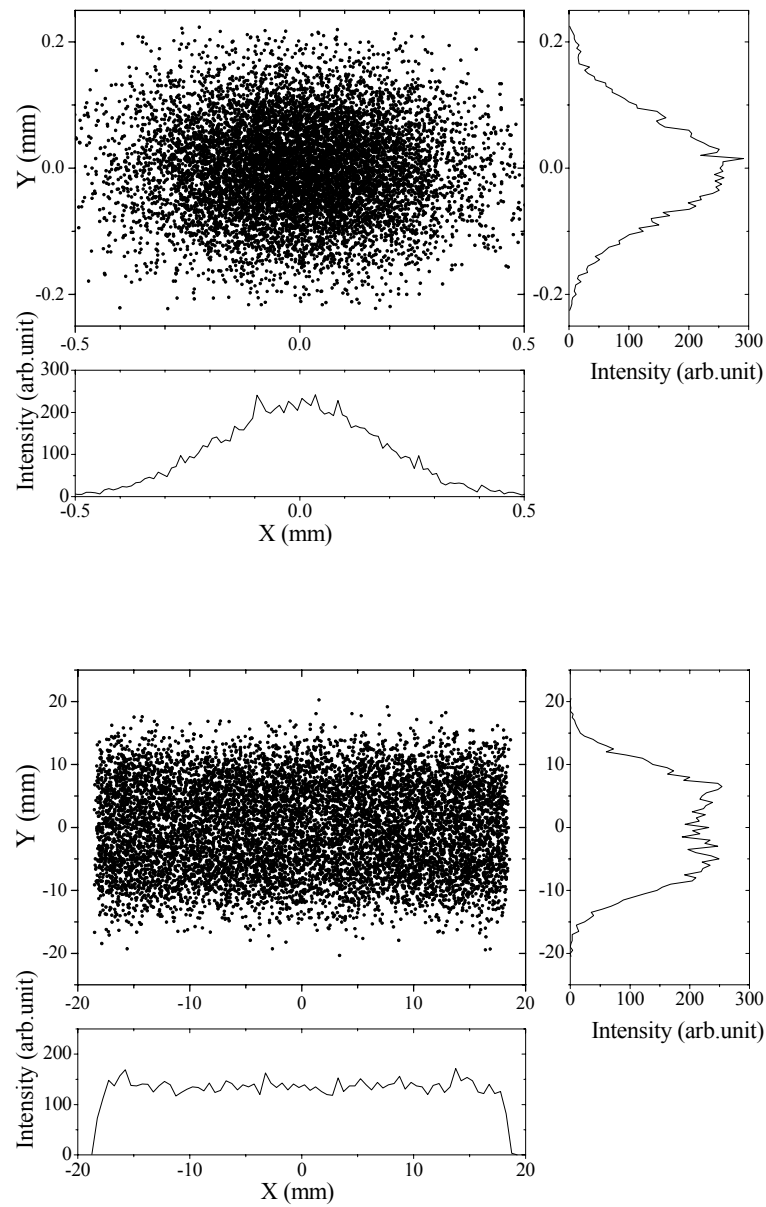


Figure 4.1 The intensity distribution of the light source in the BM4 bending magnet (a) at the source position and (b) at the distance of 7300 mm from the source obtained from ray-tracing simulations.

Table 4.1 Input parameters for the source of synchrotron light in the BM4 bending magnet.

Natural emittance	74 nm mrad
σ_x , FWHM _x	0.185 mm, 0.469 mm
σ_y , FWHM _y	0.076 mm, 0.191 mm
Electron energy	1.0 GeV
Magnetic field	1.2 Tesla

The intensity distribution of the synchrotron light at the distance of 7300 mm from the source position is shown in Figure 4.1(b). The image plane is perpendicular to the optical axis. The simulation was obtained with the opening angle in the horizontal direction of 5 mrad and full opening in the vertical direction. The figure reveals the divergence nature of synchrotron light. The nominal angular width of synchrotron light emitted from bending magnet sections is $1/\gamma$. For a 1.0 GeV storage ring, the angular width is about $1/2000 = 0.5$ mrad. Thus the size of the beam in the vertical direction at the distance of 7300 mm would be $0.0005 \times 7300 \text{ mm} = 3.65 \text{ mm}$. The discrepancy between the simulated and theoretical results is due to the finite size of the source in the simulation. In the horizontal direction, the beam size increases accordingly to the opening angle, which is 5 mrad.

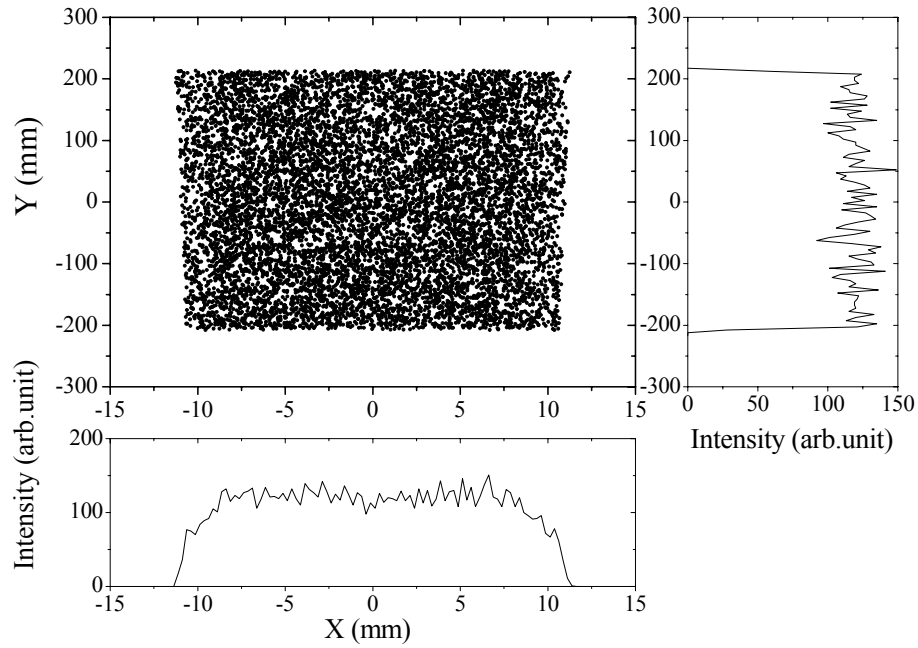


Figure 4.2 The intensity distribution of light beam on the surface of the pre-focusing mirror obtained from ray-tracing simulation.

Figure 4.2 shows the intensity distributions of light on the surface of the pre-focusing mirror. In the simulation, the parameters of real components in the front-end part of the BL-4 beamline were used. The masks in the front-end part of the beamline define the opening angles in the horizontal and vertical directions of 5mrad and 3mrad, respectively. The mirror is aligned to reflect the beam in the horizontal plane with the angle of incidence of 5° . The y -axis is normal to the mirror surface at the center of the mirror. The plane of reflection is the y - z plane, as shown in Figure 2.18. Due to the grazing geometry, the large area of the mirror surface is required to reflect the beam. The required area of the reflecting surface of the mirror should be at least $23 \times 450 \text{ mm}^2$. The pre-focusing mirror has the active area of $45 \times 520 \text{ mm}^2$. Thus, all

light rays passing through the masks in the front-end will certainly incident on the active area of the pre-focusing mirror.

4.2 Imaging and Focusing Properties

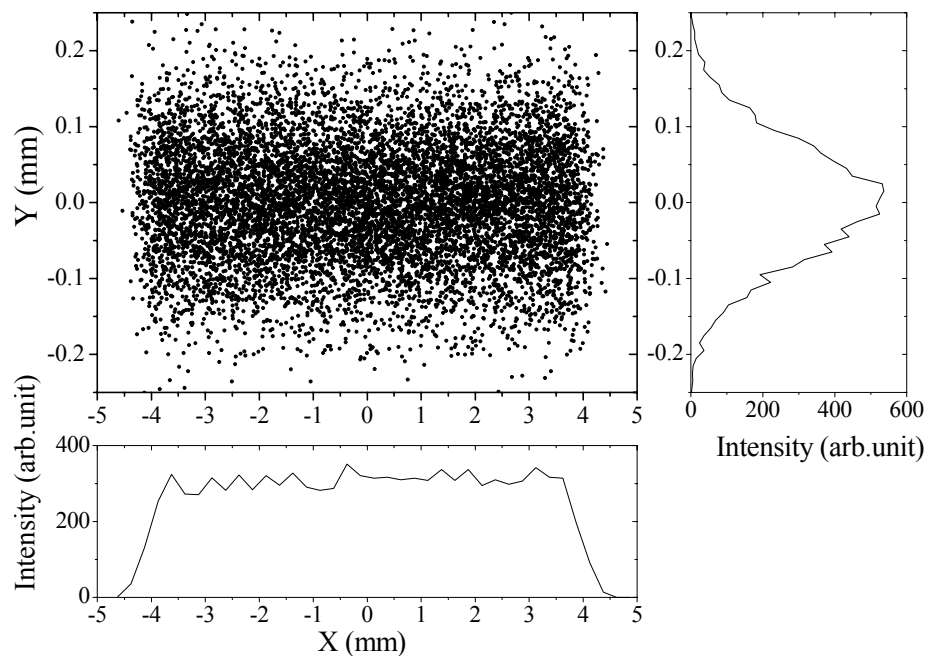


Figure 4.3 The simulated intensity distribution of synchrotron light at the position of the entrance slit of the monochromator.

Figure 4.3 shows the intensity distribution of synchrotron light reflected from the pre-focusing mirror and focused on the entrance slit of the monochromator. The image plane is at the position of the entrance slit, which is located 7300 mm downstream of the pre-focusing mirror. As the exit and entrance arm lengths of the pre-focusing mirror in the vertical direction are the same length, i.e. 7300 mm, the demagnification of the mirror is 1. Thus, the intensity distribution of synchrotron light

in vertical direction at the entrance slit represents the intensity distribution in vertical direction of the light source. From the ray-tracing simulation, FWHM of the intensity distribution of synchrotron light in the vertical direction was found to be 0.387 mm, which is roughly the same the size of the source ($\sim 2\%$ bigger). The slight difference of the distributions of the source and that of the image is caused by the optical aberrations. It is more obvious to observe the optical aberrations in the horizontal direction. The aberrations results in the asymmetrical distribution around the center. This is normal when a toriodal mirror is used to focus a light beam in a grazing geometry, when the size of the optical element is comparable to the entrance or/and exit arm lengths. The aberrations from a toriodal mirror become more obvious when the source size is a point source.

At the BL-4 beamline, synchrotron light in the visible region on the entrance slit can be observed by a naked eye. The observed image on the entrance slit is similar to the simulated image. The width of the light beam is about 8 mm. The intensity distribution of synchrotron light has been studied in detailed since it represents the intensity distribution of light of the source in the vertical direction, i.e. the vertical size of the electron beam in the storage ring. The width of the entrance slit can be varied from 0 to 1500 micron in the vertical direction, i.e. the opening of the slit is perpendicular to the dispersive plane of the monochromator. The relative intensity of the focused synchrotron light passing through the opening of the slit can be measured. In the measurement, a retractable stainless steel plate coated with goal is inserted to the optical axis at the position just behind the entrance slit. The photocurrent (or drain current) caused by the emission of electron excited by the synchrotron light is measured by a pico-ammeter. The intensity distribution of the light beam in the vertical direction can be obtained by varying the slit width or scanning the focused

beam on the entrance slit in the vertical direction. The two methods yielded similar results.

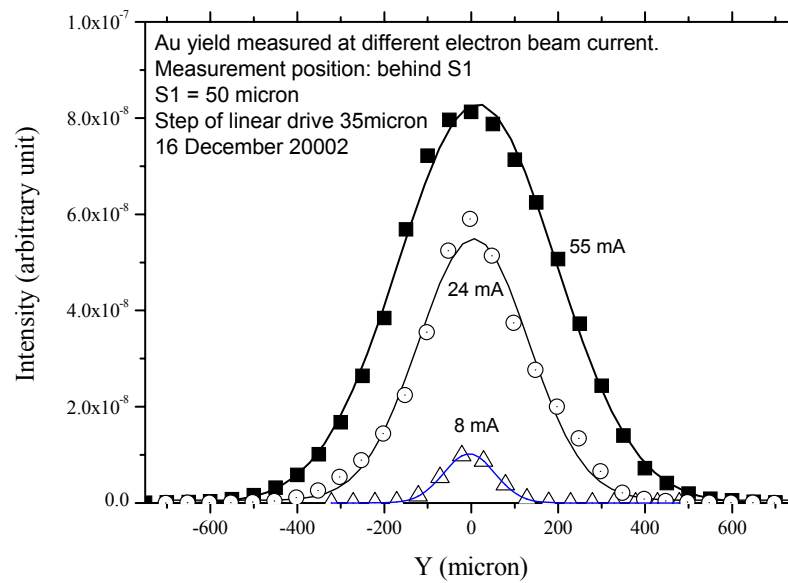


Figure 4.4 The intensity distribution of synchrotron light in the vertical direction measured at the entrance slit of the monochromator for the electron beam currents in the storage ring of 8mA, 24mA and 55mA.

Figure 4.4 shows the intensity distribution of synchrotron light in the vertical direction measured at the entrance slit of the monochromator for the electron beam currents in the storage ring of 8 mA, 24 mA and 55 mA. The intensity distributions have the Gaussian profiles. *FWHM*'s of the distributions are 0.117 mm, 0.252 mm and 0.360 mm for the electron beam current of 8 mA, 24 mA and 55 mA, respectively. The results clearly show the increase of *FWHM* of the distribution with the electron beam current.

Figure 4.5 shows *FWHM* of the intensity distribution of the synchrotron light beam in the vertical direction as a function of the electron beam current measured at the entrance slit of the monochromator. The measurement results were obtained on different dates. The same machine parameters were used for the operation of the light source. The vertical beam size increases with the increasing of the electron beam currents for the three machine operations. In stable storage rings, the size of the electron beam does not depend on the electron beam current. The possible cause of the increase of the beam size was the instability of the electron beam, probably due to ion trapping effects.

It was observed also that there was the fluctuation of the light beam position on the entrance slit. The fluctuation could be observed by a naked eye, the amplitude of the fluctuation was about 1 mm. The variation in the light beam position was slow. The observed results directly indicated the instability of the electron beam in the storage ring. The main caused of the instability of the electron beam responsible for the movement of the light beam was later identified to be the electrical shortage of the coils in the quadrupole magnets of the storage ring.

The X-Y aperture is also an important optical element when high resolving power of the monochromator is required. The aperture defines the opening angle of the light beam for the downstream optical elements, i.e. the focusing mirror and the grating. The smaller aperture, the higher resolution of the monochromator will be obtained. This is due to the fact that optical aberrations reduced when the illuminated area of the optical element reduces. It should also be noted that the photon flux also reduces when the X-Y aperture reduces.

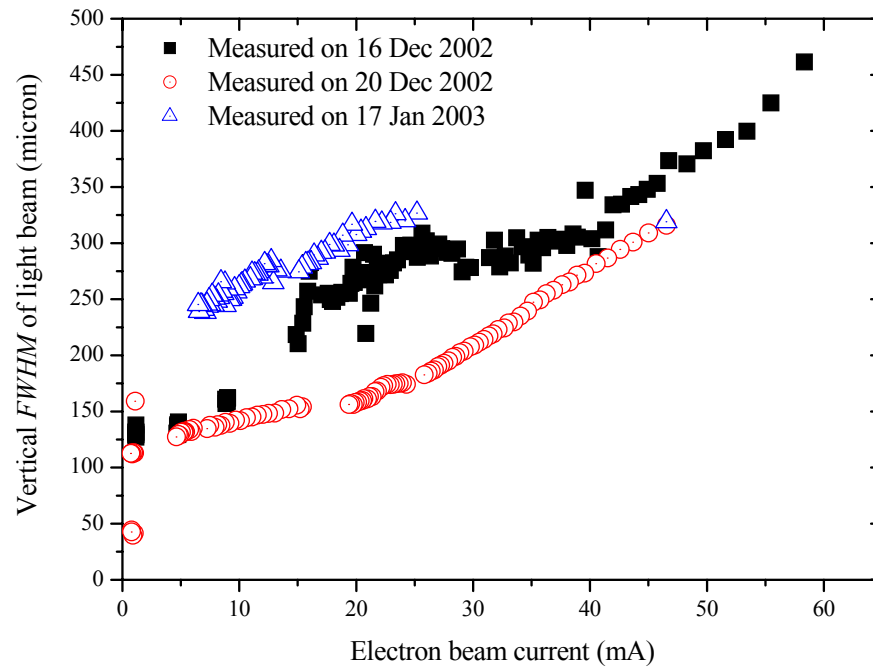


Figure 4.5 *FWHM* of the synchrotron light beam in the vertical direction as a function of the electron beam currents measured on different dates with the same machine parameters for the operations of the light source.

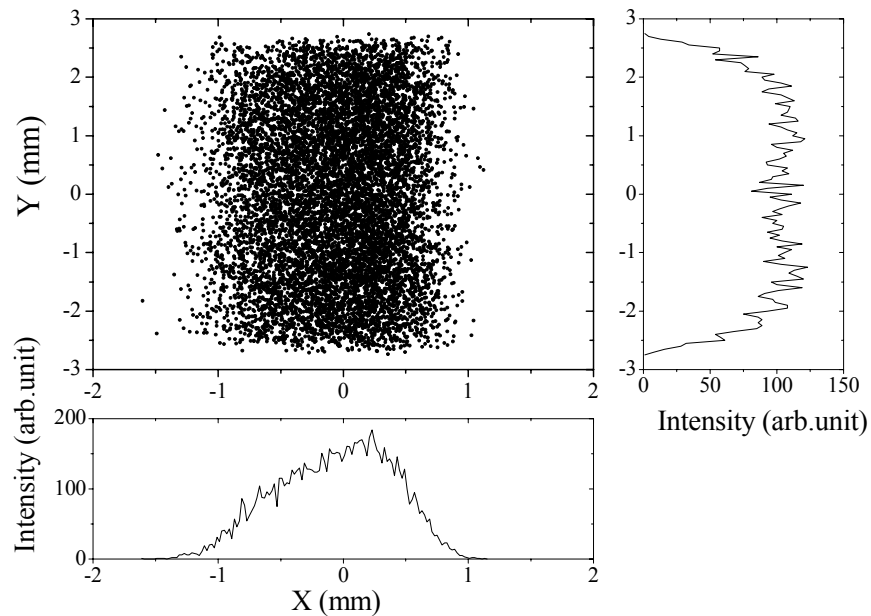


Figure 4.6 The intensity distribution of synchrotron light beam at position of the X-Y aperture when the entrance slit is widely opened.

In the horizontal plane, the light beam reflected from the pre-focusing mirror is focused at the position between the X-Y aperture and the focusing mirror, see also Figure 2.11. Thus the beam size in the horizontal direction at the X-Y aperture is small but still adjustable by the X-Y aperture if necessary. Figures 4.6 and 4.7 show the intensity distributions of the light beam at the X-Y aperture when the widths of the entrance slit are fully opened and 200 micron, respectively. The beam size in the vertical direction is about 5 mm, which is more or less the same as the width of the beam observed at the BL-4 beamline. The vertical beam size at the X-Y aperture has almost no change when the width of the entrance slit was reduced to 200 micron. This is due to the fact that the beam size is focused at the entrance slit, and the size of the focused beam is about the same size of the slit width.

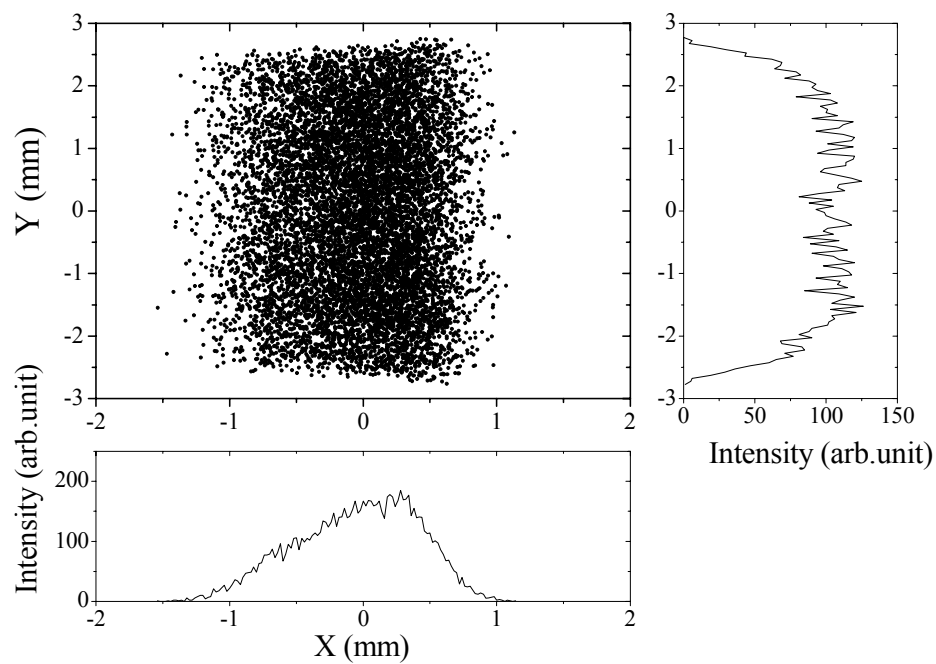


Figure 4.7 The intensity distribution of synchrotron light beam at position of the X-Y aperture when the width of the entrance slit is 200 micron.

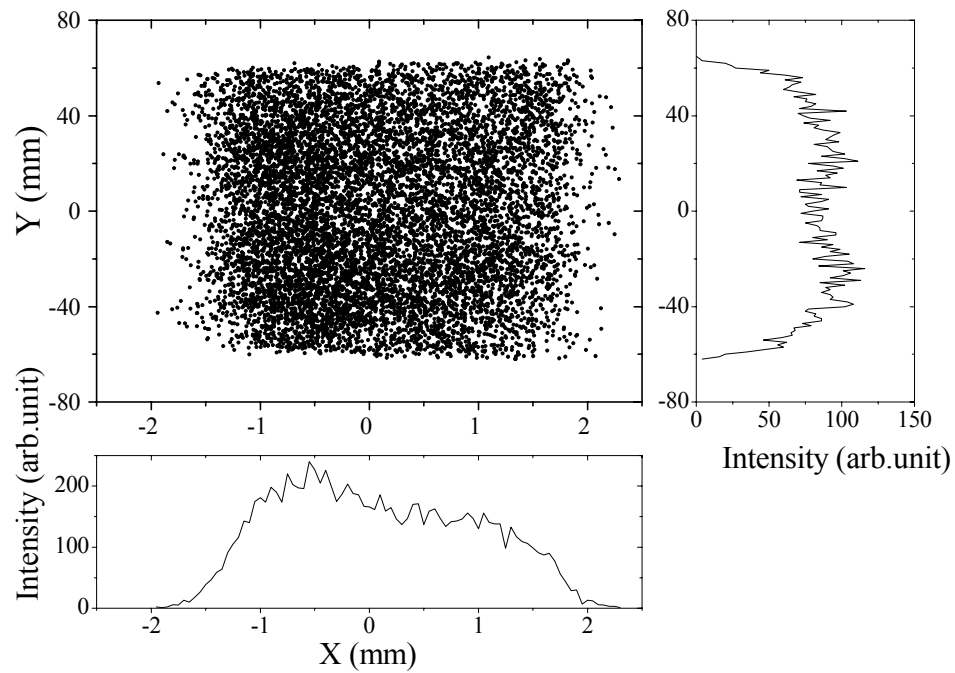


Figure 4.8 The intensity distribution of synchrotron light beam on the surface of the focusing mirror when the entrance slit and the X-Y aperture are fully opened.

Figure 4.8 shows the intensity distribution of synchrotron light beam on the surface of the focusing mirror when the entrance slit and the X-Y apertures are widely opened obtained from a ray-tracing simulation. The illuminated area of the surface of the mirror is a rather large area covering the area of about $4 \times 120 \text{ mm}^2$. However, the active surface area of the focusing mirror is $40 \times 120 \text{ mm}^2$, which is bigger than the required area.

When the width of the entrance slit was reduced to 200 micron, no significant change in the distribution is observed, as shown in Figure 4.9. The value of 200 micron was selected for convenience in the experiments that sufficient photon with reasonable resolution could be obtained. The length of the illuminated area on the focusing mirror is greatly reduced when the X-Y aperture is limited to 500 micron. The distribution of the light intensity is shown in Figure 4.10. The illuminated area of the mirror surface, as well as the photon flux, reduces about 12 times, comparing to the previous cases.

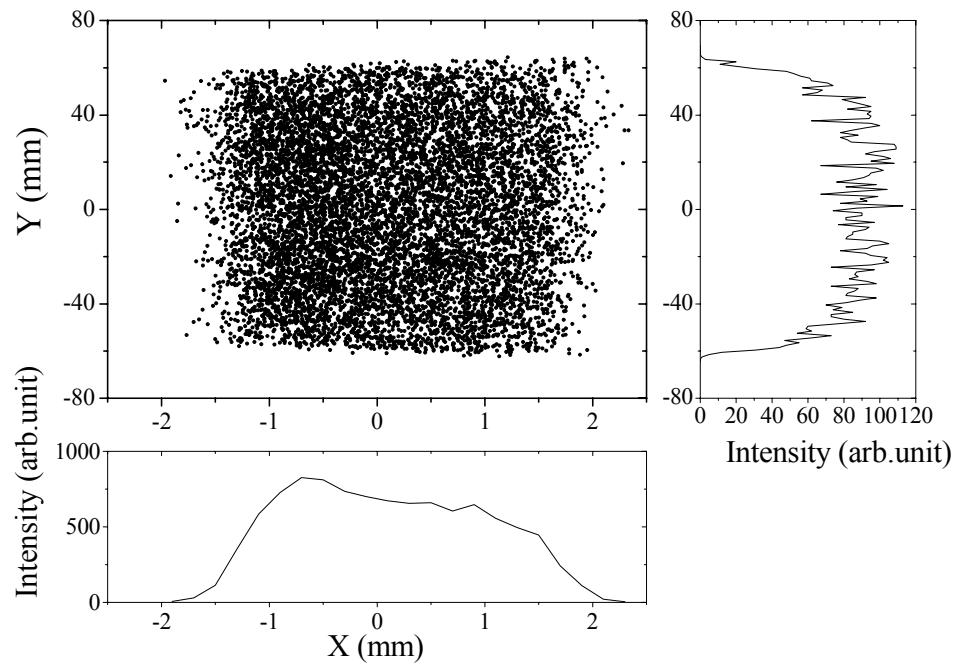


Figure 4.9 The distribution of the synchrotron light beam on the surface of the focusing mirror when the width of entrance slit is 200 micron and the X-Y aperture is fully opened.

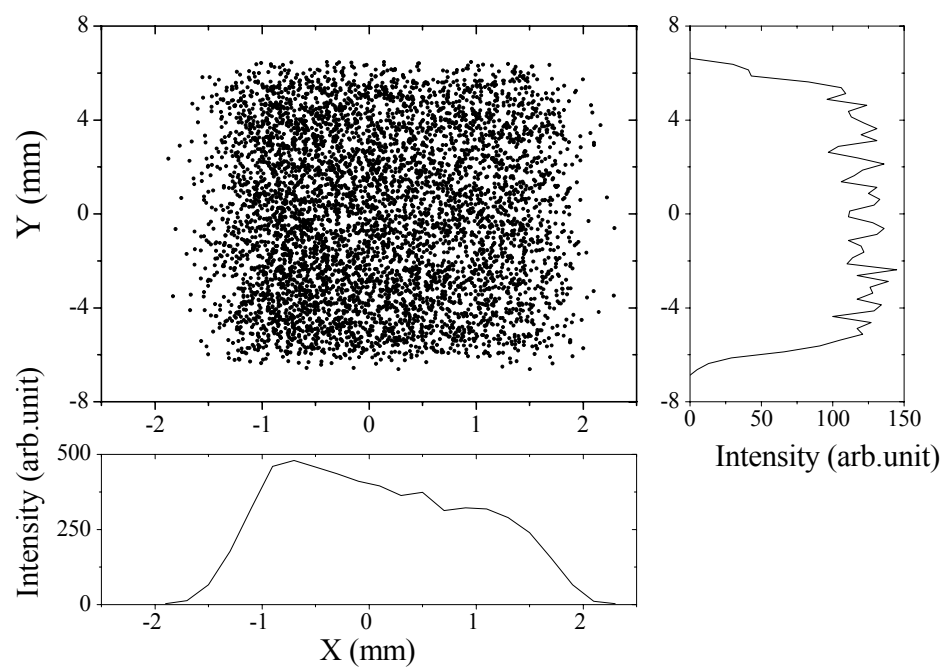


Figure 4.10 The distribution of the synchrotron light beam on the surface of the focusing mirror when the width of entrance slit is 200 micron, the X-Y aperture is widely opened in horizontal direction and is 500 micron in the vertical direction.

The design of the BL-4 beamline allows the reflected light from the focusing mirror to be observed on a monitoring pole, which is located downstream of the grating chamber as shown in Figure 4.12. By the linear translation of the grating exchanging mechanism, the spaces between the holders of the gratings can be aligned to allow the light beam passing through. A CF70 viewport is mounted on the mounting flange of the grating chamber perpendicular to the optical axis of the light beam reflected from the focusing mirror. The focusing mirror reflects the light beam through the view pole and form the image on the monitoring pole as shown in Figure 4.11.

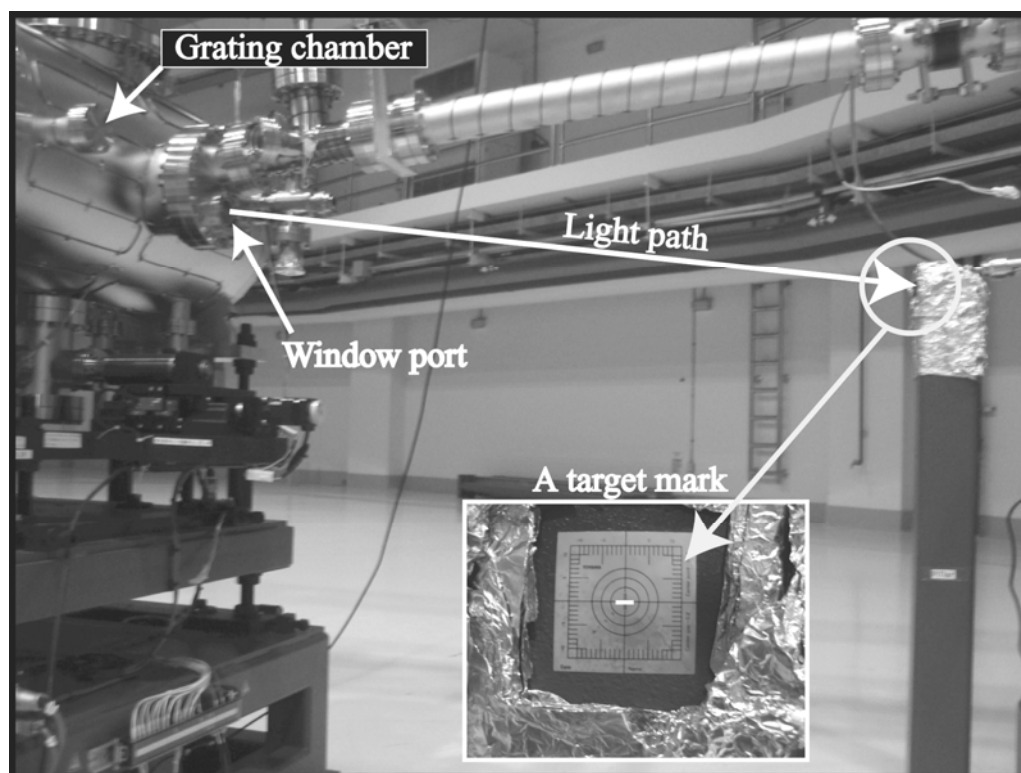


Figure 4.11 The photo of the grating chamber showing the location of the monitoring pole and image of the light reflected from the focusing mirror incidents on the pole.

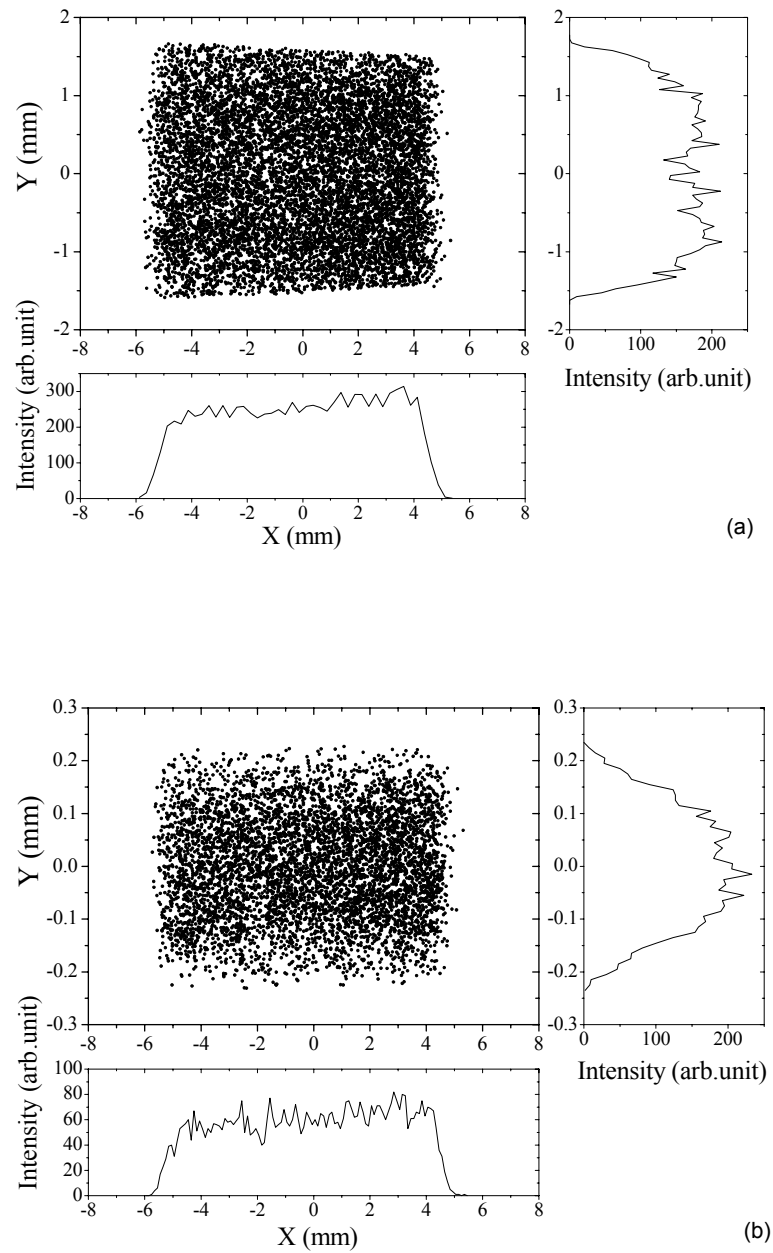


Figure 4.12 The intensity distribution of synchrotron light on the monitoring pole when the width of entrance slit is 200 micron and the X-Y aperture is (a) fully opened and (b) 500 micron in the vertical direction.

Ray tracing simulations have been performed to obtain the intensity distribution of light on the monitoring pole. Figure 4.12(a) and 4.12(b) are the simulations results when the entrance slit width is 200 micron. The beam size on the monitoring pole obtained from the simulations is in good agreement with that of the observed beam. It should be noted that this monitoring pole is essential for the alignment of the focusing mirror. Fine alignment of the focusing mirror can be done by adjusting the tilts and translation of the holder of the mirror. This is done by using a magnetic coupling screw driver, manipulating from the outside of the vacuum chamber.

Figure 4.13 shows the intensity distribution of synchrotron light on the surface of the grating when the width of entrance slit is 200 micron. When the X-Y aperture is fully opened, the active area of the grating has to be $\sim 5 \times 80 \text{ mm}^2$ at least to cover the illuminated area. The active area of the three gratings used in the monochromator is $22 \times 135 \text{ mm}^2$, which is more than enough to diffract the incident beam. The size of the illuminated area is very important regarding to the resolving power of the monochromator. From equation (1.63), the astigmatic aberration increases as the square of the width of the illuminated area. When the width is taken to be 5 mm, the magnitude of the astigmatic aberration for the monochromator of the BL-4 is not significant. Thus the opening of X-Y aperture in the horizontal direction can be fully opened.

The length of the illuminated area on the grating is essential factor for the resolving of the monochromator. As given in equations (1.61) to (1.64), the major optical aberrations such as defocus, coma and spherical aberrations increase in magnitude when the length of the illuminated area increases, resulting in poor resolving power of the monochromator. Thus, the opening of the X-Y aperture in the

vertical direction is used to limit the illuminated area on the grating when high resolving power of the monochromator is required. The length of the illuminated area of the surface of the grating is about 80 mm when the X-Y aperture is fully opened. The length is reduced to 8 mm, when the vertical opening of the X-Y aperture is 500 micron. From equations 1.61 to 1.64, the major aberrations are greatly reduced when the vertical opening of the X-Y aperture is small. However, there is a theoretical limit of the resolving power, which is given as

$$\text{Resolving power} \equiv \frac{\lambda}{\Delta\lambda} = W \cdot N. \quad (4.1)$$

where W is the length of the illuminated area and N is the groove density of the grating. Considering the grating with the groove density of 300 lines/mm at the center of the grating, the maximum resolving power when the vertical opening of the X-Y aperture is 500 micron would be about $8 \text{ mm} \times 300 \text{ lines/mm} = 2400$. This value is almost two times smaller than that of the design value of the monochromator, which is 5000. Thus one should keep in mind when the small vertical opening of the X-Y aperture is used for the grating with the lowest groove density, the maximum resolving power is limited by the illuminated length of the grating.

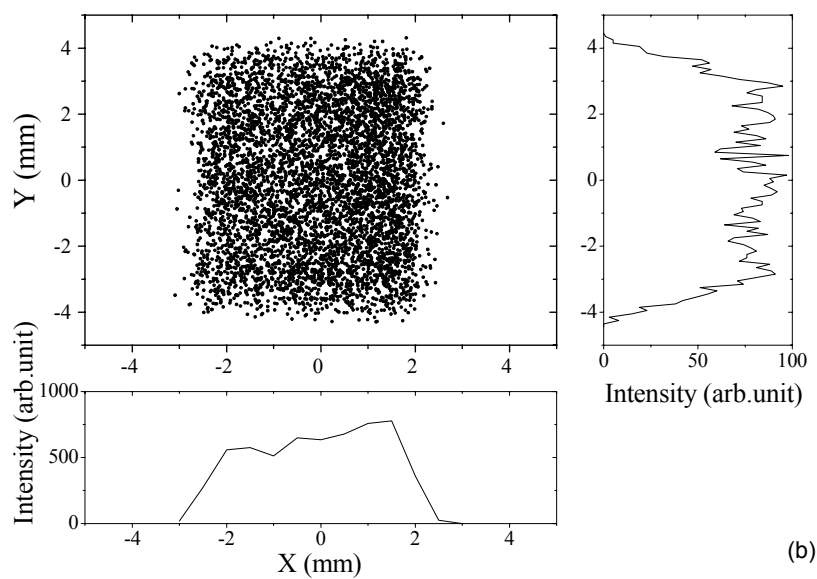
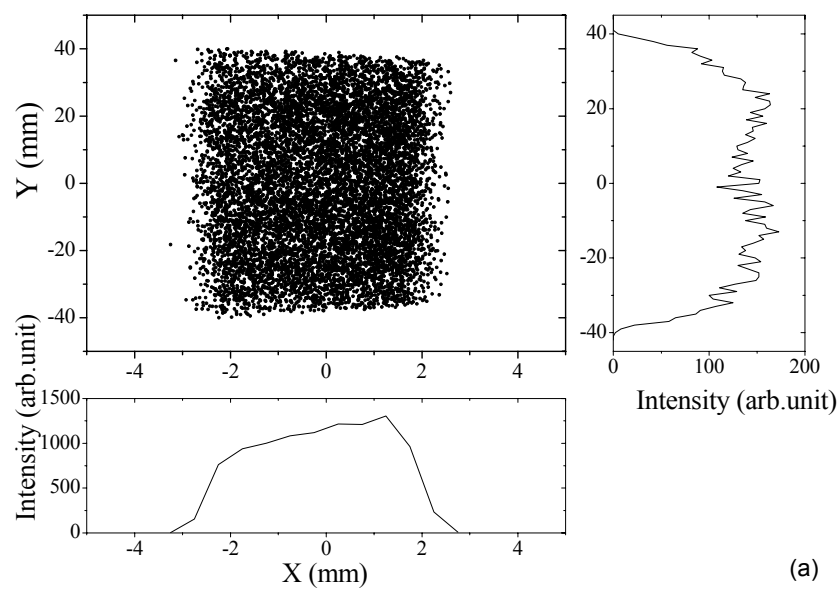


Figure 4.13 The intensity distributions of synchrotron light on the grating when the width of entrance slit is 200 micron and the X-Y aperture is (a) fully opened and (b) 500 micron in the vertical direction.

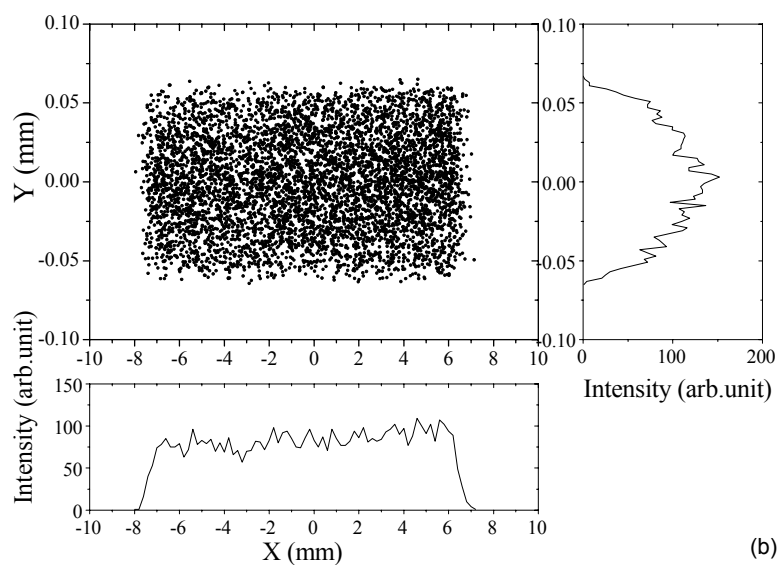
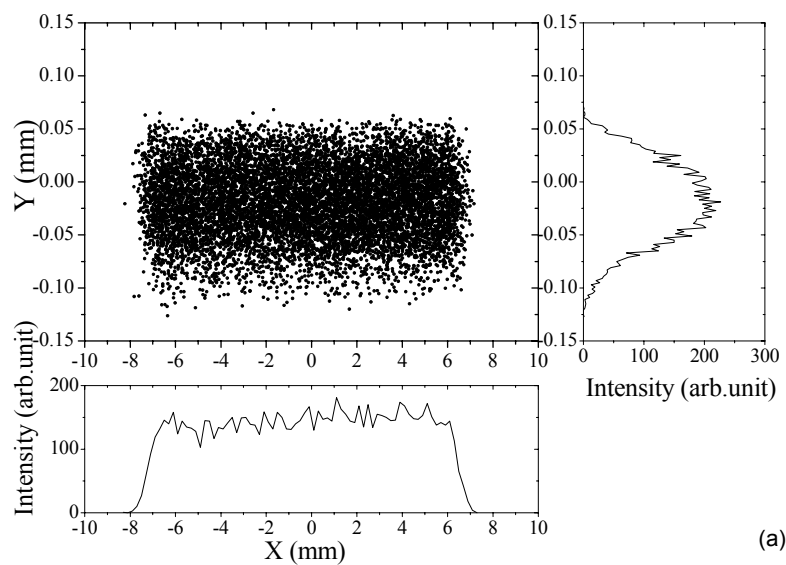


Figure 4.14 The intensity distribution of the 40 eV light beam at the exit slit of the monochromator when the width of entrance slit is 200 micron and the X-Y aperture is (a) fully opened and (b) 500 micron in the vertical direction.

Figure 4.14 shows the intensity distribution of monochromatic light with photon energy of 40 eV at the exit slit of the monochromator obtained from a ray-tracing simulation. The energy band width will be discussed in the section below. The width of the entrance slit of 200 micron was used in the simulation. The diffraction light is obtained at the position of the slit as designed. The intensity distribution of light in the vertical direction is not a Gaussian profile as that at the entrance slit. The change of the profile is due mainly to the optical aberrations of the focusing mirror and the grating. When the X-Y aperture is fully open, *FWHM* of the intensity distribution of the monochromatic light in the vertical direction is approximately 0.211 mm. This value is roughly the same as that at the entrance slit. The slightly bigger size is caused by optical aberration. At photon energy of 40 eV, the angles of incidence and diffraction are 84.5411° and 80.4587°, respectively.

The intensity distribution of monochromatic light on the post-focusing mirror is shown in Figure 4.15. The shape of the mirror surface is a toroidal shape. The asymmetries of the intensity distribution are obvious both in the horizontal direction and the direction along the optical path. The mirror is located at the distance of 1600 mm upstream the sample position. This short arm length of the mirror results in the significant optical aberrations. However, the aberrations only increase the beam size and change the shape of the beam. As the incident light beam is the monochromatized light beam, the aberrations have no influences on the resolution of the optical beamline. The images of the light beam at the sample position are shown in Figure 4.16. When the vertical opening of the X-Y aperture becomes smaller, the aberrations are easier to be observed as shown in Figure 4.7. The total demagnifications of the optical system of the BL-4 beamline are 2.5 and 1.0 in the horizontal and vertical

directions, respectively. Thus in the vertical direction, the beam size is expected to be the same as the width of the entrance slit when the X-Y aperture is fully opened. In the horizontal direction, in principle, the beam size would be 2.5 times smaller than the source size. It was found from the simulation that *FWHM*'s of the intensity distribution are 0.655 mm and 0.190 mm in the horizontal and vertical directions, respectively. The results obtained from the ray-tracing simulations are bigger than the expected values. This is due to the contribution of the optical aberration and the figure error of the optical elements. It has also been shown that the opening of the X-Y aperture influences slightly on the size of the beam size at the sample position. A small beam size with *FWHM* of about 1.0 mm or less can be obtained at the sample position, which is important for angle-resolved photoemission experiments. The beam size can be reduced further when the width of the entrance or/and exit slits decrease, i.e. the higher energy resolution, the better angular resolution will be obtained.

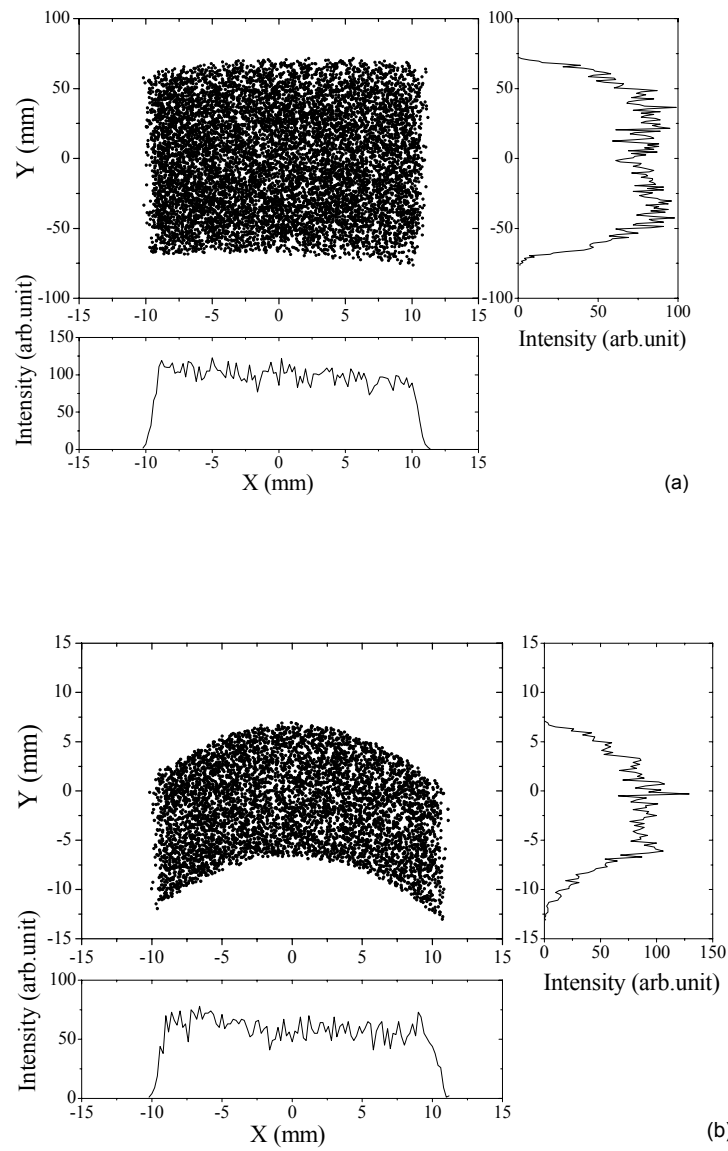


Figure 4.15 The intensity distribution of the 40 eV light beam on the post-focusing mirror when the widths of the entrance and exit slits are 200 micron and the X-Y aperture is (a) fully opened and (b) 500 micron in the vertical direction.

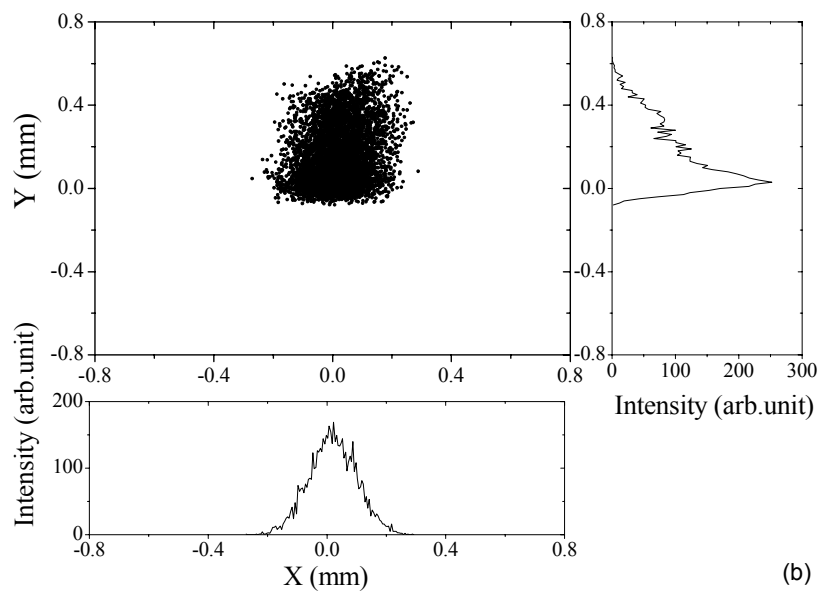
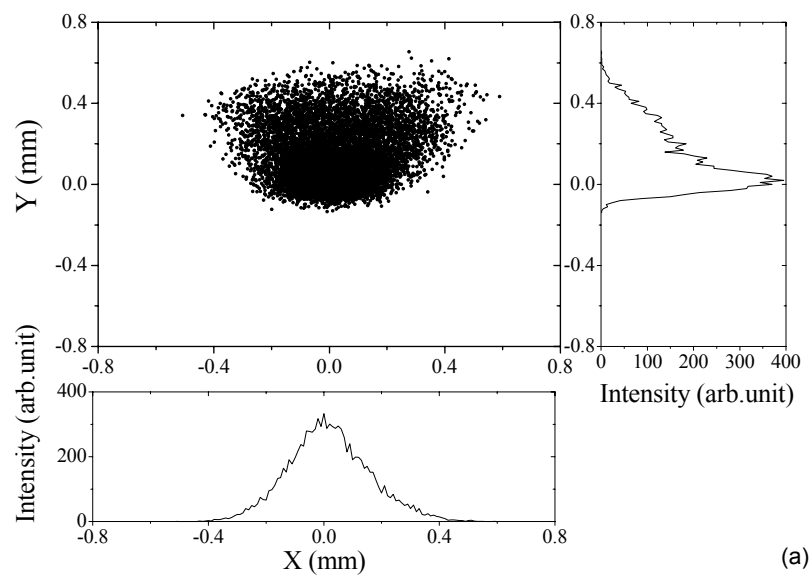


Figure 4.16 The intensity distribution of the 40 eV light at the sample position when the widths of the entrance and exit slits are 200 micron and the X-Y aperture is (a) fully opened and (b) 500 micron in the vertical direction.

4.3 Energy Calibration of the Monochromator

For a constant included angle VLSPG monochromator, the energy/wavelength calibration curve of the monochromator is the relationship between the energy/wavelength of the monochromatized light and the displacement of the linear drive for the sine bar, as given in equation (2.3). The wavelength is a linear function of the linear displacement. In principle, it is possible to find the calibration curve from calculations since the angles of incidence and diffraction can be calculated directly and the mirror plane of the gratings can be found experimentally. Thus the rotating angle, $\phi = (\alpha + \beta)/2$, of the grating with respect to the normal of the mirror plane of the grating can be obtained from calculations. The length of the sine bar of the BL-4 beamline is 300 mm. The displacement of the linear drive of the sine bar, R , is given in equation (2.2) as $R = L \sin \phi$.

For accurate calibration works, the Fermi edge of gold spectra have been used for the first two gratings with $N_0 = 300$ and 600 lines/mm. The $4f$ peak of gold is used for the grating with $N_0 = 1200$ lines/mm because of the low photoelectron yield near the Fermi edge when high energy photons are used for excitation. The calibrated curves for the three gratings used in the BL-4 beamline obtained from experiments are shown in Figure 4.17. The relationship between the wavelength and the linear displacement of the sine bar is the linear function, as expected. The photon energy obtained from experimental and calculated calibration curves are compared in Figure 4.18. It can be seen that the values of photon energy from the calculated and experimental calibration curves are slightly different. The difference is less than 1 percent. This indicates the high accuracy of the scanning mechanics of the monochromator.

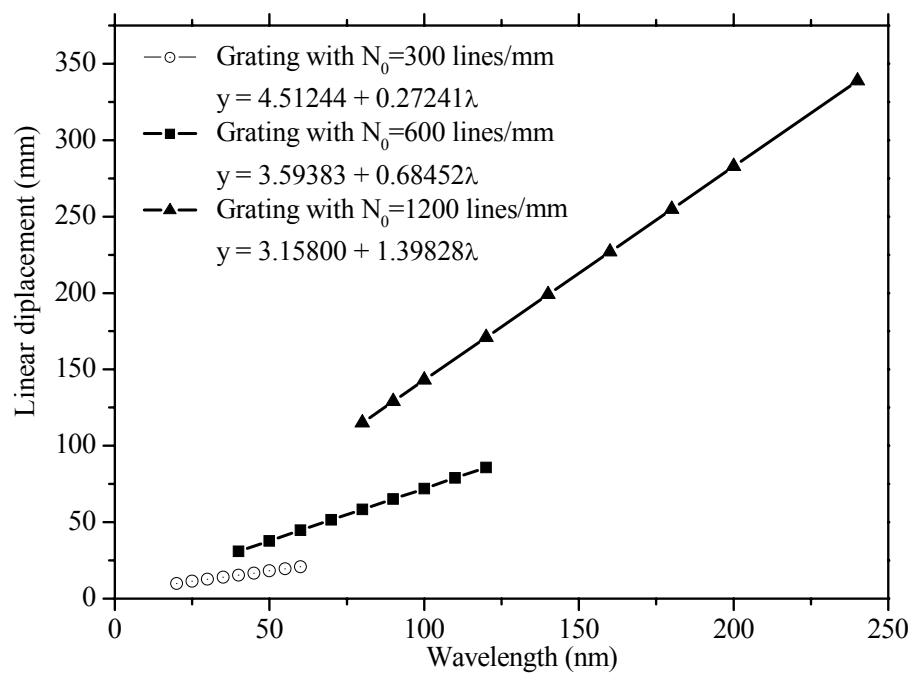


Figure 4.17 The wavelength calibration curves for VLSPG monochromator at BL-4 beamline obtained from photoemission spectra around the Fermi edge and $4f$ peaks of the standard gold sample.

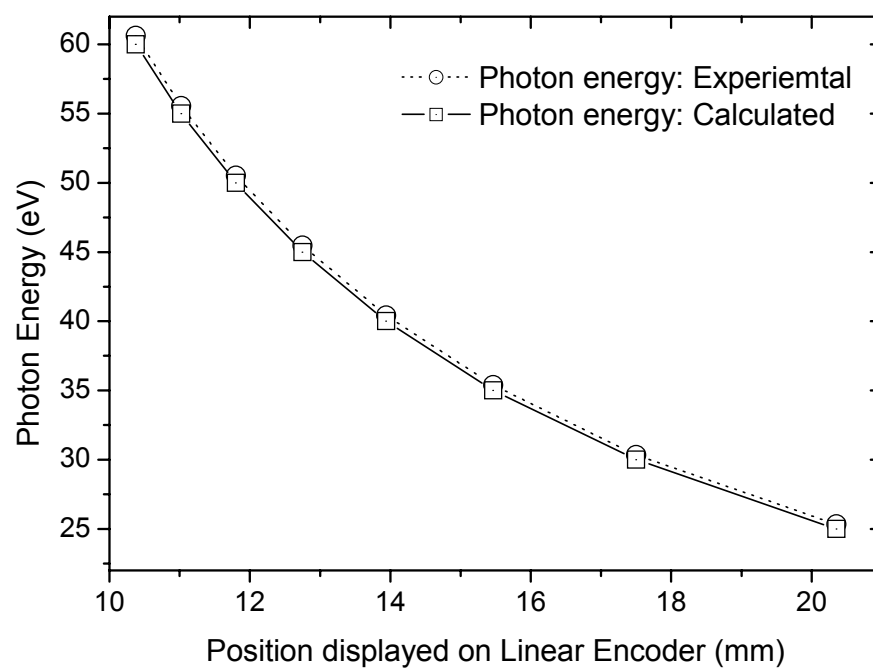


Figure 4.18 The values of photon energy of monochromatic light when using experimental and calculated calibration curves.

4.4 Resolution of the monochromator

Figure 4.19 shows photoemission spectra of gold excited by 40 eV photons. The spectra were taken using the home-developed control and data acquisition system of the BL-4 beamline described in Chapter III. The spectra were taken with different opening of the X-Y aperture in the vertical direction. The Fermi level corresponds to the electron kinetic energy of approximately 36.6 - 3.64 eV. The uncertainty of the position of the Fermi edge will be discussed below. Below the Fermi level, the 6s band is observed. Below the kinetic energy of approximately 35.0 eV, the low binding-energy side of the 5d band is also observed. The total resolution of the measurement system is the FWHM of the distribution around the Fermi level, which is given by

$$(FWHM)_{total}^2 = (FWHM)_{light}^2 + (FWHM)_{spec}^2 + (FWHM)_{temp}^2 \quad (4.2)$$

where

$(FWHM)_{light} \equiv$ the resolution of monochromator

$(FWHM)_{spec} \equiv$ the resolution of the spectrometer

$$(FWHM)_{Temp} = 4.394kT$$

where k and T are the Boltzmann constant and absolute temperature, respectively. The total $FWHM$ of the distribution around the Fermi level are given in Table 4.2.

Table 4.2 *FWHM* of the distribution around the Fermi level obtained from Au spectra shown in Figure 4.19.

Vertical opening of the X-Y aperture (eV)	Total FWHM (eV)	FWHM _{light} (eV)
4	-	-
3	-	-
2	1.2	1.177
1	0.7	0.66
0.5	0.38	0.299
0.25	0.45	0.385

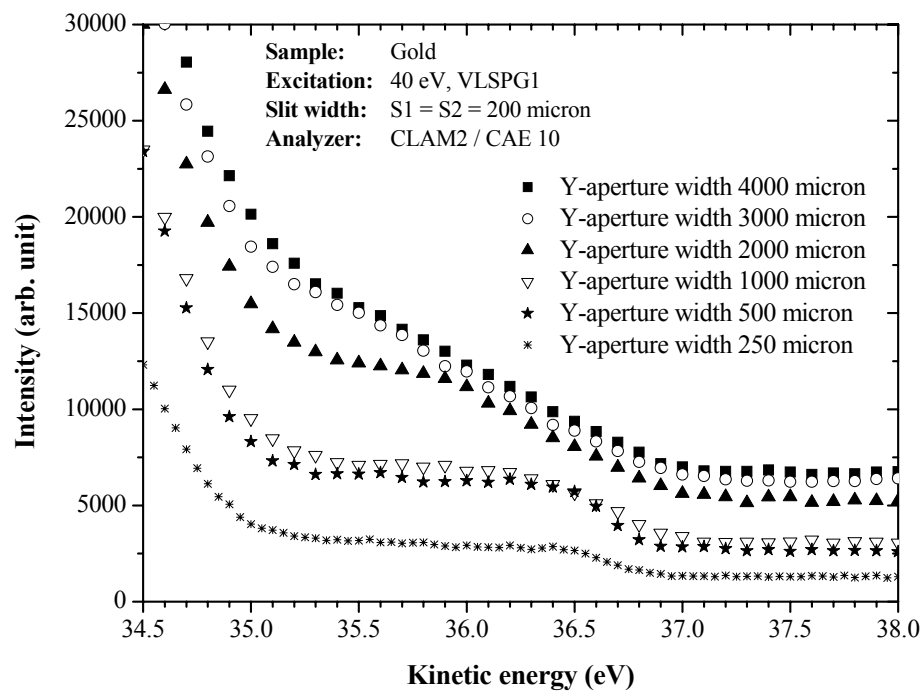


Figure 4.19 PES spectra of gold taking with excitation photon energy of 40 eV using the CLAM2 spectrometer with a new data acquisition and control system.

Ray tracing simulations have been carried out to study the resolving power of the monochromator. In the simulations, the angle of incidence and diffraction were chosen for light with photon energy of 40 eV. The openings of the X-Y aperture in the vertical direction are 500 micron, 1000 micron, 1500 micron, 2000 micron, 2500 micron and fully opened. While the X-Y aperture is fully opened in the horizontal direction. The number of rays used is 9,000,000 rays. The parameters of the source in the bending magnet BM4 are used as the inputs. 9,000,000 rays of synchrotron light in the bandwidth of 0.1 eV were simulated from the source and traced through the optical elements from the first Mask to the exit slit. The results from the ray-tracing simulations are shown as the energy distributions in Figure 4.20. From ray-tracing simulation, the resolution of the monochromatic light was approximately 60 meV when the entrance and exit slits were 200 micron and the vertical opening of the X-Y aperture is fully opened, thus the resolving power of the monochromator is approximately $40 \text{ eV}/60 \text{ meV} = 666$. The resolution is improved when the vertical opening of the X-Y aperture is reduced to be 3000 micron. The resolution obtained from the simulation was approximately 55 meV. To reduce the opening of the aperture further, the resolution cannot be better but the photon flux decreases linearly with the decreasing of the vertical opening of the X-Y aperture. The significant influence of the X-Y aperture on the resolving power is expected when the narrow widths of the entrance and exit slits are used to obtained high resolving power of the monochromator. However, the energy resolution obtained from the simulations is much smaller than the *FWHM* deduced from the photoemission spectrum.

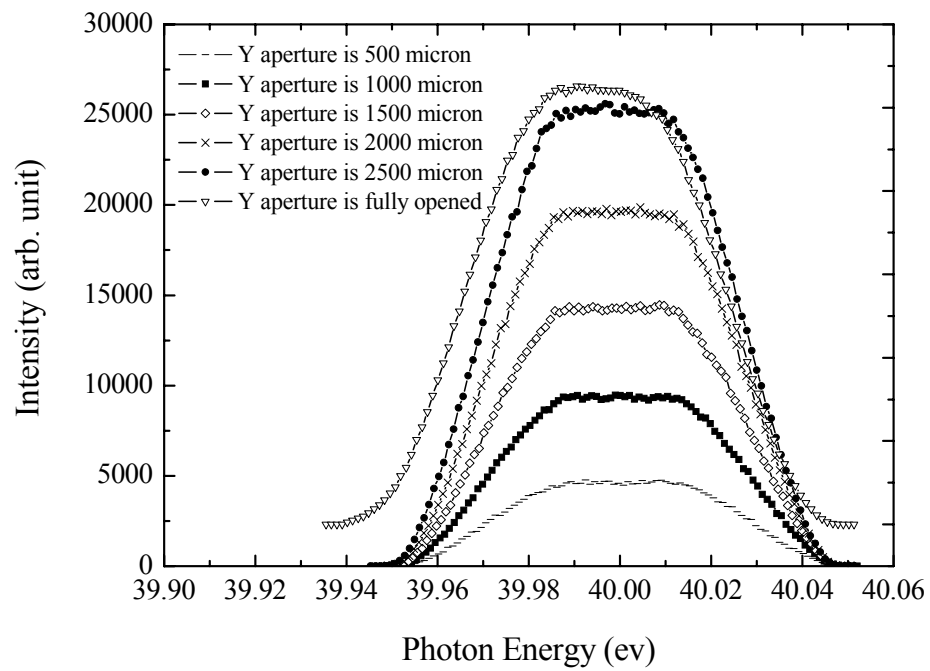


Figure 4.20 The Energy resolution obtained from ray tracing simulations with $S1 = S2 = 200$ micron, the horizontal opening of X-Y aperture is widely opened and the vertical opening of the X-Y aperture are 500 micron, 1000 micron, 1500 micron, 2000 micron, 2500 micron and fully opened.

The shift of the Fermi level of gold determined from Figure 4.19 was also observed. It was even more puzzle when it was found that the Fermi edge shifted when the middle of the vertical opening of the X-Y aperture was offset from the optical axis in the vertical direction. The shift of the energy was so big, approximately 1 eV per 1 mm offset, as shown in Figure 4.21. This shift indicted the change of exciting photon energy. The band width of monochromatized light increasing depended on the width of the vertical opening of the X-Y aperture. Thus the Fermi edges shown in Figure 4.19 become broader when the vertical opening is increased.

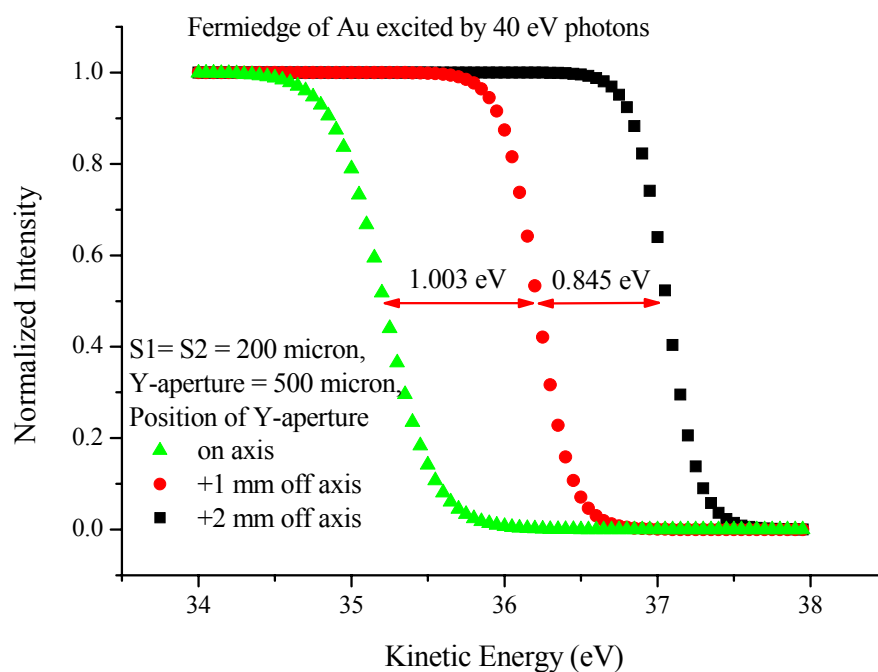


Figure 4.21 Photoemission spectra of gold around the Fermi edge. The spectra shown were from the fitted spectra of measurement data to illustrate the shift of Fermi edge when the middle of the vertical opening of the X-Y aperture was offset from the optical axis in the vertical direction.

In principle, there should be no shift of the photon energy when the middle of the vertical opening of the X-Y aperture was offset from the optical axis in the vertical direction. This is due to the fact that the VLSPG monochromator employs a divergent light beam as the incident beam of the focusing mirror. Thus, the plausible causes for the poor resolution and the shift of photon energy have been exercised using ray-tracing simulations with assumption that the optical elements in the monochromator are misaligned.

The influence of the misalignment of focusing mirror on the resolving power of the monochromator has been studied by ray-tracing simulations. Figure 4.23 shows the energy distribution of monochromatized light, or the energy resolution, obtained from ray tracing simulations. The widths of the entrance and exit slits and the size of the X-Y aperture used in the simulations have been selected to be the same as those in the experiments. The widths of entrance and exit slits are 200 micron, the horizontal opening of the X-Y aperture is fully opened and the vertical opening of the X-Y aperture is 500 micron. When there is no misalignment of the focusing mirror, the resolution of the monochromatized light from the simulations is approximately 55 eV. When the misalignment of the focusing mirror in the vertical direction of -2 mm, -1 mm, 1 mm, and 2 mm have been considered in the simulations, the energy distributions of the monochromatized light shift towards lower energy. However, the energy band width, or the resolution, was not effected by the vertical misalignment of the focusing mirror. It should be noted that the maximum shift of the energy distribution is less than 25 meV per 1 mm misalignment. This shift in energy is not comparable to the observed value, which is approximately 1 eV per 1 mm misalignment. This may be concluded that the misalignment of the focusing mirror

alone cannot be responsible for the poor resolving power of the monochromator and for the shift of photon energy.

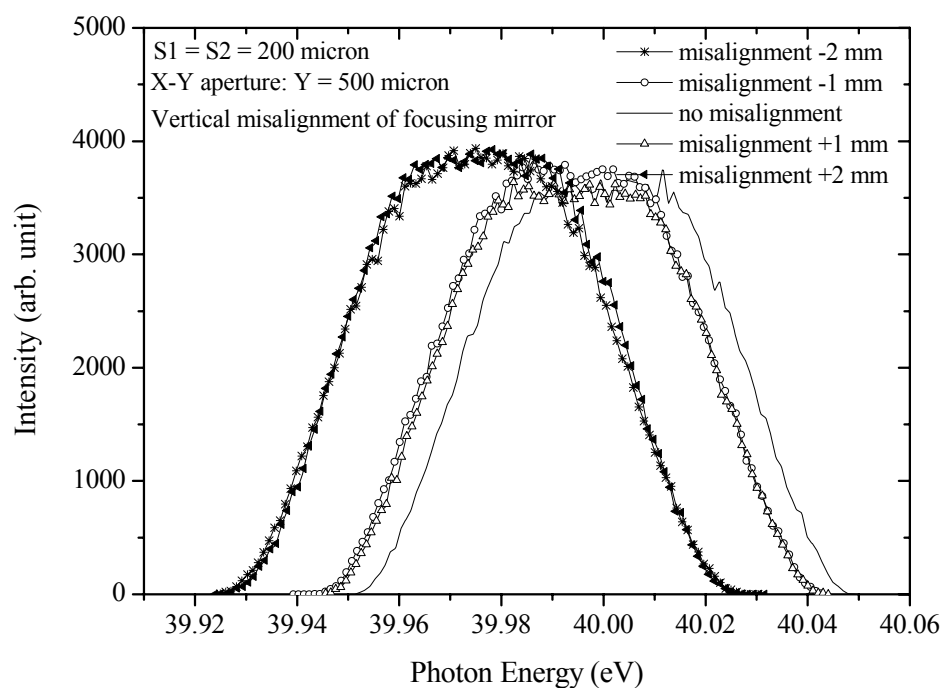


Figure 4.22 The energy distribution of monochromatized synchrotron light resolution obtained from ray tracing simulations with the widths of the entrance and exit slits are 200 micron, the horizontal opening of the X-Y aperture is fully opened and the vertical opening of the aperture is 500 micron. In the simulation, the misalignments of the focusing mirror in the vertical direction of -2 mm, -1 mm, 0 mm (no misalignment), 1 mm and 2 mm were considered.

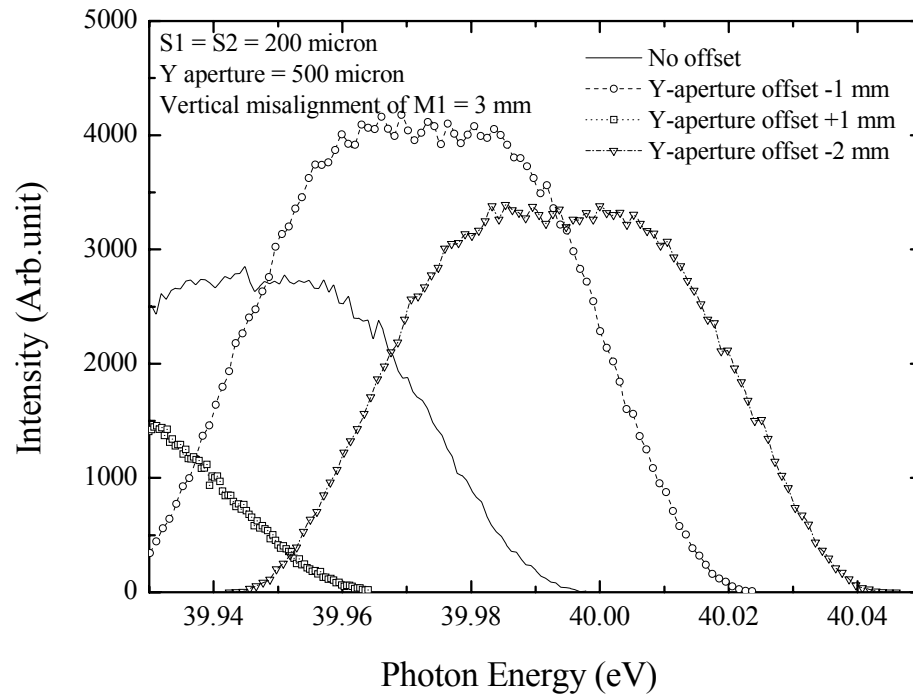


Figure 4.23 The energy distribution of monochromatized light resolution obtained from ray tracing simulations with the widths of the entrance and exit slits are 200 micron, the horizontal opening of the X-Y aperture is fully opened and the vertical opening of the aperture is 500 micron. In the simulation, the misalignments of the focusing mirror in the vertical direction was +3 mm and the vertical offset of the X-Y aperture were -2 mm, -1 mm, 0 mm (no misalignment) and +1 mm.

Figure 4.23 shows the energy distributions obtained from ray-tracing simulations to the influences of the vertical misalignment of the focusing mirror in a combination with the vertical misalignment of the X-Y aperture. In the simulations, the vertical misalignment of the focusing mirror of +3 mm has been considered, the horizontal opening of the X-Y slit was fully opened, the vertical opening of the X-Y aperture was 500 micron and the vertical offset of the X-Y aperture was varied from -2 mm to +1 mm with a 1 mm step. The misalignment of the mirror alone caused the shift of photon energy to lower photon energy, approximately 65 meV. The positive offset of the vertical opening of the X-Y aperture further shift the photon energy to lower photon energy. The negative offset of the opening caused the shift of photon energy to higher energy values. *FWHM* of the energy distribution for all cases is less than 65 meV, which is still much smaller than *FWHM* deduced from photoemission measurement of the standard gold sample.

The combinations of the misalignment of the focusing mirror and the X-Y aperture have also been examined for the misalignment of the focusing mirror of -3 mm. The results obtained from the simulations are shown in Figure 4.24. The obtained results still could not explain the poor resolution and the shift of the photon energy of the monochromatized light deduced from the measurements, as shown in Figure 4.19.

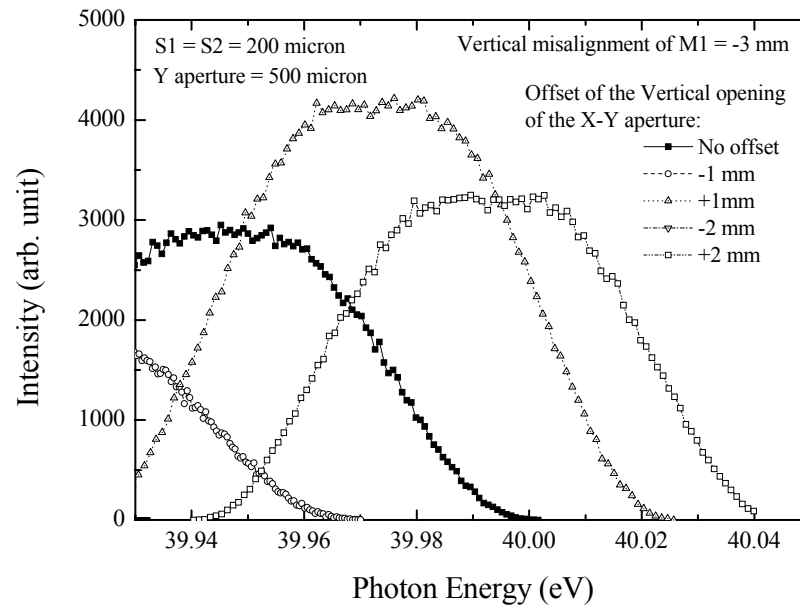


Figure 4.24 The energy distribution of monochromatized light resolution obtained from ray tracing simulations with the widths of the entrance and exit slits are 200 micron, the horizontal opening of the X-Y aperture is fully opened and the vertical opening of the aperture is 500 micron. In the simulation, the misalignments of the focusing mirror in the vertical direction was -3 mm and the vertical offset of the X-Y aperture were -1 mm, 0 mm (no misalignment), +1 mm and +2 mm.

Another plausible reason for the poor resolution and the shift of photon energy for of the monochromatized light was the incorrect installation of the gratings. The gratings have the groove density varying with the length of the grating (the side of the grating that parallel to the optical axis). The groove density of the grating at the center of the grating VLSPG1, VLSPG2 and VLSPG3 are 300 lines/mm, 600 lines/mm and 1200 lines/mm, respectively. The grating chamber has been opened, and the orientation of the gratings has been checked. It was found that the orientation of the gratings was not corrected. In principle, the end of the grating with high groove density should be the downstream end, and the end of the grating with low density must be the upstream end. Thus, the gratings with holder have been removed from the grating chamber. The mistaken of the orientation of all grating has been corrected before installing the holder of the grating back to the grating chamber.

Figure 4.25 shows the photoemission spectra of the standard gold sample around the Fermi edge before and after the correction of the grating orientation. The spectra were taken with excitation energy of 40 eV, the entrance and exit slits were 200 micron and the X-Y aperture was fully opened. Before the correction of the grating orientation, the distribution of the photoelectron yield near the Fermi edge was so broad that *FWHM* of the distribution could not be determined by curve fitting. After the correction of the grating orientation, the Fermi edge of gold could be determined with *FWHM* of 0.364 eV, indicating that *FWHM* of the monochromatized light was 0.279 eV. Not only the resolution but also the photoelectron yield has been improved. The high photoelectron yield indicated higher photon flux was obtained after the correction of the grating orientation. This was a big improvement of the performance of the monochromator of the BL-4 beamline. The resolving power of the monochromator could still be improved by reducing the vertical opening of the X-Y

aperture. This is shown in Figure 4.26. *FWHM* of the distribution of the photoelectron yield and the resolution of the monochromator for different vertical openings of the X-Y aperture are summarized in Table 4.3.

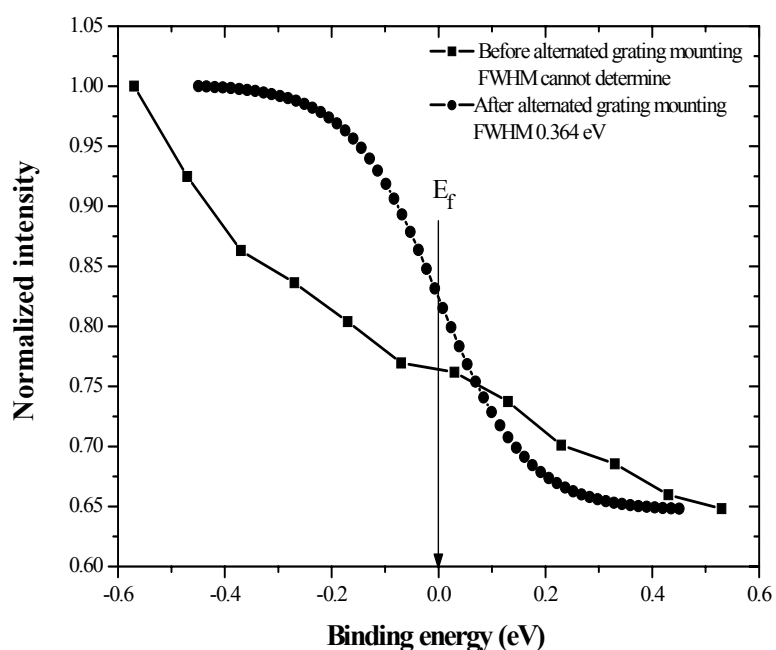


Figure 4.25 Photoemission spectra of the standard gold sample around the Fermi edge before and after the correction of the grating orientation. The spectra were taken with excitation energy of 40 eV, the entrance and exit slits were 200 micron and the X-Y aperture was fully opened.

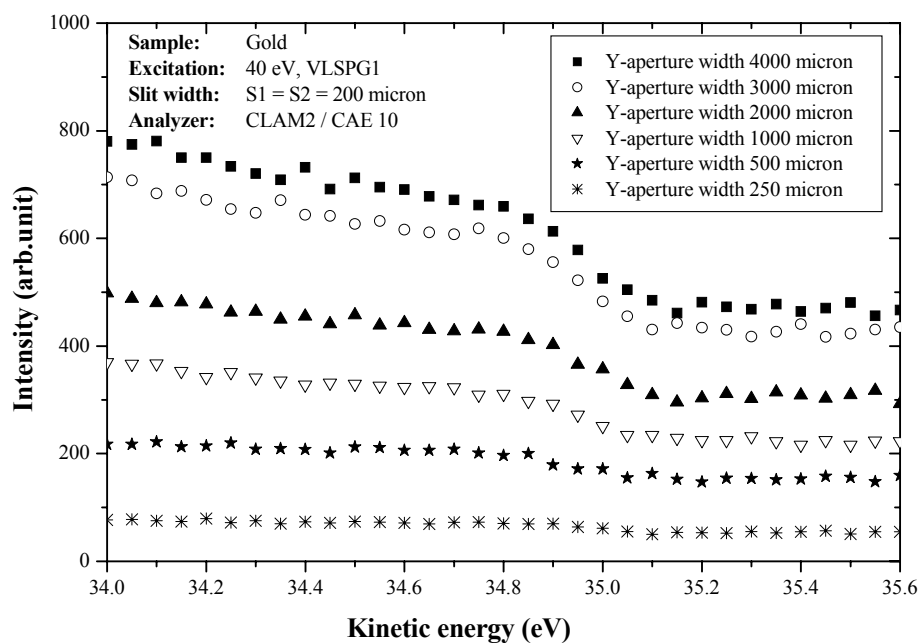


Figure 4.26 PES spectra of gold taking with excitation photon energy of 40 eV, entrance and exit slit widths are 200 micron using the CLAM2 spectrometer. These spectra are taken after the correction of the grating orientation.

Table 4.3 FWHM of the distribution of photoelectron yield of gold near the Fermi level (the spectra are shown in Figure 4.26)

Vertical opening of the X-Y aperture	Total FWHM (eV)	FWHM _{light} (eV)
4000 micron	0.374	0.292
3000 micron	0.312	0.207
2000 micron	0.308	0.200
1000 micron	0.350	0.260
500 micron	0.29	0.186
250 micron	0.252	0.094

The resolving power of the monochromator has been investigated for all three gratings, which covers photon energy from 20 eV to 240 eV. The widths of the entrance and exit slits were chosen to give the resolving power of the monochromator of 500. The widths of the slits for different photon energy are given in Table 4.4. The resolving power of the monochromator obtained from experiments are shown in Figures 4.27, 4.28 and 4.29 for the grating with the groove density at the center of the grating of 300 lines/mm, 600 lines/mm and 1200 lines/mm, respectively. The resolving power of the monochromator using grating VLSPG1 is relatively lower than the calculated value. The cause of this cannot be pin-pointed. However, the size of the beam source may also influence on the resolving power. The experimental results for grating VLSPG2 are agreed quite well with the calculated value.

Table 4.4 The widths of the entrance and exit slits for the resolving power limited by the slit of 500.

Photon energy (eV)	Entrance slit width	Exit slit width
VLSPG1/2/3	(micron)	(micron)
20/40/80	1060	315
25/50/100	684	271
30/60/120	505	237
35/70/140	400	218
40/80/160	332	191
45/90/180	283	174
50/100/200	247	159
55/110/220	219	147
60/120/240	197	137

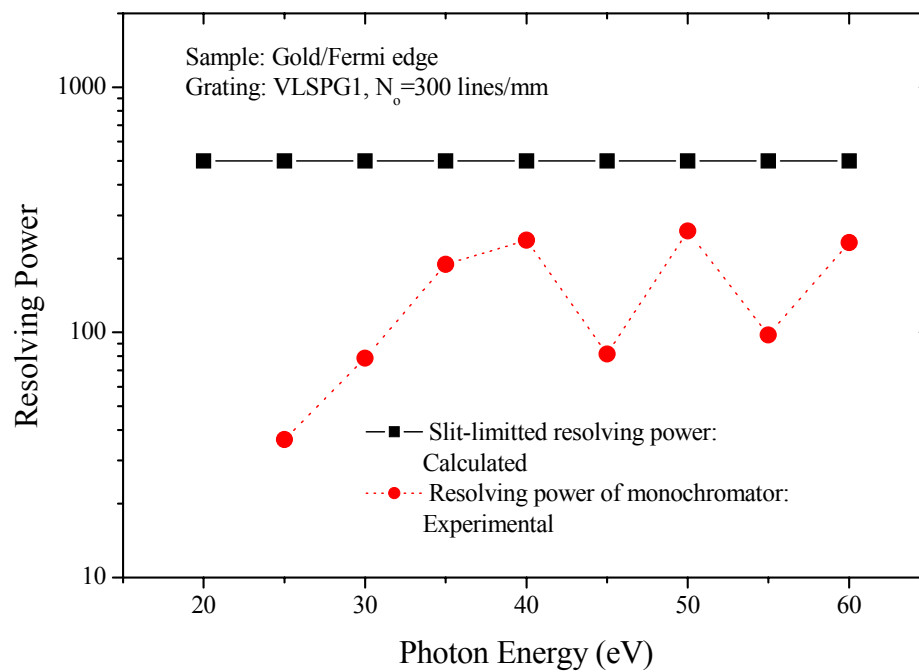


Figure 4.27 The calculated and experimental resolving power of the monochromator using grating with $N_o = 300$ lines/mm.

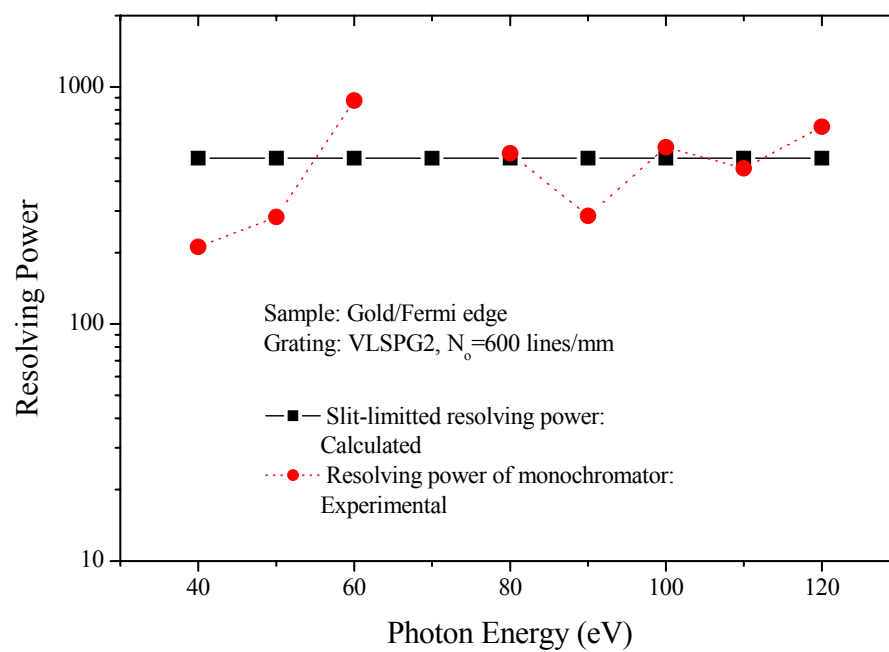


Figure 4.28 The calculated and experimental resolving power of the monochromator using grating with $N_o = 600$ lines/mm.

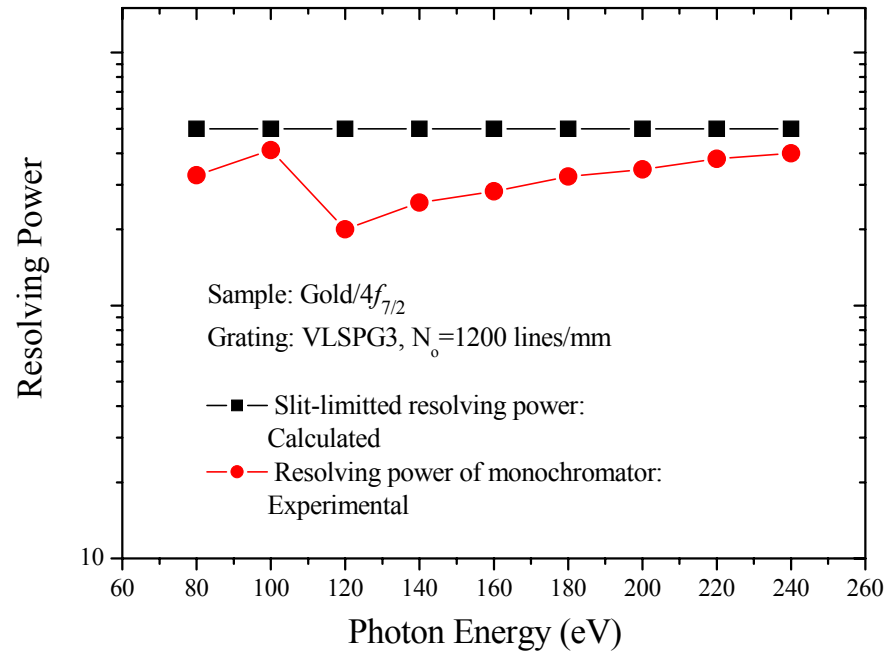


Figure 4.29 The calculated and experimental resolving power of the monochromator using grating with $N_0 = 1200$ lines/mm.

4.5 Higher Order light

Figure 4.30 shows the photoelectron spectrum taken from gold. The excitation light is the monochromatized light from the VLSPG monochromator the BL-4 beamline. The photon energy of the first order light is 40 eV. It can be seen that there are a number of photoelectrons with kinetic energy more than 40 eV. This shows that the monochromatic light contains light with higher orders. The arrows in the Figure indicate the kinetic energy of the photoelectron emitted by excitation of the n^{th} -order light ($n = 1, 2, 3$ and 4). The maximum values of the kinetic energy of the photoelectron for are 35.8 eV, 75.8 eV, 115.8 eV and 155.8 eV for the 1st-, 2nd-, 3rd- and 4th-order light, respectively.

Figures 4.31, 4.32 and 4.33 show the count rate of Au 6s photoelectron as a function of excitation energy of the first-order light using grating with the groove density at the center of 300 lines/mm, 600 lines/mm and 1200 lines/mm, respectively. Figure 4.31 indicates that the second-order light for the lowest groove density is rather below photon energy of 35 eV. Thus one must keep in mind when using this grating for the low energy range. At higher photon energy, the magnitude of the second order is more than 10 times less than that of the first-order light. The magnitude of the high-order light for the other two gratings is not significant.

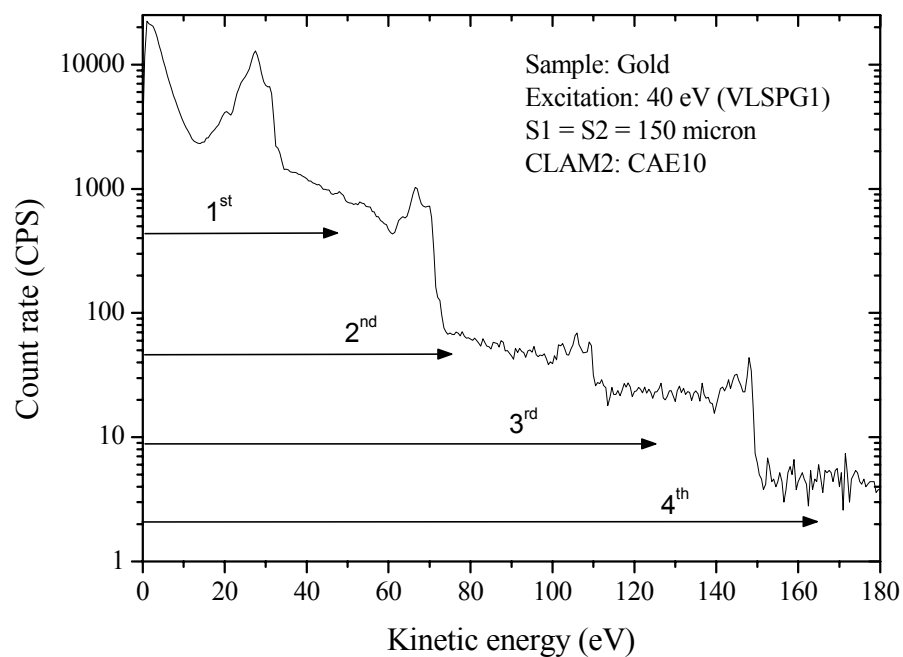


Figure 4.30 The photoemission spectrum of gold taken with the monochromatized light from the BL-4 beamline. The photon energy of the first order light was 40 eV. The grating with $N_0 = 300$ lines/mm was used as the dispersive element in the monochromator.

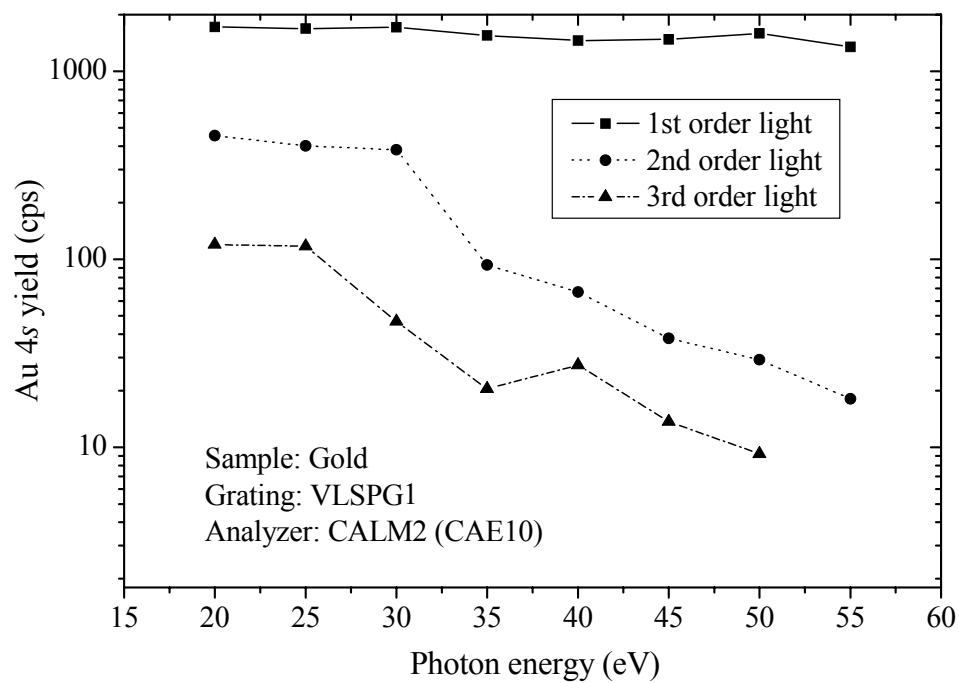


Figure 4.31 The photoelectron yield of 6s band as a function of photon energy showing the magnitude of higher order light for grating with $N_o = 300$ lines/mm.

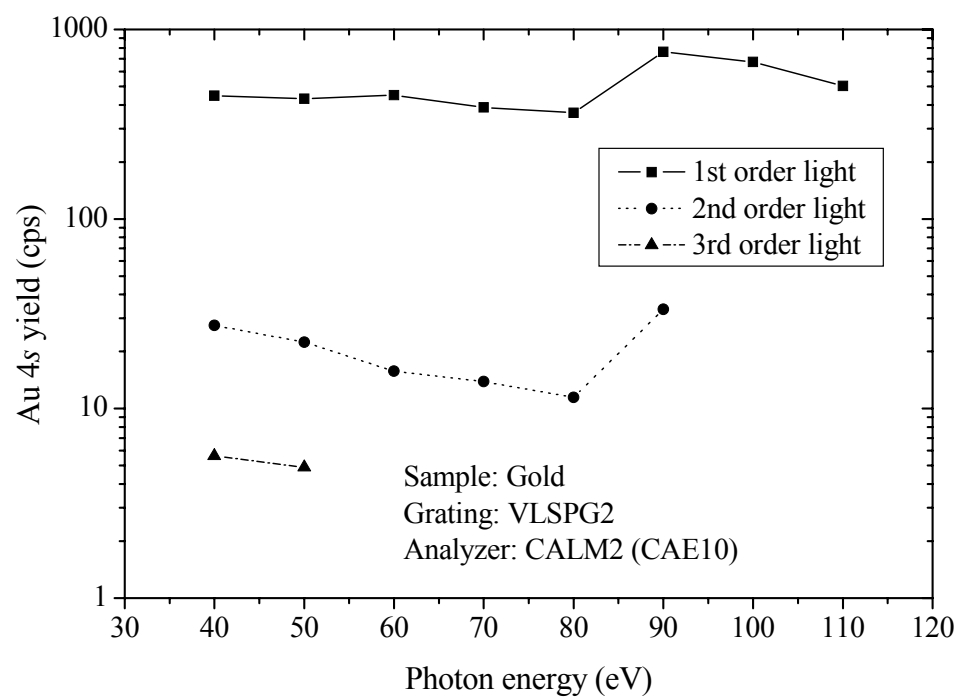


Figure 4.32 The photoelectron yield of 6s band as a function of photon energy showing the magnitude of higher order light for grating with $N_o = 600$ lines/mm.

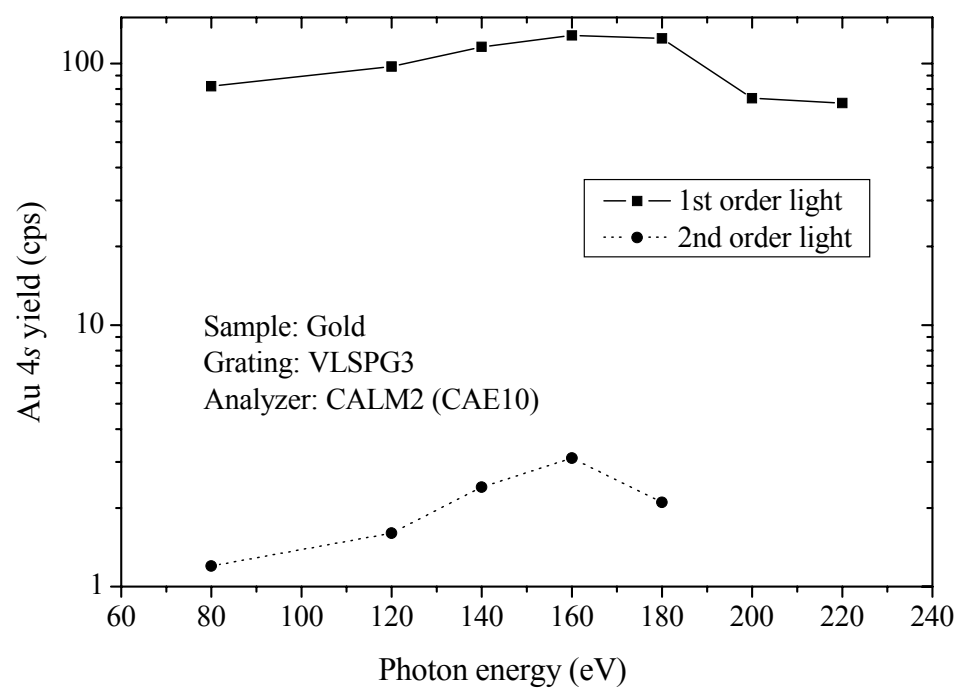


Figure 4.33 The photoelectron yield of $6s$ band as a function of photon energy showing the magnitude of higher order light for grating with $N_0 = 1200$ lines/mm.

CHAPTER V

CONCLUSION

During the course of this thesis work the following achievements have been made:

- The control and data acquisition system of BL-4 for AIPES has been developed. The system expands the uses of synchrotron light in a combination of the existing measuring tools in available at the end station of the BL-4 beamline. Various modes of measurements such as EDC, CIS, CFS and total yield are now available. The system have been used as a tool for the commissioning the BL-4 beamline. It has also been used and will be used by many users of the Bl-4 beamline in spectroscopic research.

- The commissioning of the BL-4 beamline has been carried out successfully. Many technical difficulties have been overcome. The mistaken occurring during the installation of the optical beamline has been corrected. The beamline, optical beamline and experimental station, is now opened for users. The optical beamline provides photons with energy between 20 eV and 240 eV with sufficient photon flux and resolution for photoemission experiments. The characteristics of the optical beamline have been measured, and the results have been compared to the results obtained from theoretical calculations and from ray-tracing simulations using a computer ray-tracing program. Most of the experimental results are in good agreement with that from the calculations and the simulations. However, discrepancies of the results were also found, such as poor resolving power of the monochromator. The plausible cause of the

discrepancies may be related to the source of synchrotron light. This is due to the fact that the electron beam, the light source, in the storage ring was not stable, and the well defined operating orbit was not established during the course of this thesis work. The instabilities influences the electron beam size and position, and in turn, the performance of the optical beamline.

The performance of the beamline is expected to be improved when the quality of the electron beam in the storage ring improves, i.e. the smaller emittance of the electron beam will result in higher photon flux and better resolution.

REFERENCES

REFERENCES

- Chen, C.T., and Sette, F. (1989). Performance of the dragon soft x-ray beamline. **Review of Scientific Instruments**. 60: 1616-1621.
- Damascelli, A. (2002). **Probing the low-energy electronic structure of complex systems by ARPES** [on-line]. Available: http://www.physics.ubc.ca/~damascel/ARPES_Intro.pdf.
- Dietz, E., Braun, W., Bradshaw, A.M., and Johnson, R.L. (1985). A high flux toroidal grating monochromator for the soft x-ray region. **Nuclear Instruments and Methods in Physics Research A**. 239: 359-366.
- Elder, F.R., Langmuir, R.V., and Pollock, H.C. (1948). Radiation from electrons accelerated in a synchrotron. **Physical Review**. 74:52-56.
- Fuggle, J.C. and Mårtensson, N. (1980). Core-Level Binding Energies in Metal. **Journal of Electron Spectroscopy Related Phenomena**. 21: 275.
- Hettrick, M.C. (1990). In-focus monochromator: theory and experiment of a new grazing incidence mounting. **Applied Optics** 29 (31): 4531-4529.
- Itou, M., Harada, T., and Kita, T. (1989). Soft x-ray monochromator with a varied-spacing plane grating for synchrotron radiation: design and evaluation. **Applied Optics** 28: 146-153.
- Johnson, R.L. (1983). Grating monochromators and optics for the VUV and soft x-ray region. In E-E. Koch (ed.). **Handbook on synchrotron radiation**. (Vol. 1A, pp 175-227). Amsterdam: North Holland.

- Kengkan, P., Pairsuwan, W., Isoyama, G., and Ishii, T. (1988). Magnet lattice for the Siam Photon Source. **Journal of Synchrotron Radiation**. 5:348-350.
- Kenneth, R.D. (1998). **Engineering electromagnetics**. USA: Prentice-Hall International.
- Kevan, S.D. (1983). Design of a high-resolution angle-resolving electron energy analyzer. **Review of Scientific Instruments**. 54(11): 1441-1445.
- Kirkpatrick: and Baez, A.V. (1948). Formation of optical image by x-rays. **Journal of the Optical Society of America** . 38: 766-774.
- Krinsky, S., Perlman, M.L., and Waston, R.E. (1983). Characteristics of synchrotron radiation and of its sources. In E-E. Koch (ed.). **Handbook on Synchrotron Radiation**: Vol. 1A (pp 68-73). Amsterdam: North Holland.
- Kitajima, Y., Amemiya, K., Yonamoto, Y., Ohta, T., Kikuchi, T., Kosuge, T., Toyoshima, A., and Ito, K. (1998). A soft X-ray (80-1500 eV) grazing-incidence monochromator with varied-line-spacing plane grating at PF-BL-11A. **Journal of Synchrotron Radiation** 5: 729-731.
- Kiyokura, T., Maeda, F., and Wanatabe, Y. (1998). Optical design for a bending-magnet beamline based on a varied-line-spacing plane grating. **Journal of Synchrotron Radiation** 5: 572-574.
- Lai, B., and Cerrina, F. (1986). SHADOW: A Synchrotron Radiation Ray Tracing Program. **Nuclear Instruments and Methods in Physics Research A**. 246:337
- McKinney, W.R. (1992). Varied Line-Spacing Gratings and Applications (invited). **Review of Scientific Instruments**. 63 (1): 1410-1414.
- Noda, H., Namioka, T., and Seya, M.J. (1974). Geometric Theory of the Grating. **Journal of the Optical Society of America**. 64(8):1031-1036.

- Ono, K., Oh, J.H., Horiba, K., Mizuguchi, M., Oshima, M., Kiyokura, T., Maeda, F., Wanatabe, Y., Kakizaki, A., Kikuchi, T., Yagishita, A., and Kato H. (2001). Performance of the high-resolution high-flux monochromator for bending magnet beamline BL-1C at the Photon Factory. **Nuclear Instruments and Methods in Physics Research A**. 467-468: 573-576.
- Oswald, S. (2000). X-ray photoelectron spectroscopy in analysis of surfaces. In R.A. Meyers (ed.). **Encyclopedia of Analytical Chemistry, Application, Theory and Instrumentation**. (Vol. 10, p 9323). UK: Wiley.
- Pairsuwan, W. and Ishii, T. (2003). Status of the Siam Photon Source. **Nuclear Instruments and Methods in Physics Research B**. 199: 546-549.
- Peatman, W.B. (1997). **Grating, Mirrors and Slits Beamline Design for Soft X-Ray Synchrotron Radiation Sources**. Gordon and Breach Science Publishers, Amsterdam, Netherland.
- Sanguansak, N., Matsui, S., Rujirawat, S., Apiwatwaja, R., Rugmai, S., Prawanta, S., Kwankasem, A., Angsuwattanakul, T., Boonsuya, S., Srichan, S., Tarawarakarn, P., Phacheerak, W., Siri wattanapaitoon, S., Chanpuang, P., Ishii, T., and Pairsuwan, W. (2002). Realignment magnets of Siam Photon Source storage ring. In **Proceedings of the 7th International Workshop on Accelerator Alignment 2002** (pp 55-58). Japan: SPring-8.
- Schäfers, F. (1996). **Ray the BESSY raytrace program to calculate synchrotron radiation beamlines**. Germany: BESSY.
- Seah, M.P., and Smith, G.C. (1996). Spectrometer energy scale calibration. In D. Briggs and M.P. Seah (eds.). **Practical surface analysis: Auger and X-ray photoelectron spectroscopy**. (2nd ed., Vol. 1, p 535). England: John Wiley & Sons.

- Songsiriritthigul, P., Pairsuwan, W., Ishii, T., and Kakizaki, A. (2001). Photoemission at the Siam Photon Laboratory. **Surface Review and Letters** 8(5): 497-500.
- Songsiriritthigul, P., Sombunchoo, P., Raja Sekhar, B.N., Pairsuwan, W., Ishii, T., and Kakizaki, A. (2001). Comparison of varied-line-spacing plane grating and varied-line-spacing spherical grating monochromators for the Siam Photon Source. **Nuclear Instruments and methods in Physics Research A** 467-468:593-596.
- Stevens, H.A., Donoho, A.W., Turner, A.M., and Erskine, J.L. (1983). Angle-resolving photoelectron energy analyzer: mode calculations, ray-tracing analysis and performance evaluation. **Journal of Electron Spectroscopy and Related Phenomena** 32: 327-341.
- Underwood, J.H. (2000). Monochromator and spectrographs using varied line spacing grating. In **Synchrotron Radiation Instrumentation: Eleventh US National Conference 2000** (pp 941-946). American Institute of Physics, USA.
- Underwood, J.H., and Koch, J.A. (1997). High-resolution tunable spectrograph for x-ray laser linewidth measurements with a plane varied-line-spacing grating. **Applied Optics** 36 (21): 4913-4921.

CURRICULUM VITAE

FIRST NAME: SAMRED

LAST NAME: KANTEE

GENDER: Male

NATIONALITY: Thai

DATE OF BIRTH: June 13, 1963.

PLACE OF BIRTH: Udonrtani

EDUCATION BACKGROUND:

- B.Ed. in major Physics, minor Mathematics, March 10, 1984. Bangsaen Sri Nakharinwirot University, Thailand.
- M.Sc. in Physics Teaching, October 22, 1992. Chaingmai University, Thailand.

WORK EXPERIENCE:

- A teacher in physics at Nonsang Witthayakan School, Amphur Nonsang, Udonrthani, Thailand, 1984-1994.
- Lecturer, Physics Program, Faculty of Science, Sakon Nakhon Rajabhat University, Sakon Nakhon, Thailand, 1995- at present.

PUBLICATIONS:

- Songsiriritthigul, P., Nakajima, H., Wongkokua, W., Kantee S., Pairsuwan, W., Ishii T., and Kakizaki, A. (2004). *The commissioning results of the first beamline at the Siam Photon Laboratory*. Synchrotron Radiation Instrumentation: Eighth International Conference, edited by T. Warwick et al., American Institute of Physics, pp 372-375.